
Upper-tropospheric Inflow Layers in Tropical Cyclones

Shanghong Wang



München 2021

Upper-tropospheric Inflow Layers in Tropical Cyclones

Shanghong Wang

Dissertation
an der Fakultät für Physik
der Ludwig-Maximilians-Universität
München

vorgelegt von
Shanghong Wang
aus Gucheng, China

München, den 20.01.2021

Erstgutachter: Prof. Dr. Roger K. Smith
Zweitgutachter: Prof. Dr. George C. Craig
Tag der mündlichen Prüfung: 17.03.2021

Contents

Zusammenfassung	viii
Abstract	xi
1 Introduction	1
1.1 Overview of tropical cyclones	1
1.2 The primary and secondary circulation	3
1.3 Upper radial flow structure	5
1.4 Structure of the thesis	7
2 The numerical model and simulation configuration	9
2.1 The Cloud Model version 1 (CM1)	9
2.1.1 The governing equations of CM1	10
2.1.2 Numerics	11
2.2 Simulation configuration	12
2.3 Determination of the vortex centre	13
3 Experiment overview	15
3.1 Vortex evolution	15
3.2 Azimuthally-averaged vertical structure	17
3.3 Effects of the inflow layers on storm evolution	19
3.4 Horizontal structure of outflow and inflow layers	23
3.5 Summary	26
4 Balance theory	29
4.1 The Sawyer-Eliassen equation	30
4.2 The membrane analogy	33
4.3 A more realistic configuration vis-à-vis the atmosphere	37
4.4 Methods of regularization	39
4.5 An idealized 3D numerical simulation of a tropical cyclone	40
4.5.1 Two regularization schemes	42
4.5.2 The Möller and Shapiro scheme	43
4.5.3 The issue of forcing overlapping with regions in which $\Delta < 0$	43

4.6	Regularization in regions of large vertical shear	44
4.6.1	Exploitation of the membrane analogy	44
4.6.2	A more realistic configuration	45
4.6.3	Comparison between the numerical simulation and the balance calculation at low levels	47
4.7	Discussion	49
5	Balance explanation for upper inflows and its issues	53
5.1	On a balance theory explanation for upper tropospheric inflow jets	54
5.2	Sensitivity calculations and methods	58
5.2.1	Calculation overview	58
5.2.2	Successive Over-Relaxation (SOR) method	59
5.2.3	Multi-grid (MG) method	61
5.3	Results	62
5.3.1	Calculation set Calc-A	62
5.3.2	Calculation set Calc-B	63
5.3.3	Calculation set Calc-C	68
5.3.4	Calculation set Calc-D	69
5.3.5	Summary of the calculations	72
5.4	Discussion	74
6	Explanations for upper inflows	75
6.1	The radial velocity tendency equation	76
6.2	Radial velocity tendency analysis	77
6.3	Diagnosis of imbalance	85
6.4	Azimuth-height structure	87
6.5	Discussion	90
7	Trajectories	91
7.1	Method for calculating trajectories	91
7.2	Results	92
7.2.1	Sample trajectories	92
7.2.2	Statistics of trajectories	95
7.3	Relationship to other studies	99
7.4	Discussion	100
8	Conclusions	101
A	List of acronyms	105
B	List of symbols	107
	Bibliographie	117

Contents	vii
Acknowledgments	119
Curriculum Vitae	121

Zusammenfassung

Dreidimensionale numerische Simulationen mit ausreichender vertikaler Auflösung zur Intensivierung tropischer Wirbelstürme haben gezeigt, dass sich eine Schicht mit starker Einströmung direkt unter der Ausströmregion in der oberen Troposphäre sowie in einigen Fällen eine flachere Schicht mit schwächerem Einströmen über der Ausströmregion entwickelt. Hier stelle ich eine Erklärung für solche Inflow-Jet Muster vor und verwende dazu das prototypische Problem der Intensivierung tropischer Zyklonen, das die Entwicklung eines Wirbels auf einer f -Ebene in einer Umgebung im Ruhezustand betrachtet, in der von einem anfänglich symmetrischen, feuchten, wolkenfreien Wirbel über einem warmen Ozean ausgegangen wird. Ich führe die Einströmschicht auf eine subgradiente Radialkraft zurück, die jenseits eines bestimmten Radius durch einen Großteil der oberen Troposphäre existiert. Einige Auswirkungen der Einströmregion auf die Sturmstruktur werden diskutiert. Eine alternative Erklärung, die sich auf die klassische achsensymmetrische Gleichgewichtstheorie beruft, erweist sich als problematisch.

Die Konsequenzen der Regularisierung der Sawyer-Eliassen-Gleichung zur Berechnung der Stromfunktion für die achsensymmetrische Sekundärzirkulation eines tropischen Wirbelsturms werden erforscht. Die Regularisierung ist ein Ad-hoc-Verfahren, bei dem die Koeffizienten der Gleichung in geeigneter Weise modifiziert werden, um negative Werte der Diskriminante durch kleine positive Werte zu ersetzen und so sicherzustellen, dass die Gleichung global elliptisch ist. Die Konsequenzen des Verfahrens können in Bezug auf das analoge Verhalten einer gedehnten Membran unter einer bestimmten Kraftverteilung verstanden werden.

Verschiedene Regularisierungsverfahren werden bewertet, indem die azimuthal gemittelte radiale Strömung aus einer dreidimensionalen numerischen Simulation eines tropischen Wirbelsturms mit derjenigen aus einer achsensymmetrischen Bilanzberechnung der Sawyer-Eliassen-Gleichung verglichen wird, erzwungen durch diabatische - und Reibungsterme, die aus der Simulation diagnostiziert wurden. Der Vergleich zeigt, dass die größte Herausforderung für die Regularisierung in Regionen der Trägheitsinstabilität auftritt, insbesondere wenn sich der diagnostizierte Antrieb mit solchen Regionen überschneidet. In dem gezeigten Beispiel ist die diagnostizierte balancierte Strömung empfindlich auf das jeweilige Regularisierungsverfahren und keines der untersuchten Verfahren lieferte eine Strömung, die strukturell und quantitativ nahe an der aus der numerischen Lösung erhaltenen Strömung im und nahe dem Regularisierungsbereich lag.

Die Strömung in Bereichen großer vertikaler Scherung, die im unteren Teil der Gren-

zschicht häufig vorkommen, ist weniger empfindlich gegenüber dem Regularisierungsverfahren. Nichtsdestotrotz gibt es vergleichsweise große Unterschiede zwischen der Einströmung in niedriger Höhe in der azimuthal gemittelten numerischen Lösung und der achsensymmetrischen Gleichgewichtslösung. Diese Differenzen können auf das intrinsische Fehlen eines Gleichgewichts in der Grenzschicht zurückgeführt werden. Dieser Befund, zusammen mit den Problemen, die mit der Regularisierung verbunden sind, ist eine weitere Bestätigung dafür, dass die Gleichgewichtsdynamik die Strömung in der Grenzschicht nicht adäquat erfassen kann, im Gegensatz zu jüngsten Behauptungen.

Zwei Methoden zur Lösung der Sawyer-Eliassen-Gleichung für die entsprechende balancierte Sekundärzirkulation einer numerisch simulierten, hochaufgelösten tropischen Zyklone werden verglichen. In idealisierten Berechnungen für einen symmetrisch stabilen Wirbel konvergieren beide Methoden (sukzessive Überrelaxation und Multi-Grid) und die Lösungen sind weitgehend ähnlich. In typischeren Fällen, in denen der Wirbel Regionen mit inertialer oder symmetrischer Instabilität aufweist, ist es notwendig, die Daten aus der numerischen Simulation zu vergrößern, um die balancierte Sekundärzirkulation zu bestimmen. Eine konvergente Lösung kann mit der Multi-Grid-Methode für einen feineren Gitterabstand als mit der Methode der sukzessiven Überrelaxation erzielt werden. Die Multi-Grid-Methode konvergiert jedoch nicht, wenn der vertikale Gitterabstand ähnlich dem der numerischen Simulation ist. Die Ergebnisse beider Methoden bestätigen die Unfähigkeit der Gleichgewichtsformulierung, die starke Einströmung und die daraus resultierende tangentialen Windverstärkung in der Reibungsgrenzschicht während einer Periode schneller Intensivierung zu erfassen.

Die balancierte Sekundärzirkulation kann eine solche Einströmschicht aufweisen. Es ist jedoch Vorsicht geboten, wenn man diese Einströmschicht auf eine dynamisch balancierte Antwort zurückführt, die durch die Verteilung der diabatischen Erwärmung und des tangentialen Impulses angetrieben wird. Diese Studie legt nahe, dass es sich wahrscheinlich um ein Artefakt der Ad-hoc-Regularisierungsmethode handelt, die notwendig ist, um die Sawyer-Eliassen-Gleichung in Regionen mit inertialer und/oder symmetrischer Instabilität global elliptisch zu halten.

Lagrange'sche Trajektorien von Luftpaketen, die von der Einströmschicht ausgehen, die sich unterhalb der Ausströmschicht in der oberen Troposphäre entwickelt, zeigen, dass etwa die Hälfte dieser Trajektorien in der Ausströmregion selbst endet. Die andere Hälfte sinkt langsam in die mittlere bis obere Troposphäre, unterhalb der Ausflussschicht ab und driftet infolge einer relativ schwachen Umwälzzirkulation in diesem Bereich langsam nach außen. Die Berechnungen zeigen, dass die pseudoäquivalente potentielle Temperatur entlang der Trajektorien der Luftpakete nicht annähernd erhalten bleibt, was darauf hindeutet, dass die turbulente Diffusion von Wärme und Feuchte entlang der Trajektorien in der mittleren und oberen Troposphäre beträchtlich ist.

Abstract

Three-dimensional numerical simulations of tropical-cyclone intensification with sufficient vertical resolution have shown the development of a layer of strong inflow just beneath the upper-tropospheric outflow layer as well as, in some cases, a shallower layer of weaker inflow above the outflow layer. Here I provide an explanation for such inflow jets in the context of the prototype problem for tropical-cyclone intensification, which considers the evolution of a vortex on an f -plane in a quiescent environment, starting from an initially-symmetric, moist, cloud-free vortex over a warm ocean. I attribute the inflow layers to a subgradient radial force that exists through much of the upper troposphere beyond a certain radius. Some effects of the inflow layers on the storm structure are discussed. An alternative explanation that invokes classical axisymmetric balance theory is found to be problematic.

The consequences of regularizing the Sawyer-Eliassen equation to calculate the streamfunction for the axisymmetric secondary circulation of a tropical cyclone are explored. Regularization is an *ad hoc* procedure in which the coefficients of the equation are suitably modified to replace negative values of the discriminant by small positive values, thereby ensuring that the equation is globally elliptic. The consequences of the procedure may be understood in terms of the analog behaviour of a stretched membrane subject to a particular force distribution.

Several regularization procedures are assessed by comparing the azimuthally-averaged radial flow from a three-dimensional numerical simulation of a tropical cyclone with that from an axisymmetric balance calculation of the Sawyer-Eliassen equation, forced by diabatic and frictional terms diagnosed from the simulation. The comparison shows that the largest challenge for regularization occurs in regions of inertial instability, especially when the diagnosed forcing overlaps with such regions. In the example shown, the diagnosed balanced flow is sensitive to the particular regularization procedure and none of the procedures examined gave a flow that was structurally and quantitatively close to that obtained from the numerical solution in and near the region of regularization.

The flow in regions of large vertical shear that are common in the lower part of the boundary layer is less sensitive to the regularization procedure. Nevertheless, there are comparatively large differences between the low-level inflow in the azimuthally-averaged numerical solution and the axisymmetric balance solution. These differences can be attributed to the intrinsic lack of balance in the boundary layer. This finding, together with the issues associated with regularization, is further confirmation that balance dynamics is

unable to adequately capture the flow in the boundary layer, contrary to recent claims.

Two methods for solving the Sawyer-Eliassen equation for the corresponding balanced secondary circulation of a numerically-simulated, high-resolution tropical cyclone vortex are compared. In idealized calculations for a symmetrically stable vortex, both methods (successive over-relaxation and multi-grid) converge and the solutions are broadly similar. In more typical cases, where the vortex has regions of inertial or symmetric instability, it is necessary to coarsen the data from the numerical simulation to determine the balanced secondary circulation. A convergent solution can be obtained with the multi-grid method for a finer grid spacing than with the successive over-relaxation method. However, the multi-grid method fails to converge when the vertical grid spacing is similar to that of the numerical simulation. Results using both methods confirm the inability of the balance formulation in capturing the strong inflow and resulting tangential wind spin up in the frictional boundary layer during a period of rapid intensification.

The balanced secondary circulation may show such an inflow layer. However, caution is called for in attributing this inflow layer to a balanced flow response driven by the distribution of diabatic heating and tangential momentum forcing. This study suggests that it is likely an artifact of the *ad hoc* regularization procedure that is necessary to keep the Sawyer-Eliassen equation globally elliptic in regions of inertial and/or symmetric instability.

Lagrangian air parcel trajectories emanating from the inflow layer that develops beneath the upper-tropospheric outflow layer show that about a half of these trajectories end up in the outflow layer, itself. The other half slowly subside to the mid- to upper troposphere, below the outflow layer, and drift slowly outwards as a result of a relatively weak overturning circulation in that region. Calculations show that pseudo-equivalent potential temperature is not approximately conserved along the air parcel trajectories indicating that the turbulent diffusion of heat and moisture along the trajectories is appreciable in the middle and upper troposphere.

Chapter 1

Introduction

1.1 Overview of tropical cyclones

The tropical cyclone is a warm cored, non-frontal synoptic, rapidly counterclockwise (clockwise in the southern hemisphere) rotating system which forms over the warm tropical oceans from where it draws energy to develop. The tropical cyclone has a low-pressure centre and clouds spiraling towards the “eyewall” surrounding the “eye”, the central part of the cyclone where the weather is normally calm and free of clouds. The size of a tropical cyclone, usually characterized by the radial extent of gale force winds near the surface, is typically around 100 to 250 km, but can reach 500 km. When a tropical cyclone makes landfall, the related heavy rainfall, strong winds and storm surge may inflict serious damage to coastal communities. A better understanding of tropical cyclones is crucial for improved prediction and to reduce their impact on human life and property.

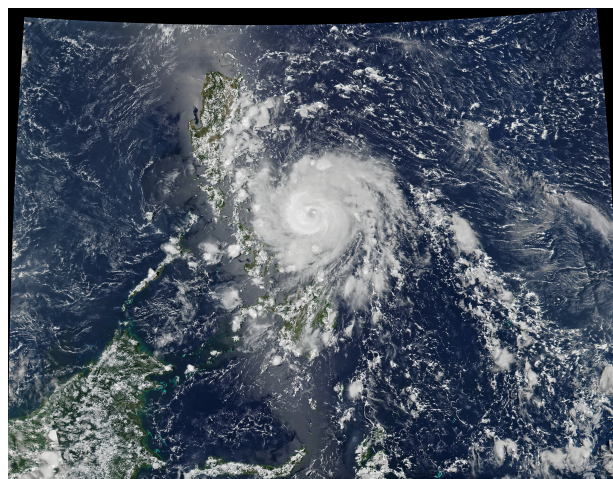


Figure 1.1: High-resolution satellite image of Typhoon Vongfong which was making landfall in the Philippines on May 14 2020. From NASA (National Aeronautics and Space Administration) : <https://earthobservatory.nasa.gov/images/146719>

Figure 1.1 shows a satellite image of Typhoon Vongfong as it made landfall in the Philippines. Its cloud structure including the eye, the eyewall, and spiral rainbands is clearly visible. The eye region of the mature tropical cyclone is a roughly circular area and free of deep clouds, typically 15 to 30 km in radius. Surrounding the eye, there is a cloud wall of deep convection, termed the eyewall. The dense eyewall is the most dangerous part with the most severe weather and the maximum wind near the surface. The peripheral part of a tropical cyclone is one or several deep convective cloud bands, these cloud bands spiral to the central eyewall. In some cases, there may be a single spiral band, which is called the principal band (Willoughby (1988)). For some intense tropical cyclones, when the eyewall contracts and becomes sufficiently small, deep convection in the outer rainband can become organized to form a second eyewall. The newborn outer eyewall inhibits the supply of moisture and angular momentum to the inner eyewall, eventually leads to the demise of the inner eyewall. This process is called eyewall replacement. Figure 1.2 shows an outer and inner eyewall of Typhoon Amber (1997) during an eyewall replacement cycle.

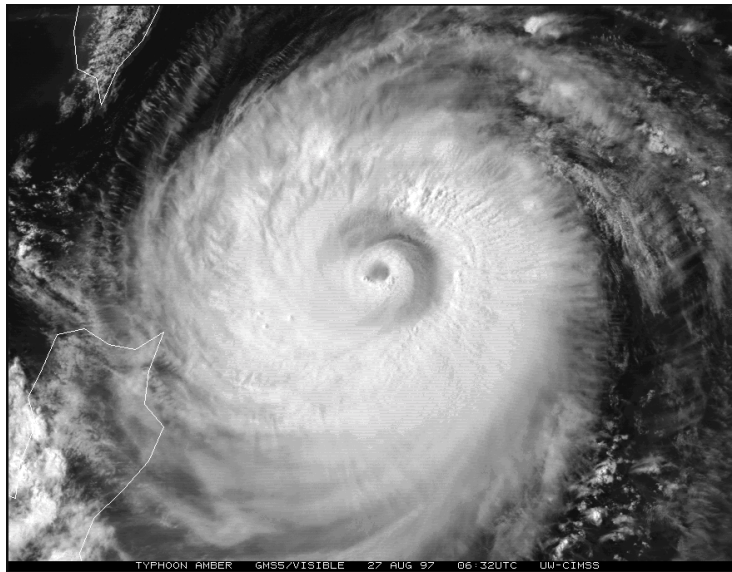


Figure 1.2: A satellite photo of Typhoon Amber (1997) exhibiting an outer and inner eyewall, while undergoing an eyewall replacement cycle. From Cooperative Institute for Meteorological Satellite Studies/Space Science and Engineering Center, University of Wisconsin–Madison.

Based on the maximum sustained surface wind speed at the standard meteorological 10 m level, tropical cyclones can be ranked on different intensity scales. For Atlantic, Eastern and Central Pacific, The National Hurricane Center (NHC) stipulates, if the 1-minute maximum sustained wind speed of tropical cyclone is less than 17 m s^{-1} , the cyclone is called a *tropical depression*. When the maximum wind speed is between 18 m s^{-1} and 32 m s^{-1} , the cyclone is termed a *tropical storm*. Once the wind speed is faster than 33 m s^{-1} , the cyclone is called a *hurricane* and classified on the Saffir-Simpson hurricane wind scale as shown in Table. 1.1. The Joint Typhoon Warning Center (JTWC) applies a similar

standard for the tropical cyclone intensity scale in Western Pacific area, but uses *typhoon* instead of *hurricane*, and *super typhoon* refers to the cyclone which has a wind speed over 67 m s^{-1} .

Category	Max. Wind Speed (ms^{-1})	Max. Wind Speed (mph)
5	≥ 70	≥ 157
4	58–70	130–156
3	50–58	111–129
2	43–49	96–110
1	33–42	74–95

Table 1.1: Saffir-Simpson hurricane wind scale.

For the Western Pacific, the Japan Meteorological Agency (JMA) officially monitor and forewarn tropical cyclones that occur within the Northern Hemisphere between 100°E and 180°E . Unlike JTWC, the JMA uses a 10 minute sustained wind at the 10 m level as the criterion to rank the tropical cyclone intensity scale as recommended by the World Meteorological Organization (WMO). The wind speed following this standard is smaller than that in the JTWC case. The lowest classification of tropical cyclones is a *tropical depression*, while the 10 minutes sustained winds speed is less than 17 m s^{-1} . When the wind speed is between $18\text{--}24 \text{ m s}^{-1}$, the cyclone is classified as a *tropical storm*. Once the system continues to intensify further, it is classified as a *severe tropical storm*, with a wind speed between $25\text{--}32 \text{ m s}^{-1}$. *Typhoon* is the highest classification when the wind speed is greater than 33 m s^{-1} . Specially, a *typhoon* with a maximum sustained surface winds greater than or equal to 66 m s^{-1} , is referred to as a *super typhoon*.

1.2 The primary and secondary circulation

The mature tropical cyclone vortex can be approximately conceptualized as a primary (tangential) circulation with a secondary (overturning) circulation superposed (Ooyama 1982). The primary circulation is a horizontal quasi-symmetric cyclonic circulation around the cyclone centre. A scale analysis by Willoughby (1990) shows that the azimuthally averaged tangential circulation of tropical cyclones is in roughly gradient wind balance (outward pointing centrifugal and Coriolis forces are counterbalanced by the inwards pointing pressure gradient force) and hydrostatic balance (a balance between the vertical pressure gradient and the gravitational force) when frictional effects can be neglected (e.g. in the free atmosphere, above the frictional boundary layer).

The secondary circulation is typically inwards in the lower troposphere and outwards in the upper troposphere, with a strong updraft in the eyewall. The secondary circulation is driven primarily by buoyancy forces associated with latent heat release in deep cumulus convection in the central convection zone of the vortex. Assuming a tropical cyclone is in strict gradient wind balance and hydrostatic, one can derive an equation relating to this

kind of compound balance and we refer to this as thermal wind balance. Then one can derive a second order partial differential equation in the radius-height plane, so-called the Sawyer-Eliassen equation for the transverse circulation for the meridional streamfunction, ψ . In the anelastic approximation, the density is assumed to be a function of height only and acoustic waves are filtered out of the equations. With this approximation, the radial velocity component, u and the vertical velocity component, w can be diagnosed in terms of a streamfunction for the overturning circulation. The derivation of the Sawyer-Eliassen equation will be presented in Section 4. This equation governs the overturning circulation that is required to keep the vortex in a state of persistent thermal wind balance as the tangential momentum forcing and thermodynamic heat forcing tries to drive the vortex out of balance.

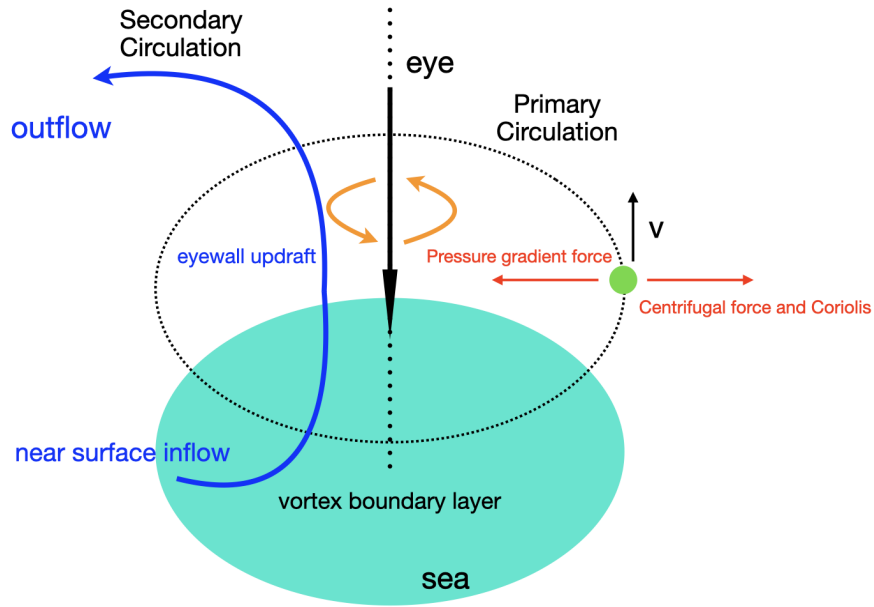


Figure 1.3: Schematic diagram illustrating the primary circulation and the secondary circulation of a tropical cyclone.

As is shown in Figure 1.3, when the primary and secondary circulations are combined, air parcels are spiralling inwards, upwards and outwards. The rising branch of the secondary circulation near the centre is warmer than the subsiding branch, which occurs at large radial distances (more than 500 km), so the combined spiralling circulation is energetically direct.

Previous work has suggested that the solution of the Sawyer-Eliassen is sufficient to describe the secondary circulation in an intensifying tropical cyclone, including in the vortex boundary layer (Heng et al. 2017). However, this assertion has been rebutted by Montgomery and Smith (2018), who noted that Heng et al. did not solve a strictly balance

vortex model and inadvertently ignored the requirement that the basic state vortex remain in a state of strict thermal wind balance during the vortex evolution.

Heng et al. (2018) attempted to rebut the critique of Montgomery and Smith (2018) by solving the Sawyer-Eliassen equation for a single numerical simulation, but again employed basic state vortices that are not in strict thermal wind balance. Recent work of Montgomery and Persing (2020) has affirmed prior findings of Bui et al. (2009) and Abarca and Montgomery (2014) that the strict Sawyer-Eliassen balance model fails to represent the strong inflow in the boundary layer needed to generate the intensifying tangential winds.

Recent research shows that the secondary circulation has a more detailed structure, with a strong supergradient outward jet above the boundary layer and upper tropospheric inflow layers sandwiching the upper troposphere outflow layer.

1.3 Upper radial flow structure

The outflow layer of tropical cyclones is where upper tropospheric air moves radially outward anticyclonically from the centre of a tropical cyclone. Anthes (1974) argued that outflow in tropical cyclones can remove anticyclonic angular momentum from the cyclone at larger radii (more than 500 km) and removes high-entropy air from the cyclone centre. Typically, the outflow layer is asymmetric with one or two anticyclonic outflow jets. Limited by the few vertical layers in the early numerical models and few cases of observational experiments with enough altitude, research on the outflow layer has progressed slowly in the last 40 years.

The last few years have seen the possible importance of the outflow layer in tropical cyclone behaviour brought to the fore (e.g. Rappin et al. 2011; Emanuel 2012; Komaromi and Doyle 2017; Doyle et al. 2017; Tao et al. 2019). Rappin et al. (2011) claimed to have “demonstrated that weak inertial stability in the outflow layer minimizes an energy sink of the tropical cyclone secondary circulation and leads to more rapid intensification to the maximum potential intensity”. However, in many simulations of tropical cyclone behaviour, including the one to be described here, the outflow becomes primarily a region of *inertial instability* (e.g. Smith et al. 2018a) so that, as shown here in sections 5.1 and 6.3, ideas based on balance arguments are questionable.

Emanuel (2012) hypothesized that tropical cyclone intensification is controlled by small-scale turbulent mixing in the upper tropospheric outflow and offered an analytical theory in which a parameterization of this mixing process is the sole positive term in an equation for the tendency of the maximum tangential wind (his Eq. (16)). Nevertheless, the physics of the intensification process, i.e., how in reality this mixing would lead to the required inward movement of the surfaces of absolute angular momentum at low levels for spin up, remains to be articulated (Montgomery et al. 2019; Montgomery and Smith 2019).

The presumed importance of the outflow layer in the intensification process motivated a recent field experiment conducted in the Atlantic and Eastern Pacific sectors, called the Tropical Cyclone Intensity (TCI) experiment (Doyle et al. 2017). The main motivation for this experiment appears to rest on the overarching hypothesis that “this upper-tropospheric

layer is a critical one, as changes in the TC (tropical cyclone) outflow can directly *cause* changes in the TC secondary circulation” (Doyle et al. 2017, p2113). “The overarching goal of the TCI programme is to improve the prediction of TC intensity change, especially rapid intensification (RI) and rapid decay (RD), as well as TC structural changes that are hypothesized to occur through synergistic interaction with outflow” (Doyle et al. 2017, p2114).

The researchers of the TCI programme listed several key science goals to address as part of their programme. Two of them stand out as particularly important (Doyle et al. 2017, p2114):

- to understand the coupling of tropical cyclone outflow with inner-core convection and its implications for intensity change;
- to interpret observations of the fine-scale horizontal and vertical structure of the outflow layer and inner-core regions of the tropical cyclone.

Most notably, there was no mention of the possible existence and role of upper-tropospheric inflow layers that are found to develop in numerous numerical model simulations of tropical cyclone intensification where the vertical resolution is sufficient (e.g. Rotunno and Emanuel 1987, Figure 5c; Hausman et al. 2006, Figures. 4b and 8b; Bui et al. 2009, Figure 6a; Bu et al. 2014, Figure 4a,b, Figure 9a,b, Figure 12, Figure 16; Persing et al. 2013, Figures 15a, 17a, 18a; Ohno and Satoh 2015, Figure 2b; Smith et al. 2014b, Figure 2c; Fovell et al. 2016, Figures 11-21; Kieu et al. 2016, Figures 2b, 4; Heng et al. 2017, Figure 4c; Chen et al. 2018, Figure 14a,c; Smith et al. 2018b, Figure 2b,d). Most of these papers relate to the evolution of a tropical-cyclone-like vortex in the prototype problem for tropical cyclone intensification, which considers the evolution of a vortex on an f -plane in a quiescent environment, starting from an initially symmetric, moist, cloud free vortex over a warm ocean. Some of the studies show inflow layers above and below the outflow layer, while others focus on the layer above the outflow layer in the lower stratosphere. However, to my knowledge, the reasons for the occurrence of the inflow layers and their significance in cyclone behaviour has received little attention. Indeed, they are not considered when treating the tropical cyclone as type of thermodynamic Carnot heat engine (e.g. Emanuel 1986, 1988, 1991, 2018 and refs.).

Only recently have detailed observations of the tropical cyclone outflow layer become available, largely as a result of the use of unmanned aircraft drones to release dropwindsondes into storms from the lower stratosphere (e.g. Braun et al. 2016). While the main purpose of such measurements was to document the outflow layer itself, the data offer the opportunity to detect any layers of inflow in the vicinity of the outflow layer. A comprehensive study of such dropsonde data was presented by Komaromi and Doyle (2017) and Duran and Molinari (2018). These analyses, together with one of Hurricane Edouard (2013) by Smith et al. (2019), do point to the existence of a layer of enhanced inflow above and/or below the outflow in nature. The possible importance of these inflow layers and their role in storm behaviour would seem to merit further study.

Traditionally, it has been difficult to obtain detailed measurements of the upper troposphere flow in tropical cyclones as this region tends to be above the ceiling of conventional jet aircraft. The situation changed with the recent deployment of the NASA Global Hawk to survey storms. The Global Hawk is an autonomous aircraft drone that can overfly storms and release dropsondes into them from the lower stratosphere. One such study of cyclone structure based on such soundings is that by Komaromi and Doyle (2017). These authors show radius-height cross sections of radial wind for two composite data sets obtained from dropsondes into six non-developing or developing storms: their Figure 8a and 8c, respectively. Both these composites show layers of inflow above and below the upper tropospheric outflow layer, but a little surprisingly, the inflow layer beneath the outflow layer is stronger in the case of the non-developing storms.

In their Figure 10, Komaromi and Doyle (2017) show individual radius-height cross sections of radial wind for four storms in their data set and in their Figure 11 they show vertical cross sections of radial flow averaged from 100-500 km radius. Again, these data show layers of inflow above and below the upper tropospheric outflow layer.

Another observational study is that by Smith et al. (2019), which presented vertical cross sections of wind and thermodynamic fields obtained in Atlantic Hurricane Edouard (2014), one of the storms investigated also by Komaromi and Doyle. Figure 1c of Smith et al. shows a radius-height cross-section of mean radial flow constructed from the dropsonde data obtained over an 18 h period on September 16-17. This cross section shows that, above a height of 10 km, there are significant layers of inflow straddling the upper tropospheric outflow layer.

Duran and Molinari (2018) described an observational analysis of the upper troposphere and lower stratosphere of rapidly-intensifying Hurricane Patricia (2015) in which they showed two vertical cross sections of the storm-relative radial and tangential velocities in the lower stratosphere based on dropsonde data (their Figure 10). They stated that the radial cross sections corroborate the existence of a lower stratospheric inflow layer connected to descent in the eye.

Overall, the observational findings are not surprising in view of the propensity of numerical models to show the development of upper-tropospheric inflow layers, even though in reality, such inflow layers may be significantly influenced by the effects of environmental vertical wind shear that is normally present in real cases.

1.4 Structure of the thesis

A brief description of the model used in this study (Cloud Model Version 1 - CM1) and the configuration of the simulations carried out are described in Chapter 2. The behaviour of the vortex evolution and structure features are discussed in Chapter 3. Chapter 4 reviews the traditional axisymmetric balance theory and its limitation. Chapter 5 examines issues with an interpretation of the inflow layers on the basis of traditional axisymmetric balance theory and shows that an explanation for the inflow layers in terms of axisymmetric balance dynamics is problematic. A comparison of balance calculations by two different

methods suggests that the balanced solution structure is likely an artifact of the ad hoc regularization procedure that is necessary to keep the Sawyer-Eliassen equation globally elliptic in regions of inertial and/or symmetric instability. Chapter 6 provides a new framework for examining the outflow and inflow layer dynamics in tropical cyclone vortices based on Newton's second law. Diagnostics of the normalized agradient force, a measure of the degree of imbalance in the numerical simulation, and azimuth-height structures are also shown in this chapter. Chapter 7 shows the trajectories originating in the inflow layers. A summary and conclusions are given in Chapter 8.

Chapter 2

The numerical model and simulation configuration

2.1 The Cloud Model version 1 (CM1)

The Cloud Model version 1 (CM1) used for this study is a three-dimensional, non-hydrostatic, non-linear, time-dependent numerical model for idealized studies of atmospheric phenomena. It has been developed primarily by George Bryan at The Pennsylvania State University (2000-2002) and at the National Center for Atmospheric Research (NCAR). CM1 is designed primarily for idealized research, especially for relatively small-scale processes and deep precipitating convection such as thunderstorms and cyclones.

The governing equations of CM1 conserve total mass and total energy. Because CM1 calculates the total mass during a model integration and uses equations with additional energy terms (e.g., terms associated with the heat content of hydrometeors and dissipative heating which are neglected by other models), it has a mass/energy error that is several orders of magnitude smaller than other numerical models (e.g., the Pennsylvania State University/National Center for Atmospheric Research mesoscale model (MM5), the Advanced Regional Prediction System (ARPS), the Regional Atmospheric Modeling System (RAMS), the Weather Research and Forecasting (WRF) Model). A particular advantage of CM1 is that it can be used to carry out large domain simulations in high resolution with a comparatively little memory overhead. For this reason, the model can be applied to very large problems (i.e., domains of order 10^9 grid points). Further, CM1 can use different equation sets for different applications, such as the user can choose three different solvers (depending on application and desired accuracy) to integrate the compressible equations, even be used with the anelastic equations or incompressible equations. Therefore CM1 is very efficient for a broad range of problems that span many scales. Details can be found in Bryan and Fritsch (2002) and Bryan and Rotunno (2009b).

Based on few limited comparative tests on single-processor machines (more information can be obtained from the CM1 website¹), CM1 is roughly 2 times faster and uses roughly

¹<https://www2.mmm.ucar.edu/people/bryan/cm1/>

half as much Random Access Memory (RAM) as the Advanced Research WRF. Also, CM1 is roughly 1.5–2 times faster than ARPS (when using the same time step), and uses 75% of the Random Access Memory (RAM) required by ARPS.

2.1.1 The governing equations of CM1

Here, for a variable α , $\alpha(x, y, z, t) = \alpha_0(z) + \alpha'(x, y, z, t)$, the subscript 0 denotes the base state which is invariant in time and is a function of z only, and the superscript prime denotes the perturbation from the base state.

CM1's governing equations include prognostic equations for $u, v, w, q_v, q_l, q_i, \theta'$ and π' , where, u is velocity in the x direction; v is velocity in the y direction; w is velocity in the z direction. q_v is the water vapor mixing ratio; q_l is the mixing ratio of liquid water; q_i is the mixing ratio of solid water (ice), $\pi = (p/p_{00})^{R_d/C_p}$ is the Exner function which presents a non-dimensional pressure, p is pressure, p_{00} is a standard reference pressure. R_d is the specific gas constant for dry air, and C_p is the specific gas constant for dry air at constant pressure. θ is the potential temperature. The base state is further assumed to be in hydrostatic balance,

$$\frac{d\pi_0}{dz} = -\frac{g}{C_p\theta_{\rho 0}}, \quad (2.1)$$

where, g is the acceleration due to gravity, θ_ρ is density potential temperature,

$$\theta_\rho = \theta \frac{1 + q_v/\epsilon}{1 + q_v + q_l + q_i}, \quad (2.2)$$

where, ϵ is the ratio of R_d to R_v , R_v is the specific gas constant for water vapor.

The governing equations for velocity (u, v, w) are

$$\frac{\partial u}{\partial t} + C_p\theta_\rho \frac{\partial \pi'}{\partial x} = ADV(u) + fv + T_u + D_u + N_u \quad (2.3)$$

$$\frac{\partial v}{\partial t} + C_p\theta_\rho \frac{\partial \pi'}{\partial y} = ADV(v) - fu + T_v + D_v + N_v \quad (2.4)$$

$$\frac{\partial w}{\partial t} + C_p\theta_\rho \frac{\partial \pi'}{\partial z} = ADV(w) + b + T_w + D_w + N_w \quad (2.5)$$

where, $ADV(\alpha)$ is the advection operator in CM1 which defined as

$$\begin{aligned} ADV(\alpha) &= -u \frac{\partial \alpha}{\partial x} - v \frac{\partial \alpha}{\partial y} - w \frac{\partial \alpha}{\partial z} \\ &= \frac{1}{\rho_0} \left[-\frac{\partial(\rho_0 u \alpha)}{\partial x} - \frac{\partial(\rho_0 v \alpha)}{\partial y} - \frac{\partial(\rho_0 w \alpha)}{\partial z} \right. \\ &\quad \left. + \alpha \left(\frac{\partial(\rho_0 u)}{\partial x} + \frac{\partial(\rho_0 v)}{\partial y} + \frac{\partial(\rho_0 w)}{\partial z} \right) \right], \end{aligned} \quad (2.6)$$

and b is the buoyancy,

$$b = g \frac{\theta_\rho - \theta_{\rho 0}}{\theta_{\rho 0}}, \quad (2.7)$$

and ρ is density, f is the Coriolis parameter, the T terms represent tendencies from turbulence, the D terms represent optional tendencies from other diffusive processes and N terms represent Newtonian relaxation (i.e., Rayleigh damping).

The governing equations for the moisture are

$$\frac{\partial q_v}{\partial t} = ADV(q_v) + T_{q_v} + D_{q_v} - \dot{q}_{cond} - \dot{q}_{dep} \quad (2.8)$$

$$\frac{\partial q_l}{\partial t} = ADV(q_l) + T_{q_l} + D_{q_l} + \dot{q}_{cond} - \dot{q}_{frz} + \frac{1}{\rho} \frac{\partial(\rho V_l q_l)}{\partial z} \quad (2.9)$$

$$\frac{\partial q_i}{\partial t} = ADV(q_i) + T_{q_i} + D_{q_i} + \dot{q}_{dep} + \dot{q}_{frz} + \frac{1}{\rho} \frac{\partial(\rho V_i q_i)}{\partial z} \quad (2.10)$$

where The \dot{q} terms represent phase changes between these three components, The last term on the right hand sides of Eq.(2.9) and Eq.(2.10) represents the effect of hydrometeor fallout by a terminal fall velocity (V , which is assumed to be positive-definite).

The governing equations for θ' and π' are

$$\begin{aligned} \frac{\partial \theta'}{\partial t} = & ADV(\theta) - \Theta_1 \theta \left(\frac{\partial u}{\partial x} + \frac{\partial v}{\partial y} + \frac{\partial w}{\partial z} \right) + \Theta_2 (L_v \dot{q}_{cond} + L_s \dot{q}_{dep} + L_f \dot{q}_{frz}) \\ & + \Theta_3 (\dot{q}_{cond} + \dot{q}_{dep}) + T_\theta + D_\theta + N_\theta + \Theta_2 \epsilon + \dot{Q}_\theta + W_T, \end{aligned} \quad (2.11)$$

$$\begin{aligned} \frac{\partial \pi'}{\partial t} = & ADV(\pi) - \Pi_1 \pi \left(\frac{\partial u}{\partial x} + \frac{\partial v}{\partial y} + \frac{\partial w}{\partial z} \right) + \Pi_2 (L_v \dot{q}_{cond} + L_s \dot{q}_{dep} + L_f \dot{q}_{frz}) \\ & + \Pi_3 (\dot{q}_{cond} + \dot{q}_{dep}) + \Pi_4 (T_\theta + D_\theta + N_\theta + \Theta_2 \epsilon + \dot{Q}_\theta + W_T) + \Pi_5 (T_{q_v} + D_{q_v}), \end{aligned} \quad (2.12)$$

where \dot{Q}_θ represents external tendencies to internal energy, primarily radiative heating/cooling. W_T represents the cooling/warming effect from hydrometeors that fall relative to air, $\Theta_2 \epsilon$ is associated with dissipative heating, which is the increase in internal energy that occurs when kinetic energy is dissipated. The values of variables Θ and Π depend on whether the equation set mathematically conserves mass and energy in moist environments. The quantities L_v , L_s and L_f are the specific latent heats for vaporization, water substance and fusion respectively.

2.1.2 Numerics

CM1 uses terrain-following coordinates, following Gal-Chen and Somerville (1975). The nominal heights of the coordinate surfaces are given by

$$\sigma = \frac{z_t(z - z_s)}{z_t - z_s}, \quad (2.13)$$

where $z_s(x, y)$ is the terrain elevation, and z_t is the constant height of the model top. CM1 uses the framework of the Arakawa-C grid (Arakawa and Lamb 1977), all momentum points are staggered in the middle grid point with one half a grid spacing from the scalars points grid (Figure 2.1).

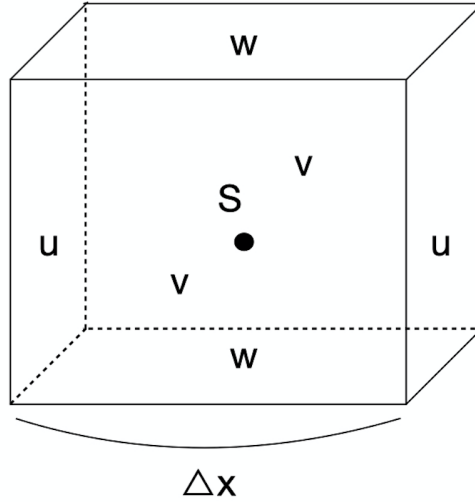


Figure 2.1: Cartoon showing the three-dimensional Arakawa-C grid. S denotes scalars (e.g., θ, π), dot is the scalars point in the middle of the cube. u is velocity in the x direction; v is velocity in the y direction; w is velocity in the z direction. Δx is the grid spacing in x direction

2.2 Simulation configuration

The calculations presented here are carried out using the CM1 (cm1r19.8). The horizontal domain is $2940 \text{ km} \times 2940 \text{ km}$ in size with 960 grid points in each direction. A horizontal grid spacing of 1 km is used in a central region $600 \text{ km} \times 600 \text{ km}$ of the domain. Outside this region, the grid spacing is stretched uniformly from 1 km to 12 km. There are 78 vertical levels from 0 km to 25 km. The vertical grid spacing is 100 m in the first 1 km and 500 m from 16 km to 25 km. Between 1 km and 16 km, the vertical grid spacing is stretched smoothly from 100 m to 500 m.

The initial condition is a prescribed, warm-cored, axisymmetric vortex in thermal wind balance in an otherwise quiescent environment. The vortex has a maximum tangential wind speed of 15 m s^{-1} at the surface at a radius of 100 km. The tangential wind decreases sinusoidally with height to zero at 20 km and is set to zero above this altitude. The corresponding balanced pressure, density and temperature fields are obtained using the method of Smith (2006).

The physical parameterization schemes include the Morrison double-moment microphysics scheme (Bryan and Morrison 2012), a simple planetary boundary layer parameterization (Bryan and Rotunno 2009a) and, because of the comparatively short duration of the integrations, no radiation scheme. A newtonian relaxation to the temperature field is used with a time scale of 10 days instead of the 12 h default value (see footnote 1 of Montgomery et al. 2020). Rayleigh damping layers with an e-folding time scale of 5 mins are implemented to suppress the reflection of internal gravity waves. These layers are above 20 km height and within 100 km of the open-radiative lateral boundaries. The Coriolis

parameter f is set to a constant value of $0.5 \times 10^{-4} \text{ s}^{-1}$, corresponding with a latitude of approximately 20°N . The sea surface temperature is taken to be constant and equal to 27°C . The Dunion moist tropical sounding (Dunion 2011) is used to characterize the background thermodynamic state. As in Persing et al. (2013), the horizontal and vertical mixing lengths are set as 700 m and 50 m, respectively, and are assumed constant in both space and time. These values are close to those recommended by Bryan (2012) in order to produce realistic hurricane structure. Montgomery et al. (2019) provide detailed justification for these selected parameter values.

2.3 Determination of the vortex centre

The determination of the minimum wind, which is used as the centre location for carrying out an azimuthal average, is as follows. First, the wind field at the surface is smoothed by applying a 1-2-1 filter in the zonal and meridional direction 60 times. Then, the minimum wind speed and its location are determined in the smoothed wind field in a $60 \text{ km} \times 60 \text{ km}$ box centred on the domain centre. For horizontal cross sections, the minimum wind used to define the centre is calculated in the same way, but at each particular height separately.

At an early stage of the study, I examined an alternative possibility to define the vortex centre as the location of minimum pressure in a similarly smoothed pressure field. Most of the time, the location of minimum pressure and minimum wind speed are close to each other below the outflow layer, but in the upper troposphere, the minimum pressure centre sometimes has a larger displacement: for example, in the mature phase, the horizontal displacement of the minimum pressure between 14 km and the surface is a little more than 1 km, but there is no displacement when centre location is based on the minimum wind speed. At earlier stages of development, the horizontal displacement of the minimum pressure between 14 km and the surface is 50 km while for minimum wind centre, it is only 13 km. For this reason, the minimum wind centre is preferred here.

Chapter 3

Experiment overview

A numerical experiment is carried out with the configuration described in Chapter 2. Model output data are stored every 15 min during the simulation for a total period of 120 hrs. For certain time periods (41-43 h, 59-61 h, 73-75 h), data output at 1 min intervals to facilitate accurate tendency calculations.

Section 3.1 shows the evolution of the tropical cyclone in the simulation. The azimuthally-averaged vertical structures are shown in Section 3.2. A discussion of the effects of the inflow layers on storm evolution is in Section 3.3. Section 3.4 shows the horizontal structure of upper outflow and inflow layers. A summary is provided in Section 3.5.

3.1 Vortex evolution

Figure 3.1(a) shows the time evolution of the maximum azimuthally-averaged¹ tangential wind speed, $Vmax$, and maximum total wind speed, $VTmax$, in the simulation. The determination of centre location for the azimuthal average is described in Chapter 2. The green line in Figure 3.1(a) shows the threshold slope for rapid intensification (RI), which is defined as a rate of at least $15 \text{ m s}^{-1}/\text{day}$. With this definition, the vortex enters an RI stage at about 30 h, a stage that lasts until about 65 h. Thereafter, the vortex enters a quasi-steady mature phase until about 90 h. The vortex intensifies again during 90 h to about 110 h, then enters a quasi-steady phase as the simulation is terminated at 120 h. The mature intensity measured by $Vmax$ is about 75 m s^{-1} . As in many previous studies (e.g. Nguyen et al. 2008), $VTmax$ is typically between 5 and 10 m s^{-1} larger than $Vmax$, a reflection of localized deep convection that first begins to form at about 5 h.

The time evolution of the maximum azimuthally-averaged radial wind speed in different vertical layers is shown in Figure 3.1(b). The maximum radial inflow in the boundary layer

¹The azimuthal average of a quantity α is defined by

$$\bar{\alpha} = \frac{1}{2\pi} \int_0^{2\pi} \alpha d\lambda,$$

where λ is the azimuthal angle.

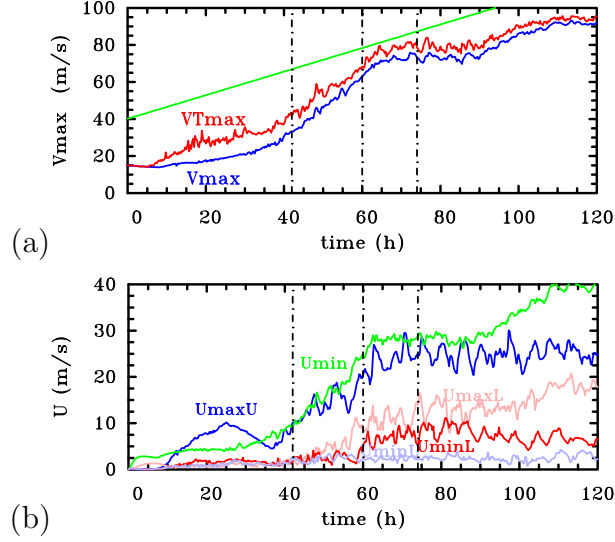


Figure 3.1: Time evolution of: (a) the maximum azimuthally-averaged tangential wind speed (V_{max} , blue) and maximum total wind speed (VT_{max} , red); (b) the magnitude of the maximum azimuthally-averaged radial wind speed in different layers: boundary layer inflow (U_{min} , green), upper tropospheric outflow (U_{maxU} , blue), boundary layer outflow (U_{maxL} , pink), inflow beneath the upper-level outflow (U_{minL} , red), inflow above the upper-level outflow (U_{minU} , light blue). The green line in panel (a) indicates a slope corresponding to the normal definition of RI (15 m s^{-1} per day). Vertical dashed lines indicate the times which are discussed in the text. The precise search layers for radial velocity extrema are: U_{min} , U_{maxL} , 0-3 km; U_{minL} , 8-13 km; U_{maxU} , 10-16 km; U_{minU} , 13-18 km.

(here, referring to the boundary layer as the layer adjacent to the surface, typically 1 km deep, where the radial inflow exceeds 2 m s^{-1} .), U_{min} , has a similar behaviour to V_{max} . It increases steadily from about 30 h, reaches a maximum magnitude at the beginning of the mature stage and subsequently levels off. Typically, U_{min} is less than 40% of V_{max} . U_{min} increases from about 90 h to about 110 h, then levels off again.

The maximum outflow just above the top of the boundary layer inflow layer, U_{maxL} , begins to increase in a time-mean sense after about 45 h and levels off during the mature stage, but it has much larger fluctuations than the maximum inflow beneath the upper-level outflow, U_{minL} , beyond 54 h.

The maximum in the upper-layer outflow, U_{maxU} , has a peak near 25 h, followed by a decline to 37 h, just after the start of RI. This peak is associated with an early episode of some individual deep convection cells. Subsequently, U_{maxU} increases rapidly throughout the RI phase, but levels off in a time-mean sense after about 65 h. Nevertheless, like U_{maxL} , it fluctuates markedly after about 48 h.

The maximum inflow immediately below the upper-layer outflow strengthens in a time-mean sense from about 58 h, reaches a peak at about 82 h, after which it declines a little. Moreover, like U_{maxL} and U_{maxU} , it exhibits significant fluctuations.

The maximum inflow immediately above the main upper-level outflow layer, $U_{min}U$, increases slightly from near the start of the RI period, but remains less than about 2.5 m s^{-1} . Its behaviour does not appear to have a strong connection with other metrics of vortex development.

3.2 Azimuthally-averaged vertical structure

The left columns of Figure 3.2 show the azimuthally- and one-hour time-averaged tangential velocity, \bar{v} , at selected times with the corresponding surfaces of absolute angular momentum, $\bar{M} = r\bar{v} + \frac{1}{2}fr^2$, superimposed. Here f is the Coriolis parameter and r is the radius. Panel (a) is for 42 h, a few hours after the RI period commences, panel (c) is for 60 h, a few hours before the quasi-steady period is reached, and panel (e) is for 74 h, which is in the middle of the quasi-steady period. The right columns of Figure 3.2 show the corresponding similarly averaged radial velocity, \bar{u} , with selected contours of vertical velocity superimposed.

The tangential velocity fields have similar characteristics to those described in many previous studies, the maximum occurring at a low altitude near the top of a shallow layer of strong inflow adjacent to the sea surface and well within a radius of 50 km. At radii larger than about 75 km at 42 and 60 h, the maximum tangential wind occurs in the low to middle troposphere, at least to about 250 km radius, a feature evidenced most clearly by the location of the inward-pointing nose of the \bar{M} -surfaces in this region. At 74 h, the middle tropospheric maximum extends only to about 160 km radius.

Invoking the classical paradigm for tropical cyclone intensification that is based on the approximate material conservation of absolute angular momentum above the frictional boundary layer (Montgomery and Smith 2014, 2017), this maximum must be associated with a relatively strong time-mean inflow at this level. A notable feature of the \bar{M} -surfaces at all times shown is their quasi-horizontal orientation in the vicinity of the upper tropospheric outflow with a propensity to fold over in this region. At large radii in the region of outflow, typically larger than 200 km at the later times, the tangential flow becomes anticyclonic, a well known feature that, again, is a consequence of the approximate conservation of absolute angular momentum in the outflow.

The radius of maximum tangential wind generally increases with height in the low to middle troposphere as shown by the yellow line in Figures 3.2(a,c,e), although at 74 h (panel (e)), there is a sharp decrease in radius marking a second wind maximum in the eyewall updraught complex. This maximum is an indication of a quasi-stationary centrifugal wave generated by the recoil of the shallow outflow just above where the boundary layer terminates (see e.g. Montgomery and Smith 2017, Stern et al. 2020).

The right panels of Figure 3.2 show the evolution of the radial flow between 42 h and 74 h. The prime focus here is on the development of the upper-level outflow and the layers of inflow above and below it. At 42 h, the outflow layer extends over a depth of about 11–15 km near its source, just inside a radius of 40 km, and it tapers slightly with increasing radius. The maximum velocity in the outflow layer at this stage is about 9.6 m s^{-1} . There

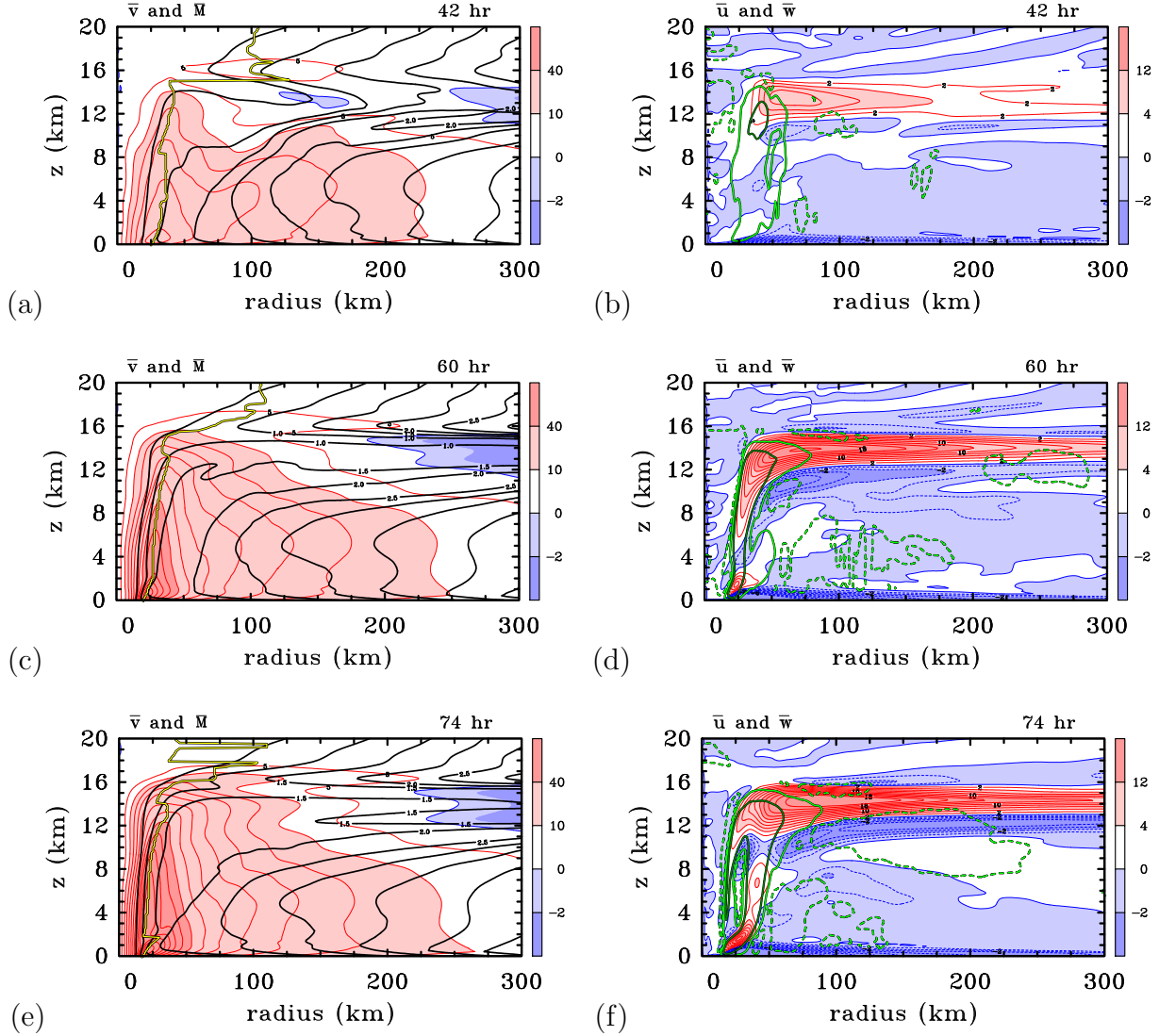


Figure 3.2: Radius-height cross sections of one-hour time-averaged and azimuthally-averaged fields from the numerical model simulation at 42 h (upper panels), 60 h (middle panels) and 74 h (lower panels): (a,c,e) tangential velocity component, \bar{v} and surfaces of absolute angular momentum, \bar{M} ; (b,d,f) radial velocity component, \bar{u} , and vertical velocity component, \bar{w} . Contour interval for \bar{v} : 5 m s^{-1} ; for \bar{M} : $0.5 \times 10^6 \text{ m}^2 \text{ s}^{-1}$; for 2 m s^{-1} when $\bar{u} > 0$, 1 m s^{-1} when $\bar{u} < 0$. For \bar{w} three green contours are shown: $+0.25 \text{ m s}^{-1}$ (solid light), $+1.0 \text{ m s}^{-1}$ (solid dark) and -0.02 m s^{-1} (dashed). The quantities \bar{v} and \bar{u} are shaded with values indicated on the colour bar. Red solid contours indicate positive values, blue dashed contours indicate negative values. Contours of \bar{M} are black, those for \bar{w} are green. The yellow curve indicates the radius of maximum tangential wind at each height.

is a shallow layer of inflow at most radii below the outflow with two local maxima, one with a speed of 1.6 m s^{-1} at a radius just inside that of maximum outflow and another

slightly weaker one near a radius of 200 km.

By 60 h, the lower inflow layer between 9 and 11 km has strengthened and now extends to the outer radius shown (300 km), with a maximum speed of 4.8 m s^{-1} , while a shallower, but weaker layer of inflow has developed just above the outflow layer between 15 and 17 km. In addition, there are weaker layers of inflow, one between about 8 and 10 km and the other between 17 and 19 km, but these would appear to be transient features as they are not prominent at 74 h. At 60 h, the mean eyewall updraught, delineated by the 0.25 m s^{-1} contour of mean vertical velocity has strengthened since 42 h. By 74 h, strengthening of the upper-level outflow and the inflow layers sandwiching it are evident (panel (f)) as well as a broadening of the mean eyewall updraught complex.

The green dashed contours in the right panels of Figure 3.2 enclose areas of mean subsidence with sinking rates larger than 0.02 m s^{-1} . At 42 h, these areas are generally small and patchy, but at later times they become more coherent. At 60 h and 74 h there is a shallow area of enhanced subsidence just above and beyond where the eyewall terminates, suggesting that the eyewall updraught overshoots its equilibrium level. There are large areas of enhanced subsidence also in the low to mid troposphere, outside the eyewall updraught complex, inside a radius between about 150-200 km, and on the inner edge of this complex.

At 60 h, there is a region of enhanced subsidence beyond 200 km radius which overlaps with part of the outflow layer and all of the inflow layer below it. There is another region of subsidence between 50 and 75 km radius where this inflow layer terminates adjacent to the eyewall updraught complex.

At 74 h, a large area of enhanced subsidence has developed below the outflow layer between about 80 km and 210 km. This region overlaps with the inflow layer just below the outflow. At this time there is an inflow maximum also within the eyewall complex, itself, which is connected to a narrow region of subsidence separating two areas of eyewall updraught. Animations of the fields indicate that this deep finger of subsidence and the inflow maximum to which it is connected are transient features, which by 76 h have disappeared (not shown). I show later in section 3.4 that the flow in the upper troposphere, including the eyewall region, has a marked azimuthal wavenumber-one asymmetry at these times.

Having documented the existence and evolving structure of upper-level inflow layers, the natural question that emerges is what their impact is on the storm structure? I address this question in the next section.

3.3 Effects of the inflow layers on storm evolution

Animations of vertical cross sections at 15 minute intervals shows a progressive inward movement of the \bar{M} -surfaces with maximum displacement in the inflow layer just above the outflow layer. At lower altitudes, the animations show a pronounced folding of individual \bar{M} -surfaces to produce transient ‘z-like’ patterns with an outward-pointing nose at large radius in the outflow layer and an inward pointing nose that is sometimes in the

outflow layer and at other times in the inflow layer below it. These upper-level features are exemplified in the left column of Figure 3.2 and are to be expected as the \bar{M} surfaces are initially closer to the vertical than to the horizontal and \bar{M} is approximately materially conserved in the upper troposphere, at least beyond the eyewall updraught. These \bar{M} -surfaces are strongly distorted by the vertical gradient of mean radial flow.

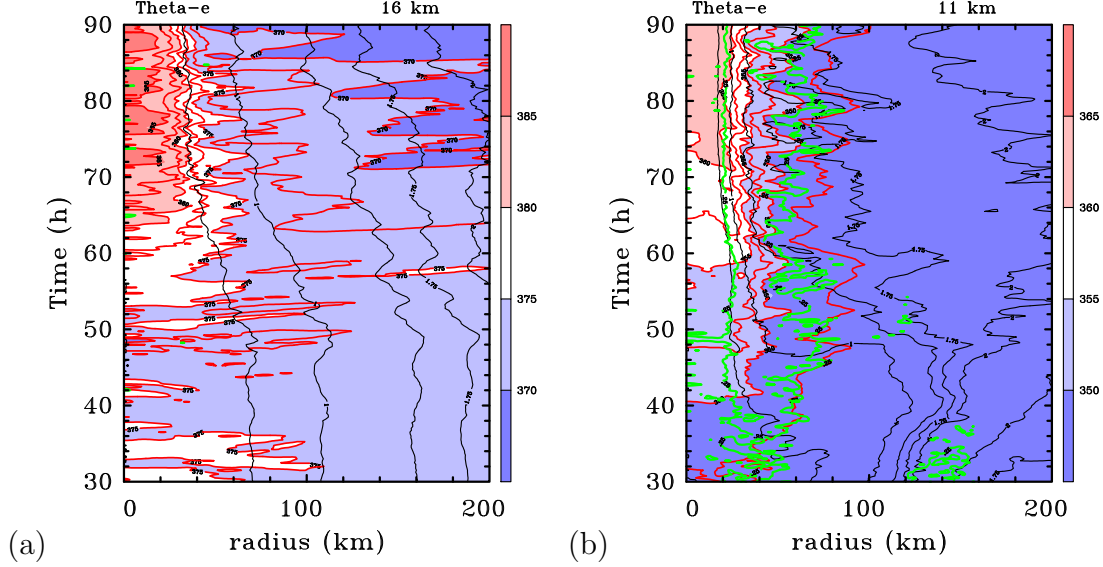


Figure 3.3: Radius-time cross sections of azimuthally-averaged pseudo-equivalent potential temperature, $\bar{\theta}_e$, absolute angular momentum, \bar{M} , and vertical velocity \bar{w} at (a) 16 km, and (b) 11 km. Contour interval for $\bar{\theta}_e$ is 2.5 K; for \bar{M} , $0.5 \times 10^6 \text{ m}^2 \text{ s}^{-1}$. Shown also is the \bar{M} with the value $1.75 \times 10^6 \text{ m}^2 \text{ s}^{-1}$. Contours of \bar{w} (in green) has the value 0.25 m s^{-1} and indicates the approximate location of the eyewall updraught. Contours of $\bar{\theta}_e$ in red with shading indicated on the colour bar. Contours of \bar{M} are black.

Figure 3.3 shows radius-time cross sections of \bar{M} -contours at altitudes of 16 km and 11 km, together with similar contours of azimuthally-averaged pseudo-equivalent potential temperature, $\bar{\theta}_e$. Also shown at 11 km is the contour of vertical velocity with a magnitude of 0.25 m s^{-1} to show the approximate location of the eyewall updraught complex at this level. Beyond this updraught complex, the quantities \bar{M} and $\bar{\theta}_e$ should be approximately materially conserved by the mean radial flow. The pseudo-equivalent potential temperature was calculated using Eq.43 in Bolton (1980):

$$\bar{\theta}_e = T \left(\frac{p_{00}}{p} \right)^{0.2854(1-0.28q)} \exp \left[q(1 + 0.81q) \left(\frac{3376}{T_l} - 2.54 \right) \right], \quad (3.1)$$

where T is the temperature, p is the pressure, p_{00} is the reference pressure, T_l is the condensation temperature and q is the water vapor mixing ratio.

At 16 km altitude, which is within the inflow layer above the outflow layer and slightly above the eyewall updraught complex, an inward migration of the \bar{M} -surfaces is clearly

evident, at least within a radius of 180 km. This inward migration implies a spin up of the mean tangential wind at this level. There is an inward migration of the \bar{M} -surfaces at 11 km altitude also, but in the inner region, within the eyewall updraught, the inward migration can be attributed in part to the upward advection of tangential momentum. There is an event in Figure 3.3(b) where an \bar{M} -surface appears to form at a finite radius and subsequently move inwards (e.g. at 49 h at a radius of about 100 km). This occurrence is associated with the passage of the inward and downward moving tip of a folding \bar{M} -surface through the level in question. After about 60 h as the inflow below the outflow layer strengthens, at radii larger than 100 km, the migration occurs in oscillatory pulses with a period of a few hours. Whatever the circumstance, the inward migrating \bar{M} -surface implies a spin up of the mean tangential wind within this inflow layer.

Like the \bar{M} -surfaces, the $\bar{\theta}_e$ -surfaces are approximately materially conserved in three dimensions, but these surfaces are nearly horizontal at the initial time. They are subsequently distorted in a different way. At 16 km altitude (panel (a)), $\bar{\theta}_e$ shows little change with the contour interval chosen until just after 60 h, except for a slight reduction at most radii (between 35 and 55 h) and small positive pulses inside a radius of 50 km. The latter reflects the effect of convective updraughts that occasionally reach this level during the earlier period of evolution. Beyond 60 h, the eyewall convective complex begins to persist at this altitude as reflected in the increase of $\bar{\theta}_e$ values most prominently within about 60 km radius. As there is radial inflow at this level (see e.g. the right panels of Figure 3.2), this region of elevated $\bar{\theta}_e$ values remains radially confined.

The situation is similar at 11 km altitude (panel (b)), where the increase in $\bar{\theta}_e$ values occurs a little earlier at about 40 h, but as at 16 km, the increase remains radially confined by the inflow. The presence of a weak negative radial gradient of $\bar{\theta}_e$ at this level is indicated by the red contour ($\bar{\theta}_e = 347.5$ K) between 40 km and 100 km radius and beyond about 45 h. Note that the fluctuations in the radial location of this contour are closely correlated with those of \bar{M} indicating that beyond the eyewall updraught complex, both $\bar{\theta}_e$ and \bar{M} are approximately conserved in radial displacements at 11 km.

Animations of vertical cross sections of $\bar{\theta}_e$ and \bar{M} show that the surfaces of these quantities have significantly different structure during much of the intensification phase, but with some tendency for the surfaces to become more parallel in the eyewall updraught region during the later stages of intensification (after about 72 h) and into the mature stage (not shown). A particularly striking feature of these surfaces during this later stage is the way in which advection by the radial inflow beneath the outflow layer leads to a more vertically erect eyewall and effectively reinforcing the eyewall $\bar{\theta}_e$ front in the upper troposphere.

The vertically coherent eyewall front is evident in Figure 3.4, which shows vertical cross sections of $\bar{\theta}_e$ at 42 h, 60 h and 74 h with the \bar{M} -surfaces and selected contours of radial and vertical velocity superimposed. The distribution of $\bar{\theta}_e$ shows the classical structure. The principal features are: the mid-tropospheric minimum beyond a radius of about 100 km, increasing in prominence with radius; the tendency for the isopleths of $\bar{\theta}_e$ to become close to vertical in the eyewall updraught complex; and the tendency for these isopleths to slope outwards and become close to horizontal in the upper tropospheric outflow layer. There

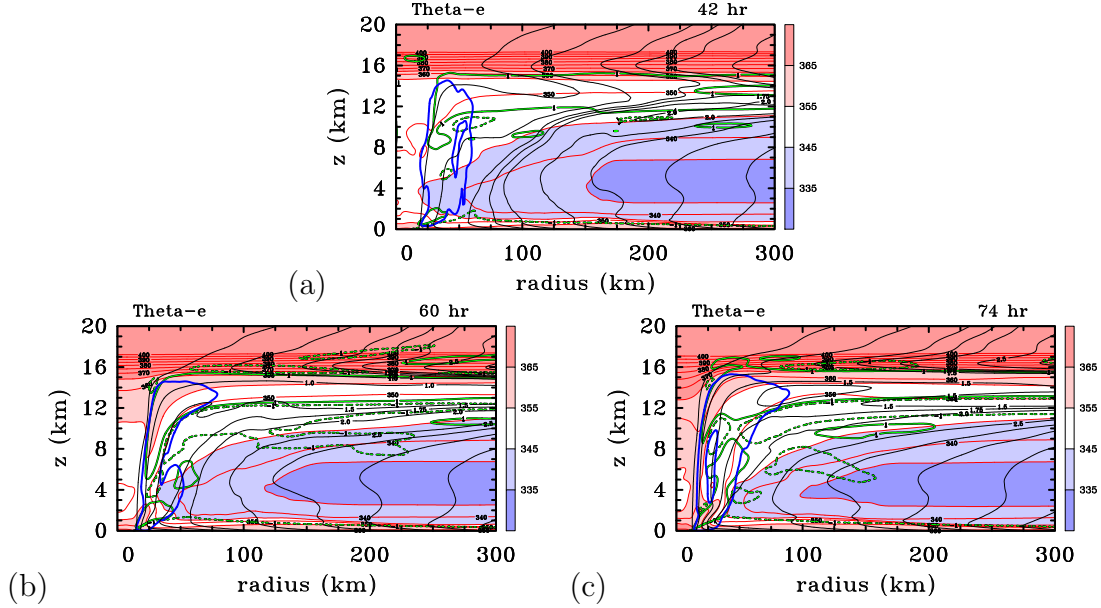


Figure 3.4: Radius-height cross sections of pseudo-equivalent potential temperature, $\bar{\theta}_e$, and absolute angular momentum, \bar{M} at (a) 42 h, (b) 60 h and (c) 74 h. Superimposed on each panel are two contours of the radial velocity component \bar{u} and one contour of the vertical velocity component, \bar{w} . All fields are azimuthally-averaged and time-averaged for one hour. Contour interval for $\bar{\theta}_e$ is 5 K; for \bar{M} , $0.5 \times 10^6 \text{ m}^2 \text{ s}^{-1}$, with the \bar{M} -surfaces in black and the $\bar{\theta}_e$ -surfaces in red with shading indicated on the colour bar. Shown also is the \bar{M} with the value $1.75 \times 10^6 \text{ m}^2 \text{ s}^{-1}$. The contours of \bar{u} are green solid contours as 1 m s^{-1} and dashed contours as -1 m s^{-1} and the thick blue contour of \bar{w} has the value 0.25 m s^{-1} to indicate the approximate location of the eyewall updraught.

is an approximate congruence between the $\bar{\theta}_e$ and \bar{M} surfaces in the eyewall updraught complex above about 5 km and in the upper troposphere where the air ascending in the eyewall flows outwards.

Throughout much of the troposphere, $\bar{\theta}_e$ has a negative radial gradient. This is, in part, a reflection of the structure in the boundary layer. Although this description broadly captures the basic reason for the interior $\bar{\theta}_e$ structure, the inner-core region underneath the eyewall complex (radius $< 25 \text{ km}$) exhibits a somewhat more intricate structure. Here there is a local region of enhanced radial gradient in which the eye appears to act as a source of high $\bar{\theta}_e$ air (Figure 3.4). This air rises into the eyewall updraught, effectively feeding the updraught with enhanced $\bar{\theta}_e$. The finger of enhanced $\bar{\theta}_e$ is clearly evident at 60 h and becomes markedly more pronounced at 74 h. This low-level $\bar{\theta}_e$ structure has been observed and analyzed elsewhere by Zhang et al. (2001) with a similar interpretation.

The role of nonlinear boundary layer dynamics in creating this corner structure is certainly an interesting and important topic, but lies outside the scope of the current study.

Returning to the upper-level structure of $\bar{\theta}_e$, and recalling the approximate material

conservation of this quantity, a prominent feature to note is the development between 60 h and 74 h of subsidence of lower-stratospheric air into the upper part of the eye with the strongest subsidence occurring in a finger along the inside edge of the eyewall (Figure 3.4(b) and (c)). Another prominent feature is the broadening of the eyewall updraught complex during this period, which is related, at least in part, to the (transient) splitting of the updraught at 74 h.

The effect of the upper-layer inflow on the $\bar{\theta}_e$ field is harder to discern from a comparison of panels (a), (b) and (c) of Figure 3.4 than it is in the animations. This is due to the broadening of the eyewall updraught complex during this period, a broadening that is evident also in the $\bar{\theta}_e$ pattern in Figure 3.3(b), and the fact that $\bar{\theta}_e$ values in the updraught have increased. However, as suggested by the inward movement of the $\bar{\theta}_e$ surfaces beyond the eyewall updraught complex in Figure 3.3(b), the convergent inflow must play a role in tightening the radial gradient of $\bar{\theta}_e$ in the upper troposphere on the outside of the eyewall.

3.4 Horizontal structure of outflow and inflow layers

Figure 3.5–3.8 shows horizontal cross sections of the radial velocity component u (red/blue) along with horizontal wind vectors and vertical velocity w (yellow) at different levels at selected times. The vortex centre at each level, indicated by the hurricane symbol, is calculated in the same way as described in the appendix.

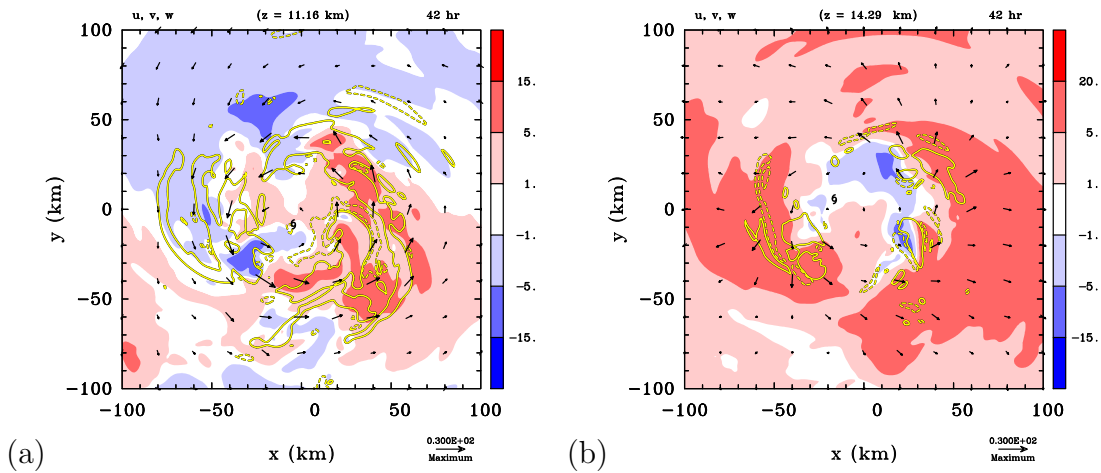


Figure 3.5: Horizontal cross sections of the instantaneous radial velocity component, u (shaded values), horizontal wind vectors and vertical velocity, w (yellow contours), at 42 h. Left column for a height of 11 km, right column for a height of 14 km. Radial velocity shaded as indicated on the colour bar in m s^{-1} . The maximum reference wind vector is 30 m s^{-1} shown on lower right corner. Two contours of w : solid yellow contour with black border, 0.5 m s^{-1} , dashed yellow contour with black border, -0.5 m s^{-1} . The vortex centre, indicated by the hurricane symbol, is defined as the location of minimum wind speed at each particular level.

Figure 3.5(a) shows cross section at a height of approximately 11 km (actually 11.16 km) that is generally within the upper-level inflow layer beneath the outflow layer, while Figure 3.5(b) show the fields at a height of approximately 14 km (actually 14.29 km), which is within the outflow layer, itself. Early on in the intensification stage, at 42 h, there is outflow in all sectors beyond a radius of about 40 km at 14 km height (panel (b)), with mostly inflow inside this radius. The inflow is seen to occur on the inside edges of deep convective cores, which lie predominantly outside a radius of 30-40 km. The situation at 11 km is rather different (panel (a)), with mostly inflow in the northern half of the domain and mostly outflow in the southern half (here referring to the y -direction as north, even though in the problem as formulated on an f -plane, there is no preferred direction). Clearly the inflow layer at this altitude and time is quite asymmetric.

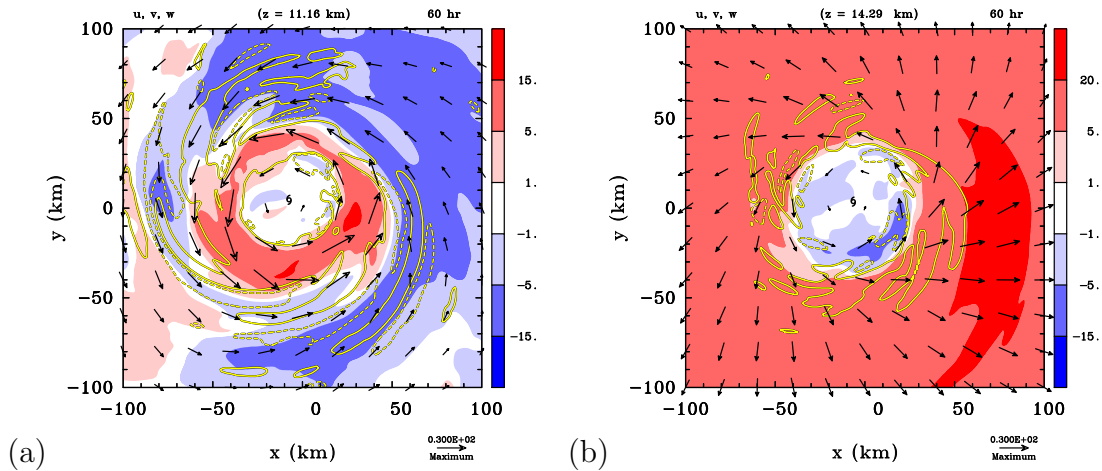


Figure 3.6: Horizontal cross sections of the instantaneous radial velocity component, u (shaded values), horizontal wind vectors and vertical velocity, w (yellow contours), at 60 h. Left column for a height of 11 km, right column for a height of 14 km. Radial velocity shaded as indicated on the colour bar in m s^{-1} . The maximum reference wind vector is 30 m s^{-1} shown on lower right corner. Two contours of w : solid yellow contour with black border, 0.5 m s^{-1} , dashed yellow contour with black border, -0.5 m s^{-1} . The vortex centre, indicated by the hurricane symbol, is defined as the location of minimum wind speed at each particular level.

At 60 h, towards the end of the intensification stage, the outflow at 14 km has strengthened and is to a first approximation symmetric with outflow at all azimuths about the centre (Figure 3.6(b)). The inflow at 11 km ((Figure 3.6(a))) has strengthened also, but is seen to retain a significant degree of asymmetry, being most extensive in the northeastern sector and least extensive in the southwestern sector. Broadly, the inflow lies outside an annulus of outflow coinciding with the eyewall updraught at this altitude. Noteworthy is the fact that the region of inflow with a magnitude exceeding 5 m s^{-1} contains elongated bands of both enhanced ascent and descent that are presumably some form of wave motions (inertia-buoyancy waves and/or vortex Rossby waves).

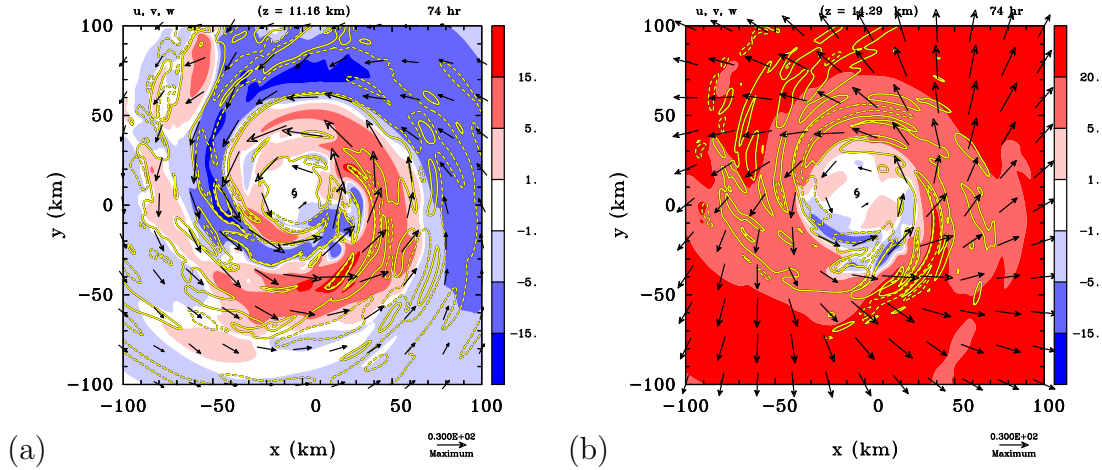


Figure 3.7: Horizontal cross sections of the instantaneous radial velocity component, u (shaded values), horizontal wind vectors and vertical velocity, w (yellow contours), at 74 h. Left column for a height of 11 km, right column for a height of 14 km. Radial velocity shaded as indicated on the colour bar in m s^{-1} . The maximum reference wind vector is 30 m s^{-1} shown on lower right corner. Two contours of w : solid yellow contour with black border, 0.5 m s^{-1} , dashed yellow contour with black border, -0.5 m s^{-1} . The vortex centre, indicated by the hurricane symbol, is defined as the location of minimum wind speed at each particular level.

At 74 h (Figure 3.7), during the quasi-steady mature stage, the outflow at 14 km exceeds 20 m s^{-1} beyond a radius of 50-100 km that depends on azimuth with weak inflow within 20 km in a region to the south of the centre. At 11 km, however, the pattern of inflow and outflow remains asymmetric with an inward counterclockwise spiralling band of inflow extending from about 120 km east-southeast of the vortex centre to about 50 km east of the centre, where it terminates. At radii inside this band is an inward counterclockwise spiralling band of outflow that extends from approximately southwest of the vortex centre to the north of the centre.

The pattern of azimuthal-mean radial and vertical motion at 74 h in Figure 3.2(f) shows a deep, radially-confined downdraught that apparently splits the eyewall updraught. The upper portion of this downdraught corresponds to an upper-level inflow maximum at a radius of about 30 km and an altitude between 9 and 10 km. I investigate the degree of symmetry of this feature in Figure 3.8, which shows similar horizontal cross sections to those in Figures 3.7, but at altitudes of 6.1 km and 9.9 km. Like the higher altitudes at this time, the pattern of inflow and outflow at both levels exhibits a marked asymmetry.

At 9.9 km altitude (Figure 3.8(b)), the pattern has a prominent azimuthal wavenumber-one component, with spiral regions of inflow and outflow, much like the pattern at 11 km in Figure 3.7(a) and the orientation of the spiral pattern is much the same. The main difference is the localized region of strong inflow in the east to southeast sector at 9.9 km, at radii between about 15 and 35 km, which would account for the local maximum of inflow seen in Figure 3.2(f). On the broad scale, it is apparent that most of the strongly

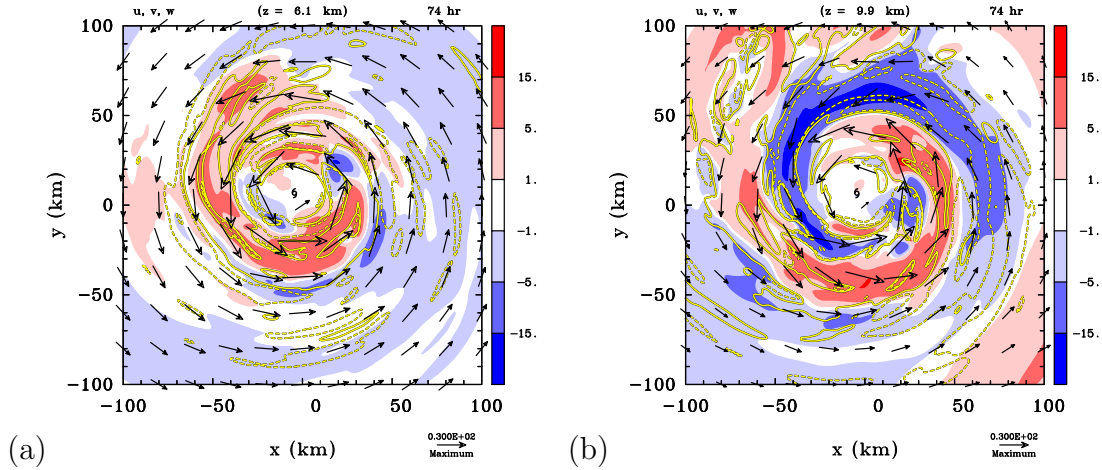


Figure 3.8: Horizontal cross sections of the instantaneous radial velocity component, u (shaded values), horizontal wind vectors and vertical velocity, w (yellow contours), at heights of (a) 6.1 km and (b) 9.9 km, both at 74 h. Radial velocity shaded as indicated on the colour bar in m s^{-1} . The maximum reference wind vector is 30 m s^{-1} shown on lower right corner. Two contours of w : solid yellow contour with black border, 0.5 m s^{-1} , dashed yellow contour with black border, -0.5 m s^{-1} . The vortex centre, indicated by the hurricane symbol, is defined as the location of minimum wind speed at each particular level.

inflowing air is descending. At 6.1 km altitude (Figure 3.8(a)), the localized region of inflow is smaller in area and rotated slightly counterclockwise. At both altitudes, only part of the region of localized inflow coincides with a region of subsidence.

3.5 Summary

Three-dimensional numerical simulations of tropical cyclone intensification with moderately high vertical resolution have been used to analyze the development of a layer of strong inflow beneath the upper tropospheric outflow layer as well as, in some cases, a shallower layer of weaker inflow above the outflow layer. The calculations pertain to the prototype problem for tropical-cyclone intensification, which considers the evolution of a vortex on an f -plane in a quiescent environment starting from an initially-symmetric, moist, cloud-free vortex over a warm ocean.

The inflow layers adjacent to the upper-level outflow were shown to have a role in modifying the vortex structure in the upper troposphere. The inflow layer above the outflow layer leads to a spin up of the tangential winds there, thereby extending the cyclonic circulation of the hurricane vertically. In addition, the inflow acts to resist the radial spread of air with high pseudo-equivalent potential temperature at this level. The inflow layer below the outflow layer leads also to a spin up of the cyclonic tangential winds in the inflow layer and would appear to contribute to an increase of the radial gradient of

pseudo-equivalent potential temperature at the outer edge of the eyewall. The inflow layers adjacent to the upper-level outflow were shown to be more asymmetric than the outflow layer, itself, having a low azimuthal wavenumber flow asymmetry.

Chapter 4

Balance theory

A scale analysis of the equations of motion for an axisymmetric rapidly-rotating tropical cyclone-like vortex shows that, to a first approximation, over much of the troposphere, the tangential wind field and temperature field are in gradient wind balance and hydrostatic balance, i.e. thermal wind balance (Willoughby 1979). Regions where thermal wind balance does not hold include the frictional boundary layer and the upper tropospheric outflow layer. Assuming that thermal wind balance holds everywhere enables one to derive an equation for the streamfunction of the overturning circulation driven by diabatic heating and near-surface friction, processes that, in the absence of such a circulation, would drive the vortex away from thermal wind balance. This streamfunction equation is generally referred to as the Sawyer-Eliassen equation and has a variety of forms.

The Sawyer-Eliassen equation is a key equation in the formulation of a prognostic axisymmetric balance theory for tropical cyclone evolution (Sundqvist 1970a,b; Schubert and Alworth 1982; Möller and Smith 1994; Smith et al. 2018a; Smith and Wang 2018) and it has formed a basis for many diagnostic studies of tropical cyclone structure. In the latter studies, the Sawyer-Eliassen equation is solved diagnostically for the secondary circulation in the presence of a prescribed forcing mechanism (or mechanisms), possibly with an examination of the instantaneous tangential wind tendency accompanying the calculated overturning circulation (e.g. Smith 1981; Shapiro and Willoughby 1982; Schubert and Hack 1982; Hack and Schubert 1986; Rozoff et al. 2008; Bui et al. 2009; Pendergrass and Willoughby 2009; Wang and Wang 2013; Abarca and Montgomery 2014; Smith et al. 2014a; Ohno and Satoh 2015; Heng and Wang 2016; Heng et al. 2017; Montgomery and Persing 2020).

The solution of the Sawyer-Eliassen equation requires that the equation be globally elliptic, a condition that is usually satisfied by the choice of the vortex in idealized diagnostic studies, but is frequently not satisfied when the axisymmetric vortex structure is determined as an azimuthal average from the numerical model output of a tropical cyclone simulation. When this happens, the solution can be carried only by adjusting the coefficients in the Sawyer-Eliassen equation in the unstable regions to keep the equation elliptic globally. In essence, regularization, as this method is called, is an *ad hoc* procedure and various methods have been used. One method was devised by Möller and Shapiro

(2002) in a case study of Hurricane Opal (1995) and modifications thereof were used by Bui et al. (2009); Smith et al. (2014a, 2018a) and Smith and Wang (2018). An alternative method was suggested by Wirth and Dunkerton (2006), who effectively flattened out the M -surfaces in regions where the flow becomes inertially unstable, i.e. where $\partial M/\partial r < 0$. Despite the fact that the flattening out was accomplished using a scheme that globally conserves angular momentum, it makes the Sawyer-Eliassen equation parabolic in these regions, but not elliptic as required by the code they used to solve the equation¹. But Some authors referenced above have not checked whether their Sawyer-Eliassen equation is globally elliptic (e.g. Sundqvist 1970a,b; Ohno and Satoh 2015) raising questions about the convergence of their solution.

The purpose of this chapter is to develop a framework for exploring and understanding some of the local and global consequences of regularization and to investigate improved ways to carry out the regularization. In doing so, we highlight some fundamental limitations of regularization. The mathematical background of balance theory will be described in section 4.1. In section 4.2 and section 4.3, a membrane analogy and a more realistic configuration vis-à-vis the atmosphere have been used to understand the behaviour of elliptic second-order partial differential equations. Section 4.4 shows how regularization schemes have been designed in such problems and in section 4.5 related tests in an idealized three-dimensional numerical simulation are analyzed. Then a similar discussion of regularization in regions of large vertical shear are discussed in section 4.6. Finally, A discussion is given in Section 4.7.

4.1 The Sawyer-Eliassen equation

For an axisymmetric vortex with approximate gradient wind and hydrostatic balance in cylindrical height coordinates (r, z) where r is the radius and z is the height,

$$\frac{\partial \bar{p}}{\partial r} = \bar{\rho}(f\bar{v} + \frac{\bar{v}^2}{r}), \quad (4.1)$$

and

$$\frac{\partial \bar{p}}{\partial z} = -\bar{\rho}g, \quad (4.2)$$

where \bar{p} is the pressure, $\bar{\rho}$ is the density, f is the Coriolis forces, \bar{v} is the tangential velocity component, g is the acceleration due to gravity.

Eliminating \bar{p} by taking the derivative of Eq.(4.1) with respect to z and taking the derivative of Eq.(4.2) with respect to r , the thermal wind equation could be obtained as:

$$g\frac{\partial \ln \bar{\rho}}{\partial r} + (f\bar{v} + \frac{\bar{v}^2}{r})\frac{\partial \ln \bar{\rho}}{\partial z} = -(\frac{2\bar{v}}{r} + f)\frac{\partial \bar{v}}{\partial z} \quad (4.3)$$

¹The solution code is described in the appendix of Wirth (1995), who states that “The resulting finite-difference equation is solved with the help of a multigrid algorithm (routine D03EDF) from the NAG Fortran library, which readily returns the desired solution so long as the equation is elliptic everywhere in the domain”.

Defining

$$C = f\bar{v} + \frac{\bar{v}^2}{r}, \quad (4.4)$$

which denotes the sum of centrifugal and Coriolis forces per unit mass, Eq.(4.3) may be written as

$$g \frac{\partial \ln \bar{\rho}}{\partial r} + C \frac{\partial \ln \bar{\rho}}{\partial z} = -\frac{\partial C}{\partial z} \quad (4.5)$$

Here, the density is related to pressure and potential temperature $\bar{\theta}$ by

$$\bar{\rho} = \bar{p}_{00} \pi^{\frac{1}{\kappa}-1} / (R_d \bar{\theta}) \quad (4.6)$$

where, \bar{p}_{00} is a standard reference pressure, $\pi = (\bar{p}/\bar{p}_{00})^\kappa$ is the Exner function, $\kappa = R_d/C_p$, R_d is the specific gas constant for dry air, and C_p is the specific gas constant for dry air at constant pressure.

Now, taking logarithms on both sides, and defining $\chi = 1/\bar{\theta}$,

$$\ln \bar{\rho} = \kappa \ln \bar{p}_{00} + (1 - \kappa) \ln \bar{p} - \ln \bar{\theta} = \text{constant} + (1 - \kappa) \ln \bar{p} + \ln \chi \quad (4.7)$$

so that,

$$\frac{d\bar{\rho}}{\bar{\rho}} = \frac{d\chi}{\chi} + (1 - \kappa) \frac{d\bar{p}}{\bar{p}} \quad (4.8)$$

then, Eq.(4.5) may be reformulated as

$$g \frac{\partial \ln \chi}{\partial r} + C \frac{\partial \ln \chi}{\partial z} = -\frac{\partial C}{\partial z} \quad (4.9)$$

The azimuthal momentum equation and thermodynamic equation may be written in the following form,

$$\frac{\partial \bar{v}}{\partial t} + \bar{u}(f + \zeta) + \bar{w} \frac{\partial \bar{v}}{\partial z} = -\dot{V} \quad (4.10)$$

and

$$\frac{\partial \chi}{\partial t} + \bar{u} \frac{\partial \chi}{\partial r} + \bar{w} \frac{\partial \chi}{\partial z} = -\chi^2 \dot{\theta} \quad (4.11)$$

where, \bar{u} is the radial velocity component, \bar{w} is the vertical velocity component. $\zeta = (1/r)\partial(r\bar{v})/\partial r$ is the vertical component of relative vorticity. $\dot{\theta} = d\bar{\theta}/dt$ is the material derivative of the diabatic heating rate and $-\dot{V}$ is the tangential momentum sink.

Taking time derivative of Eq.(4.9) and substitution of the time derivatives from Eq.(4.10) and Eq.(4.11) gives

$$\begin{aligned} & \frac{\partial}{\partial r} \left[-g \frac{\partial \chi}{\partial z} \bar{w} + \frac{\partial}{\partial z} (\chi C) \bar{u} \right] + \\ & \frac{\partial}{\partial z} \left[- \left(\chi \xi (\zeta + f) + C \frac{\partial \chi}{\partial r} \right) \bar{u} - \frac{\partial}{\partial z} (\chi C) \bar{w} \right] = \\ & g \frac{\partial}{\partial r} (\chi^2 \dot{\theta}) + \frac{\partial}{\partial z} (C \chi^2 \dot{\theta}) + \frac{\partial}{\partial z} (\chi \xi \dot{V}) \end{aligned} \quad (4.12)$$

where $\xi = f + 2\bar{v}/r$ is twice the local absolute angular velocity.

The radial and vertical velocity components, \bar{u} and \bar{w} , may be obtained using the formulae: $\bar{u} = -(1/\bar{\rho}r)(\partial\psi/\partial z)$ and $\bar{w} = (1/\bar{\rho}r)(\partial\psi/\partial r)$, respectively, which ensure that the continuity equation is satisfied. Then, the most general form of the Sawyer-Eliassen equation in cylindrical coordinates (r, z) may be written as

$$\begin{aligned} & \frac{\partial}{\partial r} \left[-g \frac{\partial \chi}{\partial z} \frac{1}{\bar{\rho}r} \frac{\partial \psi}{\partial r} - \frac{\partial}{\partial z} (\chi C) \frac{1}{\bar{\rho}r} \frac{\partial \psi}{\partial z} \right] + \\ & \frac{\partial}{\partial z} \left[\left(\chi \xi (\zeta + f) + C \frac{\partial \chi}{\partial r} \right) \frac{1}{\bar{\rho}r} \frac{\partial \psi}{\partial z} - \frac{\partial}{\partial z} (\chi C) \frac{1}{\bar{\rho}r} \frac{\partial \psi}{\partial r} \right] = \\ & g \frac{\partial}{\partial r} (\chi^2 \dot{\theta}) + \frac{\partial}{\partial z} (C \chi^2 \dot{\theta}) + \frac{\partial}{\partial z} (\chi \xi \dot{V}) \end{aligned} \quad (4.13)$$

The left-side of Equation (4.13) may be written in the form

$$\bar{A} \frac{\partial^2 \psi}{\partial r^2} + 2\bar{B} \frac{\partial^2 \psi}{\partial r \partial z} + \bar{C} \frac{\partial^2 \psi}{\partial z^2} \quad \dots \quad (4.14)$$

where $\bar{A} = \gamma N^2$, $\bar{B} = -\gamma B$, $\bar{C} = \gamma I_g^2$, $\gamma = \chi/(\bar{\rho}r)$, N^2 is the *static stability*, I_g^2 is the *generalized inertial stability*, and B is the *baroclinicity*. The last three quantities are given by the expressions:

$$N^2 = -\frac{g}{\chi} \frac{\partial \chi}{\partial z}, \quad I_g^2 = I^2 + \frac{C}{\chi} \frac{\partial \chi}{\partial r}, \quad B = \frac{1}{\chi} \frac{\partial}{\partial z} (C \chi), \quad (4.15)$$

where $I^2 = \xi \zeta_a = \xi(\zeta + f)$ is the inertial stability squared.

The discriminant of the Sawyer-Eliassen equation, Δ , is given by

$$\Delta = \gamma^2 [N^2 I_g^2 - B^2] = (\bar{A} \bar{C} - \bar{B}^2). \quad (4.16)$$

The equation is locally elliptic if $\Delta > 0$, locally hyperbolic if $\Delta < 0$ and locally parabolic if $\Delta = 0$. It can be shown that Δ is proportional to the potential vorticity, PV : i.e.

$$\xi PV = \frac{1}{\bar{\rho}g\chi^3} \Delta. \quad (4.17)$$

so that regions where the Sawyer-Eliassen equation is hyperbolic correspond with regions of negative PV , equivalent to the flow being symmetrically unstable. Regions where $\Delta < 0$ are where the flow is inertially unstable ($I_g^2 < 0$), statically unstable ($N^2 < 0$) or where the baroclinicity, a measure of the vertical shear, is sufficiently large ($\bar{B}^2 > \bar{A} \bar{C}$).

In general, for tropical-cyclone-scale vortices, the coefficients of the highest derivatives in the Sawyer-Eliassen equation are functions of r and z and numerical methods are called for to obtain solutions. Moreover, the complex nature of the coefficients makes it difficult to determine the consequences of any regularization method. For that reason it is helpful to step back and investigate an analogous problem with a simpler partial differential equation.

Notable, for a three dimensional diagnosis, one should use the azimuthal averaged tangential wind field and its corresponding balanced distribution of pressure, density and temperature (which are obtained using the unapproximated method of Smith (2006)) to get the strictly balance solution. Montgomery and Smith (2018) and Montgomery and Persing (2020) discussed details about the limitations of using unbalanced fields.

4.2 The membrane analogy

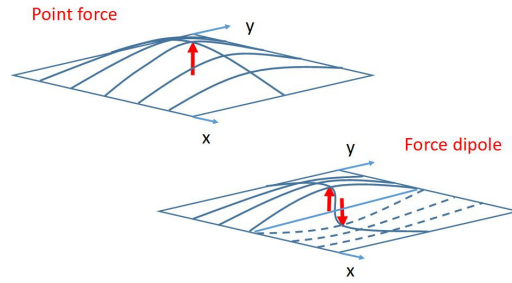


Figure 4.1: Cartoon showing the displacement of a stretched square membrane due to a point force (top left) or a point force dipole (bottom right) at the centre.

One of the simplest physical problems for understanding the behaviour of elliptic second-order partial differential equations is the equilibrium displacement of a stretched membrane subject to a distribution of forces normal to the membrane. Two examples, those of a point force and point force dipole are sketched in Figure 4.1.

In a rectangular coordinate system (x, y) , the membrane displacement $Z(x, y)$ satisfies the Poisson equation:

$$\frac{\partial^2 Z}{\partial x^2} + \frac{\partial^2 Z}{\partial y^2} = -F(x, y), \quad (4.18)$$

where $F(x, y)$ is the imposed force. Here, positive F corresponds to an upward force acting on the membrane. In the case of a square domain $(0 \leq x \leq 1, 0 \leq y \leq 1)$ with zero displacement along the boundary and a point force at the centre $[F(x, y) = \delta(x - \frac{1}{2})\delta(y - \frac{1}{2})]$, one can use one's intuition to see that the solution for the membrane displacement has to be a maximum at the point of forcing with closed contours that are near circular in the vicinity of the forcing and approach a square with smoothed corners near the boundaries. This intuition is confirmed by the numerical solution for a concentrated forcing² shown in Figure 4.2(a). This and other solutions that follow are obtained using the same over-relaxation procedure described by Bui et al. (2009).

For a membrane with the property that it deforms more easily in the x -direction than in the y -direction, the membrane displacement satisfies an equation of the type

$$\frac{\partial^2 Z}{\partial x^2} + \mu^2 \frac{\partial^2 Z}{\partial y^2} = -F(x, y), \quad (4.19)$$

²The forcing is given by the analytic formula $F(x, y) = 10^5 \exp[-\sigma^2]$, where $\sigma = \frac{1}{2}\sqrt{x^2 + y^2}/10^{-2}$.

where μ is a constant smaller than unity. In the case where $\mu = 0.1$, the solution with the forcing function in Figure 4.2(a) is shown in Figure 4.2(b). In this case, the maximum displacement amplitude has increased and the membrane displacement has become confined in the y -direction, barely feeling the boundaries in that direction. Note that a transformation of the y -coordinate in Eq. (4.19) to $Y = y/\mu$ would lead to the same equation as Eq. (4.18), but with Y replacing y and in (x, Y) space the solution would be similar to that in Figure 4.2(a), but the domain would be larger in the Y -direction. It follows that the solution of Eq. (4.19) is simply a stretched version of Eq. (4.18) in the y -direction if $\mu > 1$ and a shrunk version of Eq. (4.18) if $\mu < 1$. The solution in Figure 4.2(c) has a similar but weaker shrunk version than Figure 4.2(b), this feature suggests the magnitude of how much μ departure from 1 can control the degree of deformation, the less difference, the less deformation.

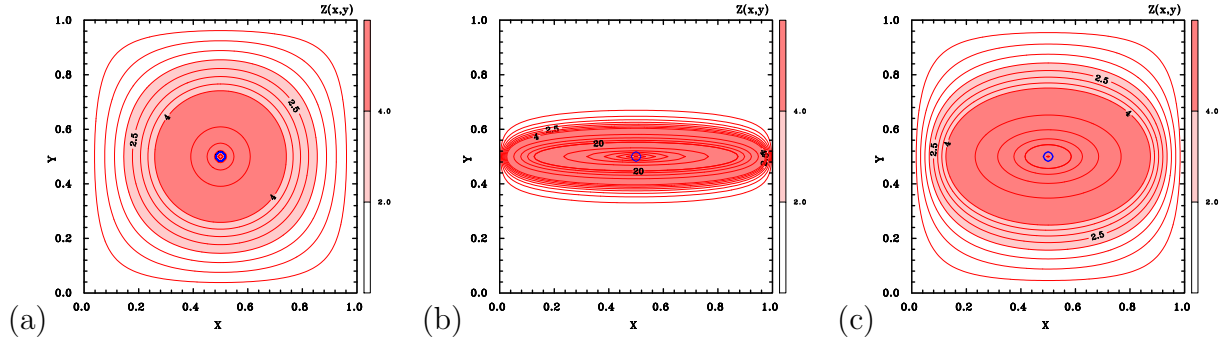


Figure 4.2: Numerical solution of (a) Eq. (4.18), (b) Eq. (4.19) with $\mu = 0.1$ and (c) Eq. (4.19) with $\mu = 0.5$ for the membrane displacement, $Z(x, y)$ (red contours and shading) subject to a concentrated force $F(x, y)$ at the centre (blue contour with the value 10^4). Red contours from 0 to 4 in steps of 0.5, from 4 to 20 in steps of 4 and from 20 to 160 in steps of 20. Shading as shown in the colour bar.

These solutions may be used to understand the consequences of regularization, which would be equivalent to solving Eq. (4.18) over much of the domain, but solving Eq. (4.19) over a limited region with some small value of μ . I shall refer to this region as the “region of regularization” and take it to be a square that includes or excludes the small region of forcing shown in Figure 4.2(a).

Figure 4.3(a) shows the solution when the region of regularization is confined to the dot-dashed square shown. In that region the displacement contours are flattened as in Figure 4.2(b), but as the boundaries are approached the solution is similar to that in Figure 4.2(a). Nevertheless, the amplitude of the maximum displacement is larger than in Figure 4.2(a) as it is in Figure 4.2(b). The effect of flattening of the displacement contours is seen in the difference field shown in Figure 4.3(b).

When the region of regularization is situated away from and to the left of the forcing (Figure 4.4(a)), the maximum displacement is still larger than in Figure 4.2(a), and in fact, the displacement is larger everywhere with the maximum difference located inside the region of regularization (Figure 4.4(b)). When the region of regularization is to the right

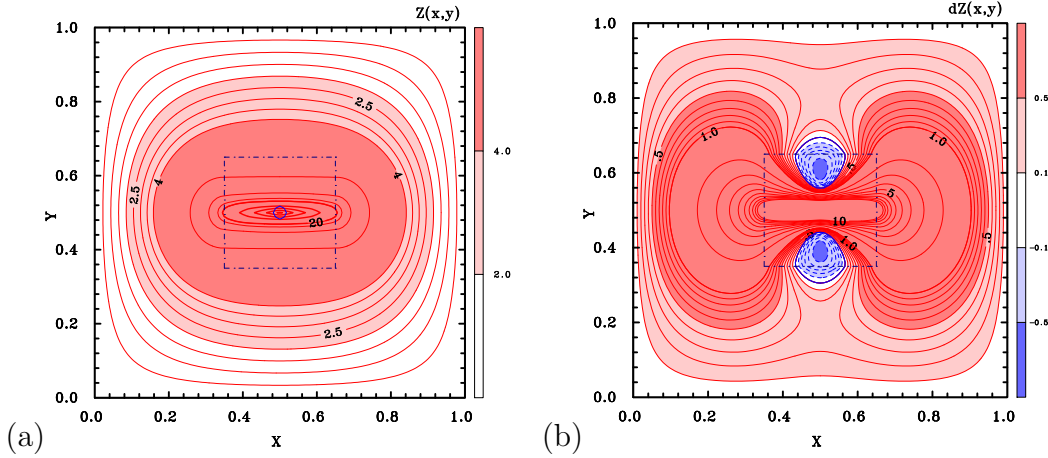


Figure 4.3: Numerical solution of Eq. (4.19) for the membrane displacement, $Z(x, y)$ (left panels, red contours and shading) subject to a concentrated upward force $F(x, y)$ at the centre (blue contour with the value 10^4). In each case, $\mu = 0.1$ inside the dot-dashed square and $\mu = 1.0$ outside this square. The right panels show the difference in displacement, $dZ(x, y)$ (contours and shading) between the particular solution and that shown in Figure 4.2(a). Contour intervals for panels (a): red contours from 0 to 4 in steps of 0.5 and from 4 to 20 in steps of 4. For panels (b): from -1 to 1 in steps of 0.5, from -10 to 10 in steps of 1. Shading as shown in the colour bar.

of the forcing, one may expect a similar pattern of displacement, but with the enhanced values to the right instead of the left of the forcing.

When the region of regularization is situated away from and below the forcing (Figure 4.4(c)), the maximum displacement is smaller than in Figure 4.2(a) and the displacement contours are again flattened out inside the region of regularization. The effect in this location is to reduce the amplitude of the displacement everywhere (Figure 4.4(d)), the maximum difference between the control case being on the border of the domain of regularization closest to the location of forcing. When the region of regularization is above the forcing, one may expect a similar pattern of displacement, but mirror imaged in the x -axis.

When the region of regularization is located on the diagonal to the right of and above the forcing (Figure 4.5a), the flattening of the contours there leads to a dipole pattern of deviation displacement from the control calculation (Figure 4.5b) with a negative deviation in the upper portion of the regularization region and a positive deviation in the lower half, the maximum being located on the lower boundary of the that region.

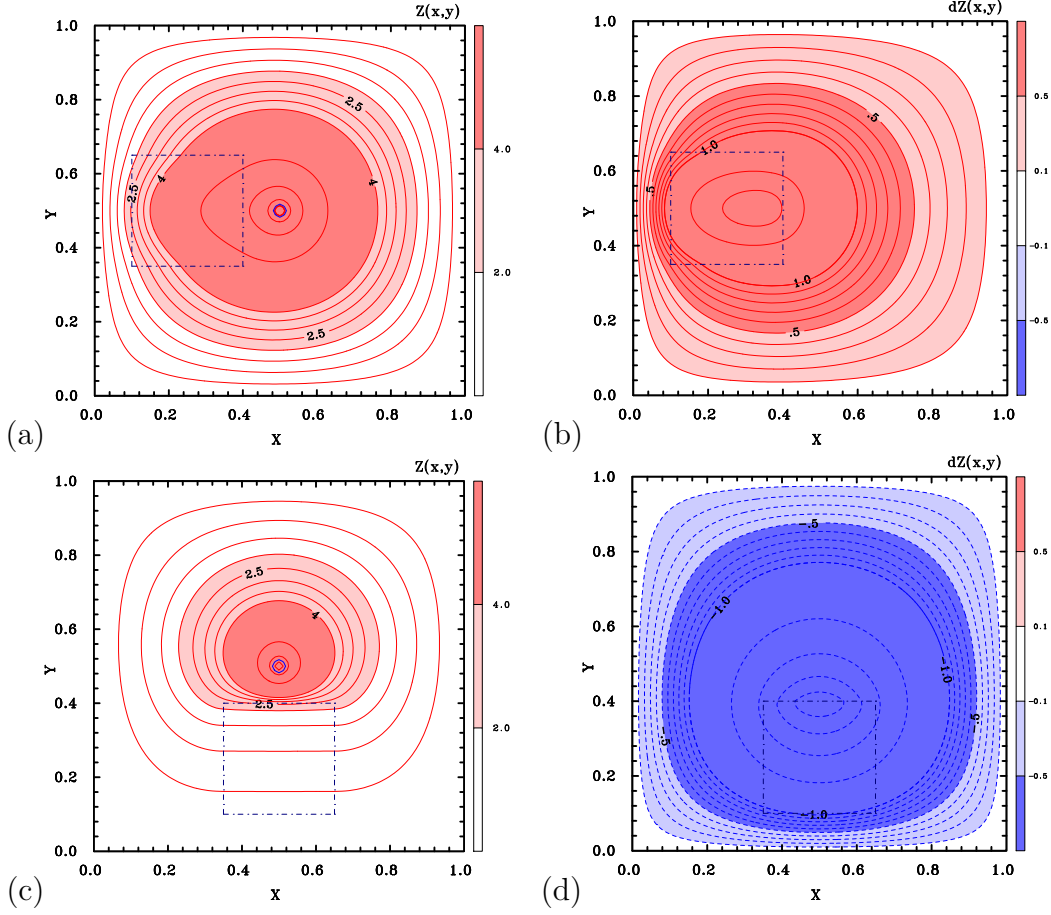


Figure 4.4: Caption as in Figure 4.3, but with the region with $\mu = 0.1$ moved to the left of the forcing (a, b) and above the forcing (c, d).

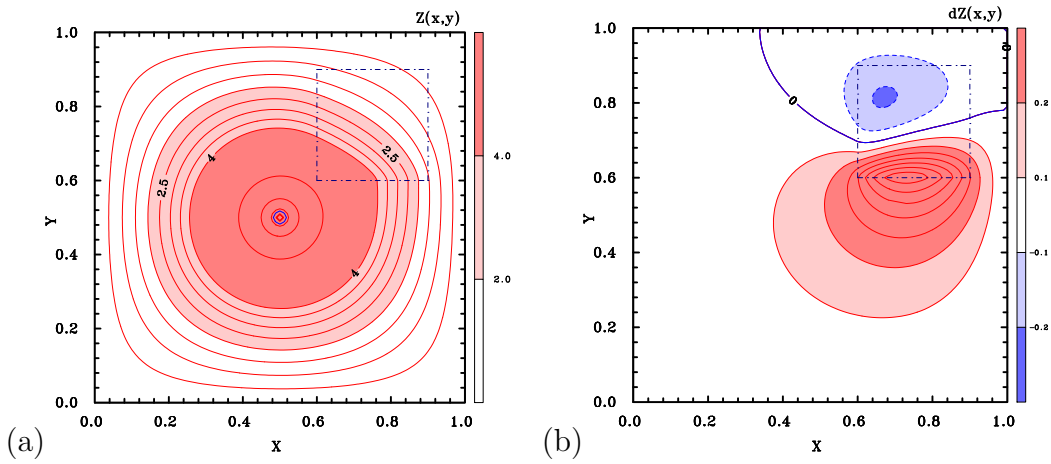


Figure 4.5: Caption as in Figure 4.3, but with the region with $\mu = 0.1$ moved along the diagonal to the right of and above the forcing.

4.3 A more realistic configuration vis-à-vis the atmosphere

In the atmosphere, diabatic heating appears in the Sawyer-Eliassen equation as a dipole of forcing oriented principally in the radial direction. Moreover, a domain that has a large aspect ratio (length to depth) and is open at its lateral boundary is more appropriate in the atmospheric context. Assuming a two-dimensional flow configuration in rectangular coordinates (x, z) , the Sawyer-Eliassen equation for a resting atmosphere would have the form

$$\frac{\partial^2 \psi}{\partial x^2} + \mu^2 \frac{\partial^2 \psi}{\partial z^2} = -F(x, z), \quad (4.20)$$

where again $-F$ represents the structure of the forcing terms in Eq. (4.13). This equation has the same form as Eq. (4.19).

The dipole forcing corresponding to that produced by an idealized line of diabatic heating from deep convection would look something like that in Figure 4.6(a), the dipole being related primarily to the radial gradient of the heating (see Eq. (4.13)). The forcing is located relatively close to the z -axis which is chosen to be a closed boundary ($\psi = 0$) analogous in rectangular geometry to the axis of rotation of an axisymmetric vortex in cylindrical coordinates. The solution for the streamfunction induced by this forcing for³ $\mu = 0.1$ is shown in Figure 4.6(b), assuming that the right boundary of the domain is open and that $\partial\psi/\partial x = 0$ along it. The upper and lower boundaries are taken to be closed with $\psi = 0$ there. The pattern of “lateral velocity”, $u = -\partial\psi/\partial z$, corresponding with the streamfunction is shown in Figure 4.6(c). As expected, and in analogy to the situation in axisymmetric geometry (e.g. Shapiro and Willoughby 1982), the streamfunction shows two cells of circulation with ascent along the axis of the forcing and within the forcing region, itself, and descent elsewhere. Beyond the forcing there is inflow in the lower troposphere and outflow in the upper troposphere and this inflow and outflow pattern extends to the right boundary. Decreasing the value of μ would increase the lateral scale of the outer circulation cell, leading to a larger flow through the right boundary and less recirculation within the domain (not shown).

Figure 4.6(d) shows the analogous solution when the coefficient μ in Eq. (4.20) is reduced to a constant value 0.01 in the rectangle in the “upper troposphere” shown. This configuration is analogous to the procedure of regularizing the Sawyer-Eliassen equation in regions in the upper troposphere where the flow becomes inertially unstable, equivalent in Eq. (4.20) to μ^2 becoming locally negative. As described in Möller and Shapiro (2002), regularization involves effectively setting μ^2 equal to some small positive value in such a region. From the understanding gained in section 4.2, I know that regularization in the rectangular region shown in Figure 4.6(d) will have the effect of flattening out the streamlines in the rectangle. Moreover, the effect is global, but diminishes in magnitude with increasing distance from the region of regularization. As can be seen in the figure, this is precisely what happens.

³In the atmosphere in middle latitudes, a more typical value for μ would be 10^{-4} .

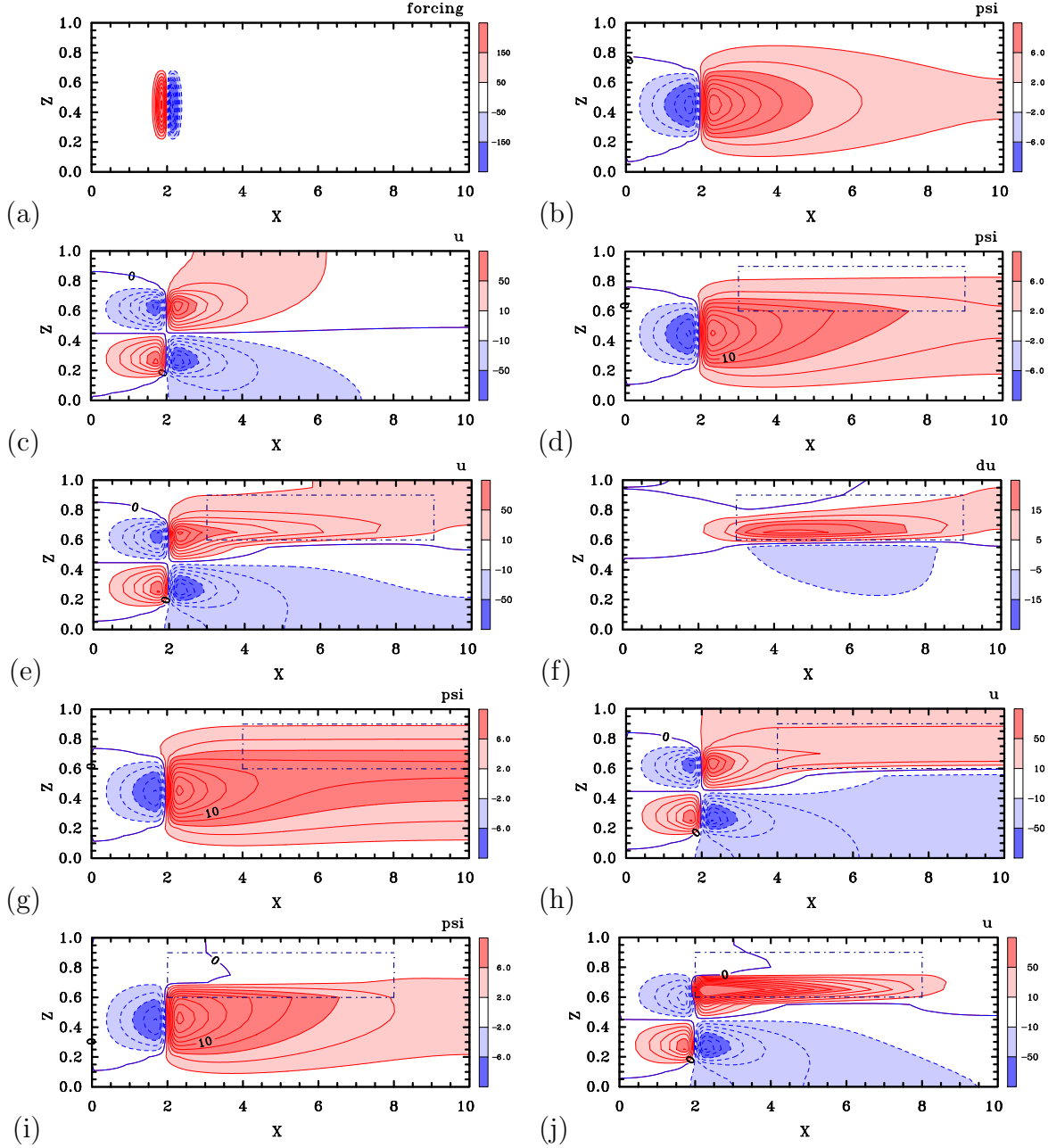


Figure 4.6: (a) Idealized dipole forcing distribution $-F(x, z)$ used to solve Eq. (4.20) with $\mu = 0.1$ for the streamfunction $\psi(x, z)$ (contours and shading) shown in (b). (c) lateral velocity component, $u = -\partial\psi/\partial z$ obtained from $\psi(x, z)$ in (b). (d) the solution for $\psi(x, z)$ when the value of μ is reduced to 0.01 in the rectangular region included by a dot-dash pattern; (e) the corresponding pattern of $u = -\partial\psi/\partial z$; (f) the difference in u , du , between (d) and (b). (g) and (h) are similar to (e) and (f) when the region of $\mu = 0.01$ is displaced to the right; (i) and (j) are similar to (e) and (f) when the region of $\mu = 0.1$ is displaced to the left so that it partially overlaps with the region of forcing. Contour intervals for panel(a): from ± 50 to ± 400 in steps of 50. For (b), (d), (g), (i): from -18 to 18 in steps of 2; for (c), (e), (h), (j): from -100 to 100 in steps of 10. For panel(f): from -5 to 25 in steps of 5. Shading as shown in the colour bar.

Figure 4.6(e) shows the lateral velocity component, $u = -\partial\psi/\partial z$, derived from the streamfunction shown in Figure 4.6(d)⁴. The effect of “regularization” is to destroy the symmetry of the inflow and outflow regions beyond the forcing, leading to stronger outflow in the upper troposphere, albeit concentrated in a shallower layer than the inflow. The difference between the pattern of inflow and outflow between the regularized solution in Figure 4.6(e) and the unregularized solution in Figure 4.6(c) is shown in Figure 4.6(f). Significantly, the outflow is strengthened throughout much of the upper troposphere, not only in the region of regularization, with the maximum increase near the lower boundary of the region of regularization. Elsewhere, the radial flow is decreased, i.e. the inflow has increased, but the maximum decrease occurs a little below the region of regularization.

Figure 4.6(g)-(j) show similar fields to those in Figure 4.6(d)-(e), but where the region of regularization is moved radially outwards (panels (g), (h)) or inwards (panels (i), (j)). When the region of regularization is moved outwards, the radial flow is able to rise higher before the flattening occurs (compare panel (g) with panel (d)), but when the region is moved inwards with the inner boundary at the axis of forcing, the flattening occurs almost immediately as the flow exits the updraught produced by the forcing (compare panel (i) with panel (d)). The consequences for the radial flow are shown in panels (h) and (j), respectively. In the former case, the outflow layer extends over a deeper layer than in panel (e), but the outflow is weaker, whereas, in the latter case, the radial flow is more confined in the vertical, but much stronger than in panel (e).

As will be discussed in section 4.5, the structural changes brought about by regularization shown in Figures 4.6 provide an understanding of possible consequences of regularization in solving the Sawyer-Eliassen equation, itself.

4.4 Methods of regularization

The main purpose of regularization in solving the Sawyer-Eliassen equation is to remove any regions of symmetric instability ($\Delta < 0$). This removal can be achieved by replacing the corresponding negative coefficients (N^2 or I_g^2) with small positive values and/or by suitably decreasing the coefficient B . Alternatively, the removal can be achieved by sufficiently *increasing* the magnitude of the inertial stability, static stability, or both (a procedure adopted by Möller and Shapiro 2002).

Any such scheme is necessarily *ad hoc* and different authors have used different methods in detail. For example, Bui et al. (2009); Smith et al. (2018a) and Smith and Wang (2018), calculate the minimum value of I_g^2 in the region where $\Delta < 0$, say $I_{g\ min}^2$, then remove the negative values of I_g^2 by adding $|1.001I_{g\ min}^2|$. Further, at points where $N^2 < 0$, which typically do not coincide with those where $I_g^2 < 0$, N^2 is set equal to 10^{-8} s^{-2} . Finally, if Δ is still less than or equal to zero, which, when $|I_g^2|$ is made small and positive is frequently the case, \bar{B}^2 is replaced with $\frac{1}{2}\bar{A}\bar{C}$ at the grid point in question.

⁴Since the focus of this section is in changes of pattern, I have refrained from ascribing actual units to quantities in Eq. (4.20).

Heng and Wang (2016) do essentially the same as Bui et al. (2009), setting $\zeta_a = 1 \times 10^{-6} \text{ s}^{-1}$ at points where $I_g^2 < 0$, but they do not say what they do if Δ remains negative. In contrast, Heng et al. (2017) set $\zeta_a = 0.01f$ at points where $\zeta_a < 0.01f$ and if there are remaining points where $\Delta < 0$, they progressively reduce the term \bar{B} by a factor 0.8 until $\Delta > 0$.

A different procedure is adopted by Möller and Shapiro (2002). In regions where $\Delta < 0$ they increased the value of ζ (and thereby ζ_a) so that, effectively⁵, Δ has some small positive threshold value. No other quantities appearing in the Sawyer-Eliassen equation coefficients are altered so that, in particular, the new value of ζ is not consistent with the local structure of \bar{v} . Of course, this is a property of the other schemes as well. Apparently, in the vortex examined by Möller and Shapiro, regions of negative Δ were due largely to the occurrence of inertial stability, $I_g^2 < 0$.

The hope in all these studies has been that, whatever procedure is used, regularization will lead to a useful balance solution, at least in regions remote from those where regularization is needed, but there are some subtle differences between the procedures that have consequences for the diagnosed structure of the balance solution.

As noted above, the Möller and Shapiro procedure differs from the others in that, at points where $\Delta < 0$, I_g^2 is *increased* in magnitude, even if the point with $\Delta < 0$ is a consequence of large vertical shear and not necessarily because the flow is inertially unstable ($I_g^2 < 0$). In contrast, in the other schemes, points with inertial instability are removed first by setting I_g^2 to be a *small* positive number, typically *smaller* in magnitude than its original magnitude. The analysis in section 4.2 points to a different local response to forcing depending on which regularization procedure is adopted and therefore to a different structure of the balance solution in and near the region where $\Delta < 0$.

4.5 An idealized 3D numerical simulation of a tropical cyclone

The next step is to apply the insights gained above to assess the applicability of balance theory in analyzing the secondary circulation of an idealized three-dimensional numerical simulation of tropical cyclone evolution on an f -plane. The simulation is similar to the one described by Kilroy et al. (2016), but uses the CM1 model (Bryan and Fritsch 2002) with a horizontal grid spacing of 1 km and a vertical grid spacing of 100 m. These data were kindly provided by Dr. Gerard Kilroy.

Figure 4.7(a) shows the azimuthally-averaged and 3 h time-averaged radial and tangential velocity components from the foregoing simulation at 32 h. At this time the vortex was undergoing a period of rapid intensification. The main features of the simulation are similar to those described in many previous studies (see Montgomery and Smith 2017 and references). In particular, there is a shallow layer of strong inflow near the surface and one

⁵Actually, they use the potential vorticity rather than Δ , but these quantities are proportional to one another

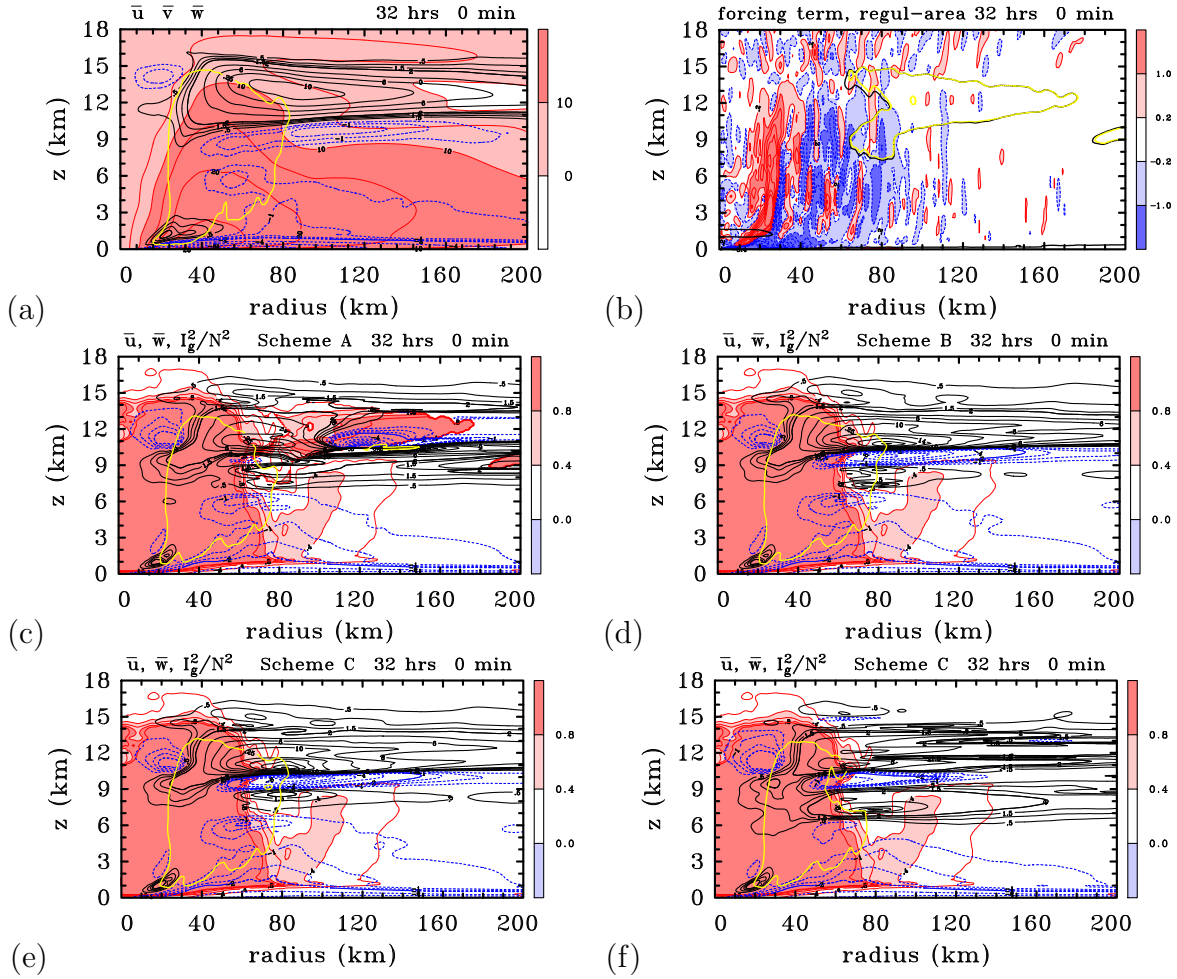


Figure 4.7: (a),(b) Radius-height cross-sections of selected three hour time-averaged and azimuthally-averaged fields from the numerical model simulation at 32 h: (a) tangential velocity component \bar{v} (red contours and shaded, Unit: m s^{-1}), radial velocity component \bar{u} (blue dashed contours for negative values and black solid contours for positive values, Unit: m s^{-1}) and vertical velocity component \bar{w} (yellow contour with a value 0.25 m s^{-1}); (b) Forcing term for the Sawyer-Eliassen equation (the right-hand-side of Eq. (4.13)), (contours and shading, contour values every 0.8 units from ± 0.2 units to ± 5 units: 1 unit $= 1 \times 10^{-11} \text{ K m}^{-1} \text{ s}^{-1}$). Shown also are the zero contours of the discriminant (black solid line or dotted yellow contours: the latter enclose regions of inertial instability). (c), (d), (e) and (f) show fields of the ratio I_g^2/N^2 in the Sawyer-Eliassen equation (red contours and shaded) and the radial velocity component \bar{u} (blue dashed contours for negative values and solid black contours for positive values, Unit: m s^{-1}) and vertical velocity component \bar{w} (yellow contour with a value 0.25 m s^{-1}) from the solution of this equation using the three regularization schemes: (c) Scheme A, (d) Scheme B, (e) Scheme C, (f) Scheme C with the forcing set to zero inside the upper-level region of non-positive discriminant. Contour intervals: for \bar{v} , every 5 m s^{-1} from 0 to 30 m s^{-1} ; for \bar{u} , every 0.5 m s^{-1} from ± 0.5 to $\pm 2 \text{ m s}^{-1}$ and every 2 m s^{-1} from ± 2 to $\pm 20 \text{ m s}^{-1}$. For I_g^2/N^2 , every 0.2 units from 0.2 to 1 units, 1 unit $= 1 \times 10^{-3}$. Shading as shown in the colour bar.

of strong outflow centred at about 12 km. There is a shallow region of marked outflow just above the boundary layer, where the inflow terminates and ascends into the developing eyewall updraught. This updraught is indicated by the contour of vertical velocity equal to 0.25 m s^{-1} . There is a region of weaker inflow in the lower troposphere, with a shallow layer of weak inflow just below the main outflow layer. The maximum tangential wind speed occurs at a height 600 m and radius of 38 km, within the layer of strong inflow.

The mean tangential wind field in Figure 4.7(a) is used to obtain balanced density and potential temperature fields using the method described by Smith (2006). In turn, these fields are used to evaluate the coefficients on the left-hand-side of the Sawyer-Eliassen equation. The forcing terms on the right-hand-side of the Sawyer-Eliassen equation arising from diabatic heating and friction are diagnosed also from the time- and azimuthally-averaged model output. The structure of the combined forcing is shown in Figure 4.7(b). The main region of positive forcing is near the inner edge of the main region of ascent, the region within the yellow contour in Figure 4.7(a). At larger radii, mostly beyond a radius of 28 km and inside a radius of about 90 km, there are narrow strips of negative forcing, punctuated by even narrower strips of positive forcing. There is a shallow region of negative forcing below a height of about 1.5 km and inside a radius of 50 km. This feature is associated with the inner-core boundary layer.

Figure 4.7(b) shows also the regions where the discriminant of the Sawyer-Eliassen equation, Δ , is negative. The main area of negative Δ is located in the mid to upper troposphere between radii of approximately 70 km to 180 km, much of it overlapping with the main outflow layer. This region, together with a much smaller region near the outer boundary between about 9 and 10 km in height, is associated with the generalized inertial stability, I_g^2 , being negative. A shallow finger of negative Δ located just above 2 km height and extending to nearly 30 km in radius is associated with static instability $N^2 < 0$ and a shallow (less than 400 m deep) surface based layer of negative Δ is associated with large vertical shear where $\bar{B}^2 > \bar{A}\bar{C}$. All of these regions require regularization in order to solve the Sawyer-Eliassen equation.

Because the region of static instability is so small, the flow therein appears to be little influenced by the regularization. For this reason I do not examine other methods to regularize the Sawyer-Eliassen equation in such regions. More details about the regularization of the equation in regions where $\bar{B}^2 > \bar{A}\bar{C}$ are discussed in Section 4.6.

4.5.1 Two regularization schemes

Figures 4.7(c) and 4.7(d) show the balanced radial flow obtained by solving the Sawyer-Eliassen equation with the forcing terms shown in Figure 4.7(b) using two regularization schemes. They show also fields of the ratio I_g^2/N^2 , which is the same as the ratio \bar{C}/\bar{A} in Eq. (4.14) and is analogous to the quantity μ^2 in Eq. (4.20). In the scheme in Figure 4.7(c), which I refer to as Scheme A, regions of negative $I_g^2(r, z)$ are removed by adding $|1.001I_{g \min}^2|$. In Figure 4.7(d), a new procedure is adopted in which negative values of $I_g^2(r, z)$ are removed by adding the local value $|1.001I_g^2(r, z)|$. This procedure, which I refer to as Scheme B, has the advantage of avoiding artificially sharp gradients of I_g^2 at

the boundary of the region where $\Delta < 0$. Even so, the reduction in the magnitude of I_g^2 generally requires a reduction in the magnitude of B to keep $\Delta > 0$. In this section, \bar{B}^2 is replaced with $0.99\bar{A}\bar{C}$ at each grid point where Δ remains negative after modifying I_g^2 . Other possibilities are explored in section 4.6.

While both schemes capture the broad features of the secondary overturning circulation, the flow structure in the upper troposphere shows considerable differences, principally in the region of regularization and regions adjacent to it. As shown in Section 4.2, a small inertial stability as in the modified scheme provides for an enhanced response of the radial velocity component to the forcing, while the larger inertial stability in the original scheme acts to inhibit the radial flow. Figure 4.6(f) provides a clue to understanding this behaviour. It shows that there is enhanced radial outflow flow just inside the region of reduced inertial instability and enhanced radial inflow or reduced outflow below that region. Conversely, if the inertial stability in the region of regularization is increased in magnitude beyond that of the surrounding values, there is enhanced radial inflow or reduced outflow above the boundary of regularization (not shown).

The new regularization scheme appears to reproduce the flow structure in the numerical model somewhat better than the original scheme, although the layer of inflow just below the main outflow layer is much too strong. The maximum outflow in the upper troposphere in the balance solution is 20.2 m s^{-1} compared with 11.2 m s^{-1} in the numerical model, while the maximum upper-level inflow is 10.7 m s^{-1} compared with only 1.8 m s^{-1} in the numerical model. Thus, even with the new procedure for replacing negative values of $I_g^2(r, z)$, the regularized balance solution does a relatively poor job in capturing the outflow and inflow strengths in the numerical model.

4.5.2 The Möller and Shapiro scheme

An alternative regularization scheme, which I refer to as Scheme C, is to set $\bar{C} = \bar{B}^2/0.99\bar{A}$, whereupon it is not necessary to change \bar{B} . This scheme was suggested by Möller and Shapiro (2002). The results of this scheme are shown in Figure 4.7(e). While the radial flow structure in this figure is closer to that in Figure 4.7(d) than that in Figure 4.7(c), it is no improvement in relation to the numerical solution in Figure 4.7(a). In this case, the maximum outflow in the upper troposphere is 20.2 m s^{-1} , the same as before, but the maximum upper-level inflow is slightly larger, 11.2 m s^{-1} instead of 10.7 m s^{-1} , making the agreement with the numerical solution slightly worse.

4.5.3 The issue of forcing overlapping with regions in which $\Delta < 0$

As indicated in Figure 4.7(b), there is considerable overlap between the total forcing distribution due to heating and friction and the primary region where the flow is inertially unstable. Figure 4.3(a) shows that this is a situation where the response to the forcing is particularly large in amplitude. This finding may explain why the magnitude of upper-tropospheric inflow and outflow shown in Figure 4.7(e) is overestimated. To examine this possibility, I show in Figure 4.7(f) the solution to the Sawyer-Eliassen equation analogous

to that in Figure 4.7(e), but with the forcing function set equal to zero in the upper level region of non-positive discriminant. While the maximum outflow and maximum inflow are indeed reduced in comparison with those in Figure 4.7(e), the second layer of outflow centred at a level of about 8 km has strengthened considerably and this layer is not even present in the numerical calculation in Figure 4.7(a). This feature is presumably a result of the artificially large vertical gradient of the forcing on the boundary of the main regularization region, which is introduced by setting the forcing abruptly to zero inside the region of regularization.

The inability of the Sawyer-Eliassen calculation to capture quantitatively the upper-level structure seen in the numerical calculation could be the fact that the flow in the numerical model is nowhere near axisymmetric at 32 h (not shown). An alternative, but not necessarily mutually exclusive explanation would be that the inability is simply a consequence of regularizing the Sawyer-Eliassen equation. Based on the understanding gained in Section 4.3, this would seem to be the most likely scenario, since the flow in the lower half of the troposphere is somewhat better captured by the balance calculation, except in a shallow layer near the surface. The flow in the near-surface layer, which is one that overlaps also with negative discriminant of the Sawyer-Eliassen equation is examined in the next section.

Despite the large differences in the structure of inflow and outflow in the middle and upper troposphere in Figure 4.7(c)-(e) as a result of the different regularization schemes, there is little difference in the lower troposphere and there are only small differences in Figure 4.7(f), in which the forcing is suppressed in the region requiring regularization. I conclude that the boundary layer inflow is at most weakly influenced by the regularization of regions of inertial instability in the upper troposphere. This is counter to the claim by Heng et al. (2017) that “... the boundary layer inflow in the balanced response is very sensitive to the adjustment to inertial stability in the upper troposphere ...”. A more detailed examination of boundary layer structure is shown in the next section.

4.6 Regularization in regions of large vertical shear

4.6.1 Exploitation of the membrane analogy

The effect of vertical shear enters the Sawyer-Eliassen equation through the second-order mixed derivative term. In the membrane analogy, one would add the $\beta \partial^2 Z / \partial x \partial y$ term to the left-hand-side of Eq. (4.21),

$$\frac{\partial^2 Z}{\partial x^2} + \beta \frac{\partial^2 Z}{\partial x \partial y} + \frac{\partial^2 Z}{\partial y^2} = -F(x, y), \quad (4.21)$$

Figure 4.8 shows solutions of Eq. (4.21) with different values β . In comparison with the solution in Figure 4.2(a), which is for the case $\beta = 0$, the displacements in Figures 4.8(a) and (b) are stretched along the diagonal from low left to up right. The larger the coefficient β , the larger the degree of stretching. Figure 4.8(c) shows the solution when

$\beta = 1.9$ in the dot-dashed square and $\beta = 0.5$ outside the square. In that square the displacement has a larger degree of stretching, but as the boundaries are approached the solution is similar to that in Figure 4.8(b). Figure 4.8(d) shows the case for $\beta = -1$. In this case the stretching is rotated from up left to low right.

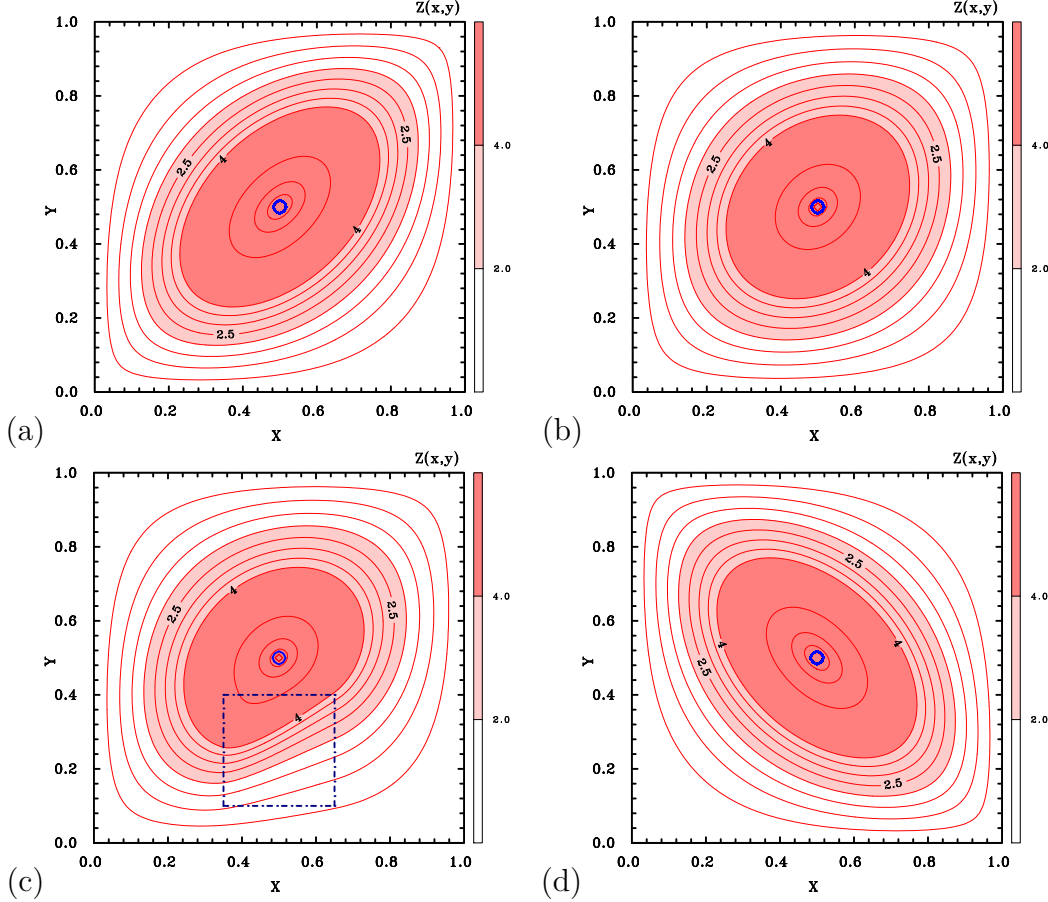


Figure 4.8: Numerical solution of Eq. (4.21) for the membrane displacement, $Z(x,y)$ (red contours and shading) subject to a concentrated force $F(x,y)$ at the centre (blue contour with the value 10^4), where (a) $\beta = 1$, (b) $\beta = 0.5$, (c) $\beta = 1.9$ inside the dot-dashed square with $\beta = 0.5$ everywhere else and (d) $\beta = -1$. Red contours from 0 to 4 in steps of 0.5, from 4 to 20 in steps of 4 and from 20 to 160 in steps of 20. Shading as shown in the colour bar.

4.6.2 A more realistic configuration

In regions of large vertical shear, Δ may become negative on account of \bar{B}^2 exceeding $\bar{A}\bar{C}$. Typically, such regions occur in a shallow surface-based layer within the friction layer, itself. As explained in section 4.4, one method for removing the negative discriminant is to set $\bar{B}^2 = \frac{1}{2}\bar{A}\bar{C}$ or, perhaps preferably $\bar{B}^2 = 0.99\bar{A}\bar{C}$ to make Δ positive, but closer to zero.

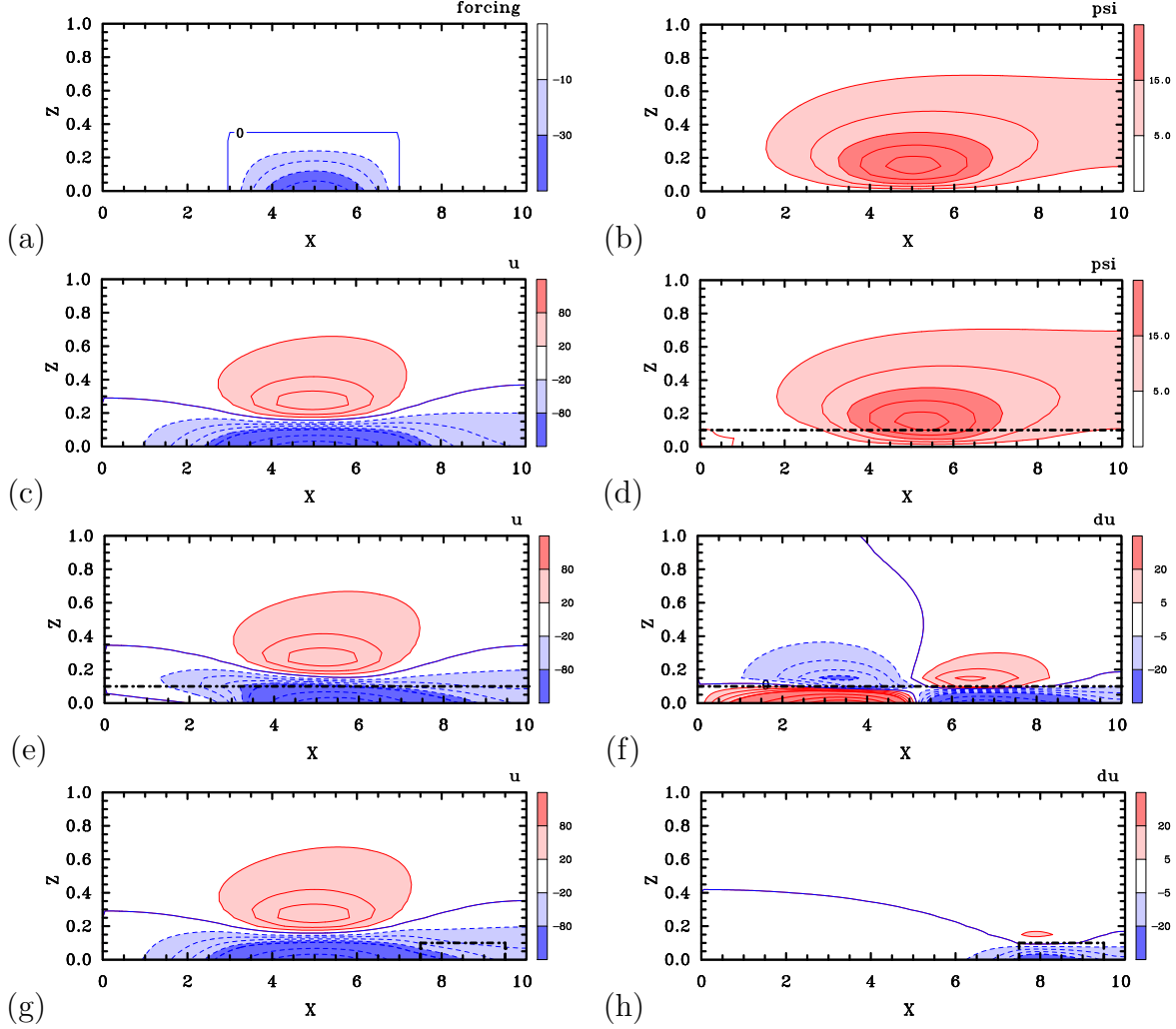


Figure 4.9: (a) Idealized forcing distribution $-F(x, z)$ used to solve Eq. (4.20) with $\mu = 0.1$ for the streamfunction $\psi(x, z)$ (contours and shading) shown in (b). (c) lateral velocity component, $u = -\partial\psi/\partial z$ obtained from $\psi(x, z)$ in (b). (d) the solution for $\psi(x, z)$ when the value of \bar{B} is set to $-\sqrt{0.99}\mu$ in the rectangular region included by a dot-dash pattern; (e) the corresponding pattern of $u = -\partial\psi/\partial z$; (f) the difference in u , du , between (e) and (c). (g) and (h) are similar to (e) and (f) when the region of $B = -\sqrt{0.99}\mu$ is smaller and to the right. Contour intervals for panel(a): from -40 to -10 in steps of 10. For (b), (d): from 5 to 15 in steps of 5 and from 15 to 45 in steps of 15; For (c), (e),(g): from -100 up to 100 in steps of 20 and from -500 to 500 in steps of 100. For (f): from -20 to 20 in steps of 5 and from -100 to 100 in steps of 20. Shading as shown in the colour bar.

The consequences of redefining \bar{B} are illustrated in three idealized calculations shown in Figure 4.9. These calculations involve solutions of Eq. (4.20) with $\mu^2 = 0.01$, as in Figure 4.6, and with an idealized surface-based layer of forcing, $-F(x, z)$ shown in Figure 4.9(a). This forcing distribution is analogous to that involving the vertical gradient of \dot{V} in Eq. (4.13). Figure 4.9(b) shows the streamfunction $\psi(x, z)$ induced by the forcing distribution shown in panel (a).

Figure 4.9(c) shows the radial velocity derived from the streamfunction shown in panel (b), highlighting the fact that there is inflow in the region of forcing and outflow above it, but because of the implied strong vertical stability in the value chosen for μ , the maximum outflow occurs at low levels, just above the layer of forcing.

Figure 4.9(d) shows the streamfunction for a similar calculation to that in panel (b), but when a term $2\bar{B}\partial^2\psi/\partial x\partial z$ is added to the left-hand-side of Eq. (4.19) in a layer that has half the depth of the layer of forcing. The constant \bar{B} is chosen to be equivalent to setting $\bar{B}^2 = 0.99\bar{A}\bar{C}$ in the Sawyer-Eliassen equation in cases where the vertical shear is large and would otherwise make the discriminant Δ negative. Moreover, when taking the square root, the sign of \bar{B} should be preserved as it was before regularization.

Comparison of Figure 4.9(d) with Figure 4.9(b) shows that the effect on the streamfunction from the inclusion of the term involving \bar{B} in Eq. (4.19) is minimal, producing a slight clockwise rotation of the streamlines in the region of nonzero \bar{B} . Such rotation was explained in the classic paper by Shapiro and Willoughby (1982): see especially Figure 1 and related discussion. The effect is mainly discernible in the slight elevation of the streamlines in the inner region ($x < 5$) and in the slight depression of the streamlines in the outer region ($x > 5$).

Figure 4.9(e) shows the lateral component of flow in this case, which should be compared with Figure 4.9(c). In essence, the “regularization” has reduced both the surface-based inflow and the outflow above it on the inner side of the forcing and has enhanced both the inflow and outflow on the outer side of the forcing. These effects are highlighted in panel (f), which shows the difference between the lateral flow in panels (e) and (c). A comparison of Figures 4.9(g) and 4.9(h) indicate that the “inflow” on the right side of the regularization region has been strengthened, which is the situation in the simulation as discussed in the next subsection.

4.6.3 Comparison between the numerical simulation and the balance calculation at low levels

Figure 4.10 shows similar fields to those in Figure 4.7, but focusing on the low-level flow structure in the numerical model simulation and in the calculation of the balanced response to the total forcing due to heating and friction. Figure 4.10(a) shows the flow structure of Figure 4.7(a) in the lowest 3 km, while Figure 4.10(b) shows the structure of the forcing (Figure 4.7(b)) in this region together with the regions where the Sawyer-Eliassen equation requires regularization. The region where large vertical shear leads to a need for regularization is rather shallow, less than 400 m deep, extending from a radius near 30 km. Based

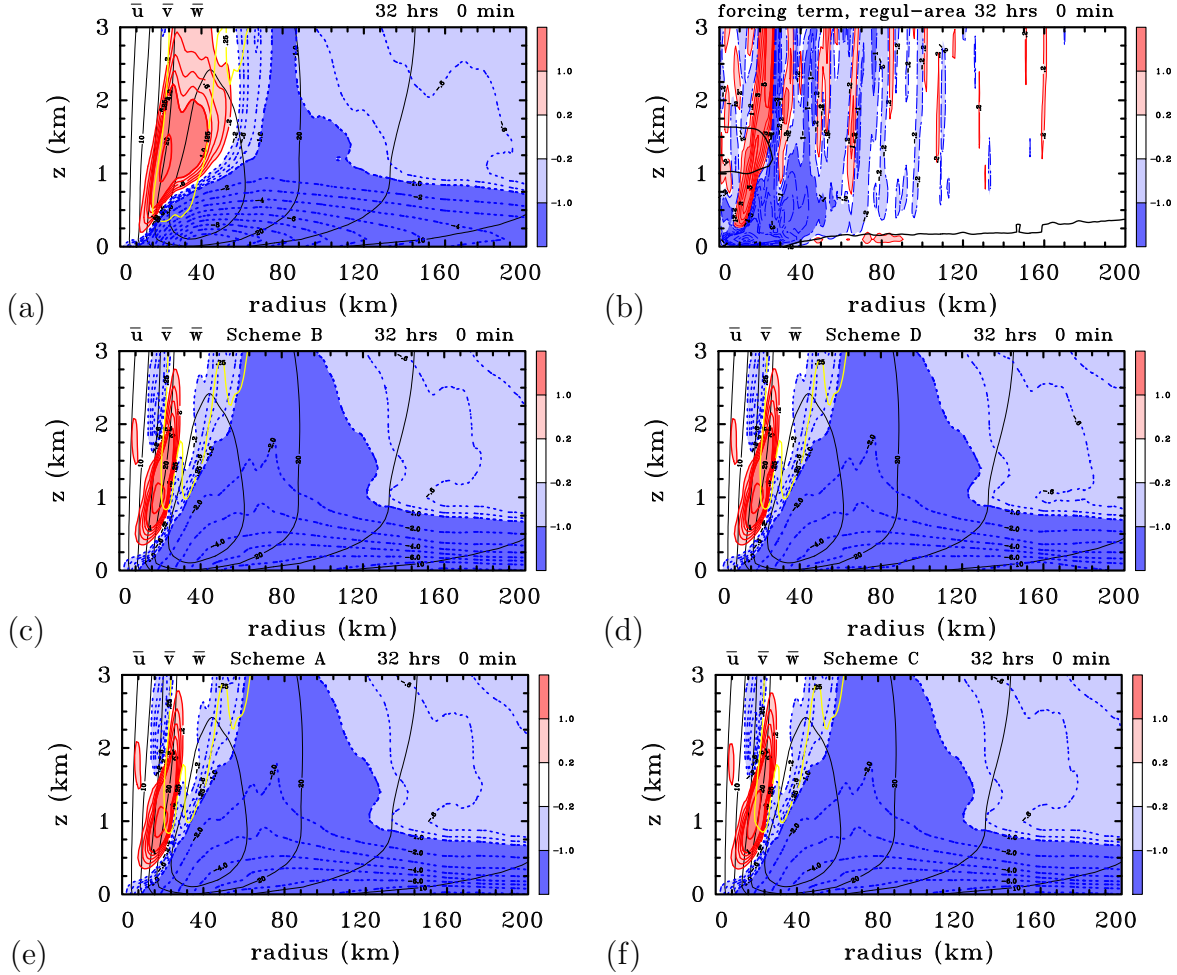


Figure 4.10: (a),(b) Radius-height cross-sections of three hour time-averaged and azimuthally-averaged fields from the numerical model simulation at 32 h from surface to 3 km: (a) tangential velocity component \bar{v} (black contours, Unit: m s⁻¹), radial velocity component \bar{u} (blue dashed contours for negative values and red solid contours for positive values, Unit: m s⁻¹) and vertical velocity component \bar{w} (yellow contour with a value 0.25 m s⁻¹); (b) Forcing term (the right-hand-side of Eq. (4.13)) derived from the model (contours and shading, contour values every 0.8 units from ± 0.2 units to ± 5 units. 1 unit = $1 \times 10^{-11} \text{K m}^{-1} \text{s}^{-1}$). Shown also are the zero contours of the discriminant (black solid line). (c), (d), (e) and (f) show tangential velocity component \bar{v} (black contours, Unit: m s⁻¹), the radial velocity component \bar{u} (blue dashed contours for negative values and solid black contours for positive values, Unit: m s⁻¹) and vertical velocity component \bar{w} (yellow contour with a value 0.25 m s⁻¹) from the solution of this equation using the four regularization schemes; (c) Scheme B, (d) Scheme D, (e) Scheme A, (f) Scheme C. Contour intervals are: for \bar{v} , every 5 m s⁻¹ from 0 to 30 m s⁻¹; for \bar{u} : every 0.2 m s⁻¹ from ± 0.2 to ± 1 m s⁻¹ and every 1 m s⁻¹ from ± 1 to ± 10 m s⁻¹. Shading as shown in the colour bar.

on the idealized calculations in Figure 4.9, the effect of the regularization required in this layer would be expected to be minimal and unlikely to account for the difference in low-level structure between the numerical solution in Figure 4.10(a) and the balance solution shown in Figure 4.10(c). (The latter figure shows just the lower 3 km of Figure 4.7(d)).

While the maximum inflow in the numerical solution is 11 m s^{-1} , that in the balance calculation is just about 8.3 m s^{-1} . Moreover, the radial location of the maximum inflow occurs at a much smaller radius (41 km) compared with the radius in the balance calculation (174 km). One possible reason is that the inflow inside the regularization area to the right side of the momentum forcing maximum has been enhanced, as in Figure 4.9(e). However, the analysis of the previous subsection suggests that this effect would not be large enough to explain the large difference between Figure 4.10(c) and Figure 4.10(a).

Figure 4.10(d) shows a similar regularization scheme to scheme A, but in regions of large baroclinicity, \bar{B}^2 is replaced with $0.5\bar{A}\bar{C}$. I refer to this as Scheme D. This is the scheme used by Bui et al. (2009); Smith et al. (2018a) and Smith and Wang (2018). There are only small differences from the fields shown in panel (c) and these are confined to the vicinity of the regularization region. From this result it would appear that the flow in regions of large vertical shear that are common in the lower part of the boundary layer is less sensitive to the regularization procedure than that in regions of inertial instability.

In support of the conclusion at the end of subsection 4.5.3 that the boundary layer inflow is at most weakly influenced by the regularization of regions of inertial instability in the upper troposphere, Figure 4.10(e) and (f) show just the lower 3 km of Figure 4.7(c) and (e). The boundary layer structures in Figure 4.7(c), (d) and (e) are almost identical and they even have the same magnitude of maximum inflow (8.3 m s^{-1}) at the same radius (174 km).

Clearly, the balance solution poorly captures the boundary layer inflow in the numerical calculation, a finding consistent with the study of Bui et al. (2009) and the more recent calculations of Montgomery and Persing (2020). The finding is clearly at odds with one of Heng et al. (2017) who claim that “balanced dynamics can well capture the secondary circulation in the full-physics model simulation *even in the inner-core region in the boundary layer*”, but is supported by a scaling analysis of the boundary layer equations, which shows that the unbalanced (nonlinear) terms are important in the inner-core region of a tropical cyclone (Vogl and Smith 2009). It is supported also by the finding of Vogl and Smith (2009) that even a linear (but unbalanced) approximation to the boundary layer equations is a poor representation of the inner-core boundary layer of a tropical cyclone.

4.7 Discussion

A framework has been developed for exploring the consequences of regularizing the Sawyer-Eliassen equation to diagnose the streamfunction for the axisymmetric secondary circulation of a tropical cyclone subject to a given distribution of diabatic forcing and tangential frictional stress. Regularization amounts to adjusting the coefficients of the equation in regions where the discriminant is negative to ensure that the equation is globally elliptic.

The possible consequences of regularization have been explored using the analog behaviour of a stretched membrane subject to a particular force distribution.

Regularization is required in three regions: (1) regions where the flow is inertially unstable; (2) regions where it is statically unstable; and (3) regions where the baroclinicity is large. Regions of large baroclinicity are typically ones of large vertical shear. In numerical models of tropical cyclones, regions of azimuthally-averaged inertial instability are generally the most extensive, while regions of static instability are typically small in areal extent. Regions where the azimuthally-averaged baroclinicity is large are typically confined to the lower part of the frictional boundary layer, where the vertical shear is large. However, setting the inertial stability to be small and positive in regions of inertial instability generally requires the baroclinicity to be reduced in magnitude as well to keep the discriminant of the Sawyer-Eliassen equation positive. Possible improvements in the procedure for regularizing in cases (1) and (3) were suggested.

A comparison of the azimuthally-averaged radial flow from a three-dimensional numerical simulation of a tropical cyclone with those from an axisymmetric balance calculation of the Sawyer-Eliassen equation forced by diabatic and frictional terms from the numerical simulation was presented. Important findings from this comparison are:

- (1) The largest uncertainty in the integrity of the balance solutions results from the regularization in regions of inertial instability, especially when the diagnosed forcing overlaps with such regions. In the example shown, where there is some overlap of this type, the diagnosed balanced flow is sensitive to the particular procedure for regularization and none of the schemes produced a flow that was structurally and quantitatively close to that obtained from the numerical solution.
- (2) Regularization in regions of large vertical shear that typically occur in the lower part of the boundary layer is less problematic, even though such regions are ones in which there is forcing. The reason is that a modification of the coefficient B in the Sawyer-Eliassen equation leads to a rotation of the streamfunction response, but the degree of rotation is constrained by the proximity of the lower boundary.
- (3) On account of (2), the large difference found between the low-level inflow in the azimuthally-averaged numerical solution and that in the axisymmetric balance solution is further indication that *balance dynamics is unable to adequately capture the flow in the boundary layer*, contrary to recent claims.

While balance ideas have played a central role in the development of a theoretical framework for understanding tropical cyclone dynamics, the application of such ideas to diagnose the results of numerical simulations almost always requires that the Sawyer-Eliassen equation be regularized. Regularization is intrinsically an *ad hoc* procedure and some methods may be better than others. Exploitation of the membrane analogy as outlined herein would seem to offer a useful framework for assessing the integrity of such procedures and their possible limitations. The analysis suggests, however, that regularization introduces uncertainties in the integrity of balance solutions to a degree that much caution is called for in

the use of such solutions for “explaining” tropical cyclone structure, especially within and near the regions which have been regularized.

Chapter 5

Balance explanation for upper inflows and its issues

Long ago, Willoughby (1979) presented a scale analysis of the equations of motion for a tropical cyclone and showed that, with the exception of the frictional boundary layer and possibly parts of the upper-level outflow, the flow in a tropical cyclone is in approximate gradient wind balance and hydrostatic balance. With these balance assumptions one can then develop a prognostic theory for axisymmetric tropical cyclone evolution (e.g. Ooyama 1969; Sundqvist 1970a,b; Emanuel 1989; Schubert and Alworth 1982; Möller and Smith 1994; Smith et al. 2018a; Smith and Wang 2018).

In a subsequent paper, drawing on a previous result of Eliassen (1951), Shapiro and Willoughby (1982) noted that the response of the secondary circulation to a positive point source of tangential momentum is radially-outwards through the source, following a nearly horizontal isentropic surface, and radially-inwards above and below the source (see their Figure 1). A cyclonic source of azimuthal-mean tangential momentum had been thought of as a mechanism for enhancing the upper-level outflow in a tropical cyclone (Challa and Pfeffer 1980 and refs; Molinari and Vollaro 1990 and refs; Montgomery and Farrell 1993), which would act as a catalyst for inducing the intensification process. The origin of such a source was attributed to “eddy forcing” resulting from flow asymmetries and/or potential vorticity anomalies in the upper-level outflow region. It follows that the radially-inward flow above and below such a tangential momentum source might provide an alternative explanation for the existence of upper-tropospheric inflow layers as studied here. Such a possibility needs exploring. Based on the discussion in the last chapter, the explanation of a balance theory view seems to be problematic.

On the other hand, Most previous solutions of the Sawyer-Eliassen equation have been obtained using the successive over-relaxation (SOR) method with a coarsened resolution including those in the aforementioned papers. Recent work by Montgomery and Persing (2020) raises a new question of whether axisymmetric balance dynamics is robustly meaningful in high resolution simulations of tropical cyclone intensification. By robustly meaningful we mean that a solution actually exists. A particular problem is that, as shown by Smith et al. (2018a), the evolution of a vortex in a balanced formulation develops regions

of inertial instability in which the Sawyer-Eliassen equation becomes hyperbolic. In an attempt to overcome this problem, it is necessary to modify the coefficients of the Sawyer-Eliassen equation as regularization, which has been discussed in the last Chapter. Even if a mathematical solution of the regularized Sawyer-Eliassen equation could be shown to exist, an extensive region of regularization may be a reason for the SOR method to fail, unless the resolution of the model data in the Sawyer-Eliassen equation are coarsened.

As a first step in verifying the robustness of their findings, this chapter used an independent multi-grid solution method for solving the Sawyer-Eliassen equation. The purpose of this work is threefold: (1) explore whether balance theory can offer an explanation for upper tropospheric inflow jets; (2) to explore the sensitivity of the solutions to the particular method used; and (3) to assess the robustness of conclusions based on the SOR method. A specific question addressed is whether a convergence solution of the Sawyer-Eliassen equation for a high-resolution simulation can be obtained using a multi-grid method when the straightforward SOR method fails.

The main idea of a balance theory explanation for upper tropospheric inflow jets is presented in Section 5.1. I describe the calculation configuration and review briefly the SOR method and the more sophisticated multi-grid method in Section 5.2. The results of various sensitivity calculations are presented in Section 5.3. The conclusions are presented in Section 5.4.

5.1 On a balance theory explanation for upper tropospheric inflow jets

The foregoing ideas are illustrated in Figure 5.1, which shows in panel (b) the balanced response to the hypothetical lens of tangential momentum forcing, $-\dot{V}(r, z)$, in panel (a). The calculation assumes a tangential wind structure with a maximum of 50 m s^{-1} at a radius of 25 km at the surface. The tangential wind decreases sinusoidally with height to an altitude of 20 km and is zero above 20 km. The structure is indicated by the solid contours in panel (a). The corresponding balanced distribution of pressure and temperature are obtained using the unapproximated method of Smith (2006), assuming a latitude of 20°N and the Dunion moist tropical sounding (Dunion 2011) at some large radius. The Sawyer-Eliassen equation solved for the streamfunction of the secondary circulation is the most general form detailed in Chapter 4.

As in the case of a point source of tangential momentum, the secondary circulation forced by $-\dot{V}(r, z)$ in Figure 5.1(a) comprises a layer of outflow through the source and two layers of inflow sandwiching this outflow. The difference in vertical extent and strength between the upper and lower inflow layers is presumably related, in part, to the differences in inertial stability, $I^2 = \xi\zeta_a$, and static stability, $N^2 = -\frac{g}{\chi} \frac{\partial \chi}{\partial z}$, within or in the vicinity of these layers.

Figures 5.2(a) and 5.2(b) show the separate diagnosed contributions from generalized (including eddy terms implicitly) diabatic heating and tangential momentum forcing from

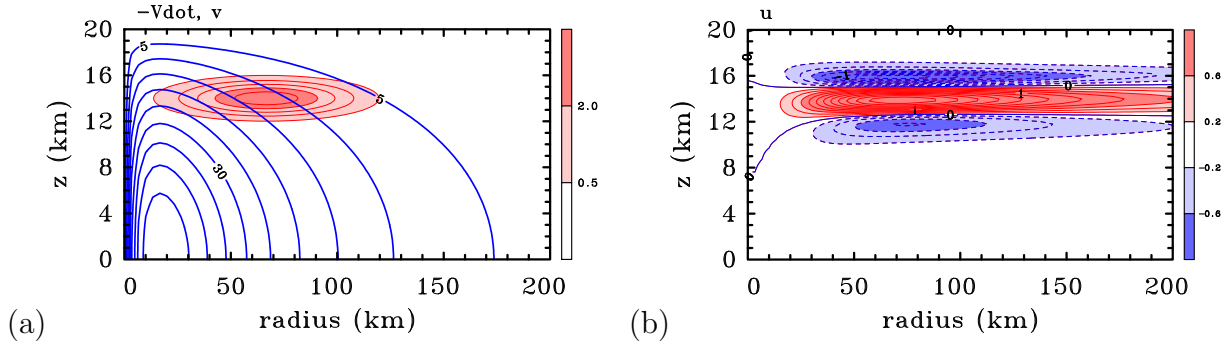


Figure 5.1: Axisymmetric balanced solution of an idealized tropical-cyclone-like vortex to a prescribed tangential momentum forcing in the upper troposphere. (a) contours of tangential velocity (contour interval 5 m s^{-1}) and upper-level tangential momentum source, $-\dot{V}(r, z)$ (shaded, contour interval 0.5 m s^{-1} per hour) and (b) radial velocity component of the axisymmetric balanced secondary circulation induced by this forcing (contour interval m s^{-1}). Shading values indicated on color bar.

60 h, a few hours before the quasi-steady period is reached. The principal feature of the diabatic heating is a tower of heating inside a radius of about 50 km with two radial tongues of heating centred at heights of about 13 and 15 km. There are narrow regions of cooling along the inner eyewall, a shallow finger of cooling just near the tropopause, and some isolated patches of cooling outside the eyewall. The main regions of momentum forcing are in the boundary layer and in the developing eyewall. These panels show also regions of negative I^2 , in which the flow is inertially unstable, and regions of negative discriminant of the Sawyer-Eliassen equation (see e.g. [Eq. (4.16)] in Chapter 4.).

Figures 5.2(c) and 5.2(d) show the balanced secondary circulation associated with the respective heating and momentum forcing in Figures 5.2(a) and 5.2(b), while Figure 5.2(e) shows the total balanced secondary circulation solution at 60 h and Figure 5.2(f) shows that in the simulation at the same time. Notably, the secondary circulation associated with the diabatic heating dominates that associated with the momentum forcing (compare panels (c) and (d)) and, in particular, accounts for much of the upper-level inflow above and below the outflow layer (compare panels (c) and (e)) in the balance solution.

Comparison of the balanced secondary circulation with the azimuthally-averaged circulation in the simulation indicates that the mean height of the outflow is too low (12 km compared with 14 km) and the outflow is split at larger radii in the balance solution. There are strong discrepancies also in the strength and radial extent of the inflow layer. For example, the inflow below the outflow layer is approximately twice as strong in the balance solution and the inflow layer above the outflow layer is barely evident. The boundary layer inflow in the balance solution is significantly weaker than in the simulation (maximum inflow 8.3 m s^{-1} compared with 24.5 m s^{-1}), but is much deeper in the inner region, supporting findings of Montgomery and Persing (2020). However, in order to obtain a convergent solution for the balanced secondary circulation, I needed to coarsen the interpolated simulation data to 2 km in the radial direction and 500 m in the vertical

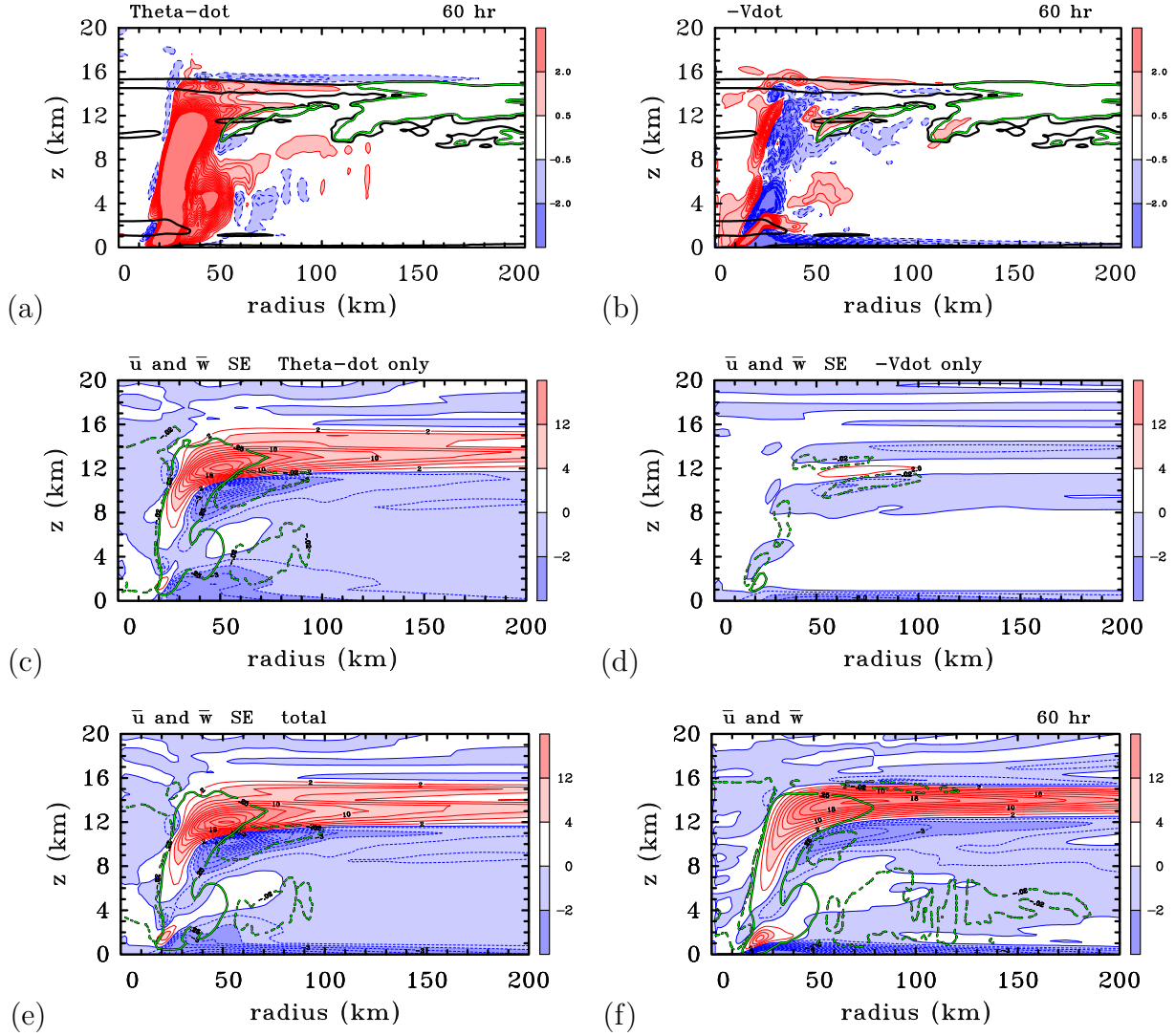


Figure 5.2: For comparison, (a, b) show the generalized diabatic heating (K per hour) and generalized tangential momentum forcing (m s^{-1} per hour) from the numerical simulation at 60 h. (c) and (d) show the corresponding balanced secondary circulation associated the separate heat forcing (a) and momentum forcing (b). (e) shows the total balanced secondary circulation solution at 60 h and (f) shows that in the simulation at the same time. All fields in (a, b, f) are azimuthally-averaged and time-averaged for one hour. Contour interval for diabatic heating and momentum forcing is 0.5 m s^{-1} per hour (red contours positive, blue contours negative), for 2 m s^{-1} when $\bar{u} > 0$, 1 m s^{-1} when $\bar{u} < 0$. For \bar{w} only two contours are shown: 0.25 m s^{-1} and -0.02 m s^{-1} . Shading values indicated on colour bar. In panel(a, b), the green contour is that of zero inertial stability, while the black contour is that of zero discriminant.

direction. The computational domain consists of a cylindrical region 200 km in radius and 20 km in height. Amongst other things, this coarsening shrinks the region in which the

discriminant of the Sawyer-Eliassen equation is negative (discussed in next section) and suggests a fundamental limitation of balance dynamics for highly-resolved tropical-cyclone-like flows. This point is underscored by our cursory application of the balance inversion at other times. Additional experience suggests that a coarsened solution is typically possible at 60 h and before. At later times, however, the regions of negative discriminant become too extensive in the outflow layer and even regularization is inadequate to achieve a convergent solution.

In summary, the balance secondary circulation broadly reproduces the main features of the simulated circulation and seems to indicate that the balanced inflow below the upper-level outflow layer arises from the spatial gradients of the diabatic heating rate. In terms of the balance model, the inflow is just that required to keep the main vortex in thermal wind balance in the presence of heat forcing. In other words, this inflow is the response needed to keep the vortex in balance.

That this overturning circulation broadly captures the main feature of the simulated flow is, in fact, a consequence of imposing the vertical mass flux associated with the diabatic heating rate. For this flow regime, the vertical velocity is largely obtained by balancing the adiabatic cooling with the diabatic heating and hence the vertical velocity is essentially proportional to the diabatic heating rate. Given the rapidly-rotating environment of the hurricane and the strongly nonlinear forcing associated with the frictional boundary, there is no reason to expect the detailed features of the simulation to match those of the balance calculation.

The inability of the balance calculation to capture the secondary circulation in the simulation quantitatively is not surprising and consistent with the fact that, as shown in the next section, there are large regions in the upper troposphere where the gradient wind balance approximation is nowhere near satisfied. The same can be said about the low-level inflow layer in the inner core region where the maximum tangential winds are being generated.

Furthermore, there are large regions in the upper troposphere where the discriminant of the Sawyer-Eliassen equation for the secondary circulation is negative (the regions enclosed by black curves in Figures 5.2(a) and 5.2(b)). In that case, to obtain a strictly balanced solution, one can only invert the Sawyer-Eliassen equation by modifying (or regularizing) the coefficients in such a way that the equation is rendered elliptic. However, the issues of regularization described in Chapter 4 has shown that the secondary circulation within and near these upper-level unstable regions is particularly sensitive to the way in which the regularization is carried out, especially where the forcing overlaps with these regions. This sensitivity casts doubt on the reliability of any inferences based on balance ideas. It is worth noting that the main region where the two fields in Figures 5.2(e) and 5.2(f) show a significant departure is precisely where the discriminant of the Sawyer-Eliassen equation is negative.

In light of these considerations, it would appear that a more fundamental framework for understanding the secondary circulation and the implied tangential wind tendency associated with it is needed. Returning to Newton's second law of motion is the recommended path for improved understanding. In this framework, balance is not an imposed constraint

on the flow dynamics.

5.2 Sensitivity calculations and methods

5.2.1 Calculation overview

In order to further verify the conjecture of the applicability of the balance solution in the previous section, four sets of calculations are carried out to compare the balanced solutions for the streamfunction of the secondary circulation of tropical-cyclone-like flows obtained using the SOR and multigrid solution methods.

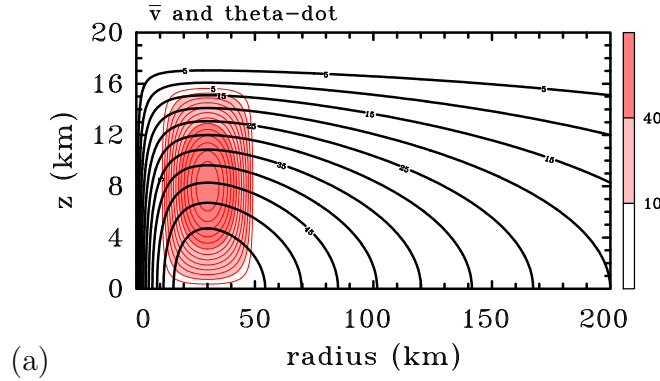


Figure 5.3: The idealized tropical-cyclone-like vortex to a prescribed diabatic heating rate in Calc-A. Shown are contours of tangential velocity (black thick contour interval 5 m s^{-1}) and prescribed diabatic heating, $\dot{\theta}(r, z)$ (shaded, contour interval 5 K per hour).

The first set of calculations, referred to as Calc-A, relate to the balanced streamfunction of an idealized tropical-cyclone-like vortex defined by a specified tangential wind profile, $v(r, z)$, forced by a specified distribution of diabatic heating rate $\dot{\theta}(r, z)$, where

$$v(r, z) = V_m \left(\frac{r}{r_m} \right) \exp \left[\frac{1}{b} \left(1 - \left(\frac{r}{r_m} \right)^b \right) \right] \cos \left(\frac{\pi z}{2z_d} \right), \quad (5.1)$$

with $b = 0.45$, $V_m = 60 \text{ m s}^{-1}$, $r_m = 30 \text{ km}$, $z_d = 18 \text{ km}$, and

$$\begin{aligned} \dot{\theta}(r, z) &= \dot{\Theta} \cos \left(\frac{1}{2} \pi \frac{\delta r}{r_w} \right) \cos \left(\frac{1}{2} \pi \frac{\delta z}{z_w} \right) \quad (|r - r_c| < r_w) \\ &= 0 \quad \text{elsewhere,} \end{aligned} \quad (5.2)$$

with $\delta r = r - r_c$, $\delta z = z - z_c$, $r_c = 30 \text{ km}$, $z_c = 8 \text{ km}$, $r_w = 20 \text{ km}$ and $z_w = 8 \text{ km}$. In these formulae: V_m is the maximum tangential wind speed, which occurs at the surface at radius r_m ; r_c and z_c are the radius and height of the maximum diabatic heating; $\dot{\Theta} = 70 \text{ K h}^{-1}$ is the maximum amplitude of the heating rate, r_w and z_w is the width and half height of the heating function. The tangential wind decreases sinusoidally with height to

an altitude of $z_d = 18$ km and is set to zero above 18 km. There is no momentum forcing in these particular calculations. The prescribed structure of tangential wind and diabatic heating is shown in Figure 5.3.

The set of calculations, Calc-B, relate to the balanced secondary circulation at 60 h of the simulation. The tangential wind field is azimuthally-averaged and time-averaged for one hour using 1 minute output data and the corresponding balanced pressure and temperature distribution are obtained by using the unapproximated method of Smith (2006), assuming a latitude of 20°N and the Dunion moist tropical sounding (Dunion 2011) at some large radius. The original horizontal grid spacing is 1 km from the model output and there are 78 vertical levels from 0 km to 25 km. The vertical grid spacing is 100 m in the first 1 km and 500 m from 16 km to 25 km. Between 1 km and 16 km, the vertical grid spacing is uniformly stretched.

The set of calculations, Calc-C, relate to the balanced secondary circulation of the vortex structure at 60 h. but with the prescribed diabatic heating rate in Calc-A, while the set of calculations Calc-D relate to the balanced secondary circulation of the vortex structure in Calc-A, but with the diabatic heating and momentum forcing at 60 h. The full set of calculations is summarized in Table 5.1.

Calculation	vortex	forcing
Calc-A	ideal	ideal
Calc-B	model	model
Calc-C	model	ideal
Calc-D	ideal	model

Table 5.1: Summary of all calculations

Each set of calculations is performed with the SOR and multi-grid method with different radial and/or vertical resolution. To meet the special requirements of the multi-grid method in relation to the number of grid points, the computational domain of each case consists of a cylindrical region 256 km in radius and 19.2 km in height.

Table 5.2 shows the number of non-elliptic points in Calc-B and Calc-C. It is clear that, the number of non-elliptic grid points increases with decreasing grid spacing. Figure 5.4 shows that the negative discriminant area is broader at the finest resolution (panel (b)) than at the coarsest resolution (panel (a)), especially in the upper-troposphere. Furthermore, the regions of static and symmetric instability are somewhat more extensive in the upper-troposphere. It is foreseeable that the increase in negative discriminant area in the case of higher resolution might lead to additional difficulty in solving the Sawyer-Eliassen equation.

5.2.2 Successive Over-Relaxation (SOR) method

On the discrete (r, z) mesh of points, the solver iterates for ψ by linearly marching through the grid mesh and minimizing the residual R defined by

$$R = \bar{A}\delta_{rr}\psi + 2\bar{B}\delta_{rz}\psi + \bar{C}\delta_{zz}\psi + \bar{D}\delta_r\psi + \bar{E}\delta_z\psi - \dot{\Theta}. \quad (5.3)$$

Non-elliptic	$dz = 600 \text{ m}$	$dz = 300 \text{ m}$	$dz = 150 \text{ m}$
$dr = 2 \text{ km}$	558	1273	2517
$dr = 1 \text{ km}$	1119	2559	5064

Table 5.2: Number of non elliptic points in Calc-B and Calc-C for different radial and vertical grid spacings, dr and dz , respectively.

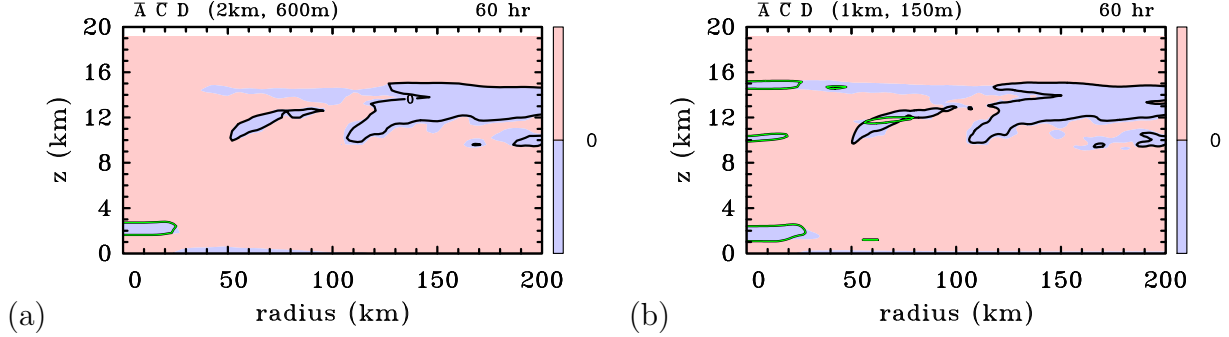


Figure 5.4: Sign of the coefficients \bar{A} , \bar{C} and the discriminant $D = (\bar{A}\bar{C} - \bar{B}^2)$ in the Sawyer-Eliassen equation (Eq. 4.14) for Calc-B and Calc-C with (a) $dr = 2 \text{ km}$, $dz = 600 \text{ m}$ and (b) $dr = 1 \text{ km}$, $dz = 150 \text{ m}$. The quantities \bar{A} and \bar{C} are proportional to the static stability and inertial stability, respectively, while the quantity \bar{B} characterizes, in part, the strength of the vertical shear of the gradient wind. \bar{A} (zero lines as green), \bar{B} (zero lines as black) and D (shaded, blue for negative, red for positive).

Here, the operator δ represents a discrete partial derivative in the direction of the subscript, with second-order derivatives having subscripts. The streamfunction at iteration step $k+1$ is obtained from that at step k by successive over-relaxation:

$$\psi_{k+1} = \psi_k + \frac{\omega R_k}{2} \left[\frac{\bar{A}}{(\Delta r)^2} + \frac{\bar{C}}{(\Delta z)^2} \right]^{-1} \quad (5.4)$$

where \bar{A} , \bar{B} , \bar{C} and $\bar{\Theta}$ are defined in Eq. 4.14,

$$\bar{D} = \frac{\partial \bar{A}}{\partial r} + \frac{\partial \bar{B}}{\partial z}, \quad (5.5)$$

$$\bar{E} = \frac{\partial \bar{B}}{\partial r} + \frac{\partial \bar{C}}{\partial z}, \quad (5.6)$$

and $\omega = 1.8$ is the empirically chosen over-relaxation parameter (generally between 1.0 and 2.0). The iteration is deemed to have converged if the maximum difference in ψ between two iteration steps is less than 10^{-8} times the maximum magnitude of the solution at all interior (r, z) grid points. This criterion follows the suggestion of Adams 1991 in his multi-grid method. Other technical details of the method can be found in Press et al. (1992) page 866–870.

5.2.3 Multi-grid (MG) method

The multi-grid method is an iteration method that has become quite popular and versatile for solving linear elliptic partial differential equations and even some nonlinear problems (Adams 1991). Although the method is not an over-relaxation method in the traditional sense, the method takes advantage of the fact that the residual error damps more quickly on small scales than larger scales of the grid mesh. The difference in error attenuation between the small and large scales allows one to cycle between small-scale and large scale grids in order to accelerate the convergence rate of the solution. Specifically, the fine grid is used to eliminate the high-frequency oscillation error; the elimination of the low-frequency oscillation error is accomplished by the coarser grids and the coarse-grid solution is then projected back onto the fine grid and the cycle is repeated and so on until the residual decreases to a given error criterion. Because the convergence speed of the low-frequency oscillation error in the coarse grid is faster than on the original grid, the multi-grid method is generally much faster than other classical, one-scale, iteration methods, such as SOR, Gauss-Siedel or Jacobi iteration. The computational efficiency of the multi-grid method is generally very high because the method scales in proportion to the number of grid points of the mesh. An excellent tutorial on multi-grid methods and their relation to the classical one-scale iteration methods is provided by Briggs et al. 2000.

For the continuous elliptic partial differential equation,

$$l(x) = AX = f \quad (5.7)$$

Assume $G(0) < \dots < G(s) < \dots G(st) = G$ is an ascending chain of subgrids terminating in grid G and

$$A(s)X(s) = F(s) \quad (5.8)$$

denote the discretization of Eq. 5.7 on $G(s)$ for each $s = 0, 1, \dots, st$. Where $G(s-1)$ is a subset of $G(s)$ which includes boundaries, and A is the coefficient matrix. Now we define a prolongation operator $I(s-1, s)$ for transferring grid values from a coarser grid $G(s-1)$ to a fine grid $G(s)$ and a restriction operator $I(s, s-1)$ for transferring grid values from a fine grid $G(s)$ to a coarser grid $G(s-1)$.

The steps of multigrid solver in this study followed:

- 1. Perform relaxation sweeps on

$$A(s)X(s) = f(s) \quad (5.9)$$

- 2. Compute the residual

$$R(s) = F(s) - A(s)X(s) \quad (5.10)$$

- 3. Restrict the residual to $G(s-1)$

$$f(s-1) = I(s, s-1)R(s) \quad (5.11)$$

- 4. Solve

$$A(s-1)E(s-1) = f(s-1) \quad (5.12)$$

- 5. Prolong the correction $E(s-1)$ to $G(s)$ and add to $X(s)$

$$X(s) = X(s) + I(s-1, s)E(s-1) \quad (5.13)$$

- 6. Perform more relaxation sweeps on the new

$$A(s)X(s) = F(s) \quad (5.14)$$

On step “Solve”, all steps 1-6 can be used for the correction term on $G(s-1)$.

- 7. Prolong $X(s)$ to $G(s+1)$

$$X(s+1) = I(s, s+1)X(s) \quad (5.15)$$

Repeating all these steps for $s = 0, 1, \dots, st - 1$ lifts the approximation to the finest grid level. Once the fine grid $G(st)$ is reached, steps 1-6 can be repeated with $s = st$ until the desired accuracy is achieved. In this study, for keeping robustness, the W-Cycle is used.

In the implementation of the multi-grid method herein, the same convergence criterion is employed as for the SOR method discussed above.

5.3 Results

5.3.1 Calculation set Calc-A

This set of twelve calculations Calc-A comprise six using the SOR method and six using the multi-grid method with a combination of $dr = 1$ km or 2 km and $dz = 150$ m, 300 m, or 600 m. Figures 5.5 and 5.6 show radial and vertical velocity components structure for a selection of these calculations. The 1 km radial grid spacing corresponds to the spacing in the model simulation used to generate the data for Calc-B. The panels in the left column show the solutions using the multi-grid method and the right columns show those using the SOR method. From these figures, it is seen that the flow in all panels is essentially the same, confirming the integrity of both solution methods.

The maximum inflow occurs near the surface while the maximum outflow occurs at a height of about 15 km. The strongest ascent occurs in the region of maximum heating, a feature to be expected from the study of Shapiro and Willoughby (1982) and Smith et al. (2018a). As shown in Table 5.3, the maximum inflow for each of the 12 cases differs by no more than 0.2 m s^{-1} and the maximum outflow differs by no more than 0.1 m s^{-1} . In essence, for this idealized case, the multi-grid and SOR methods give essentially the same results, irrespective of grid spacing.

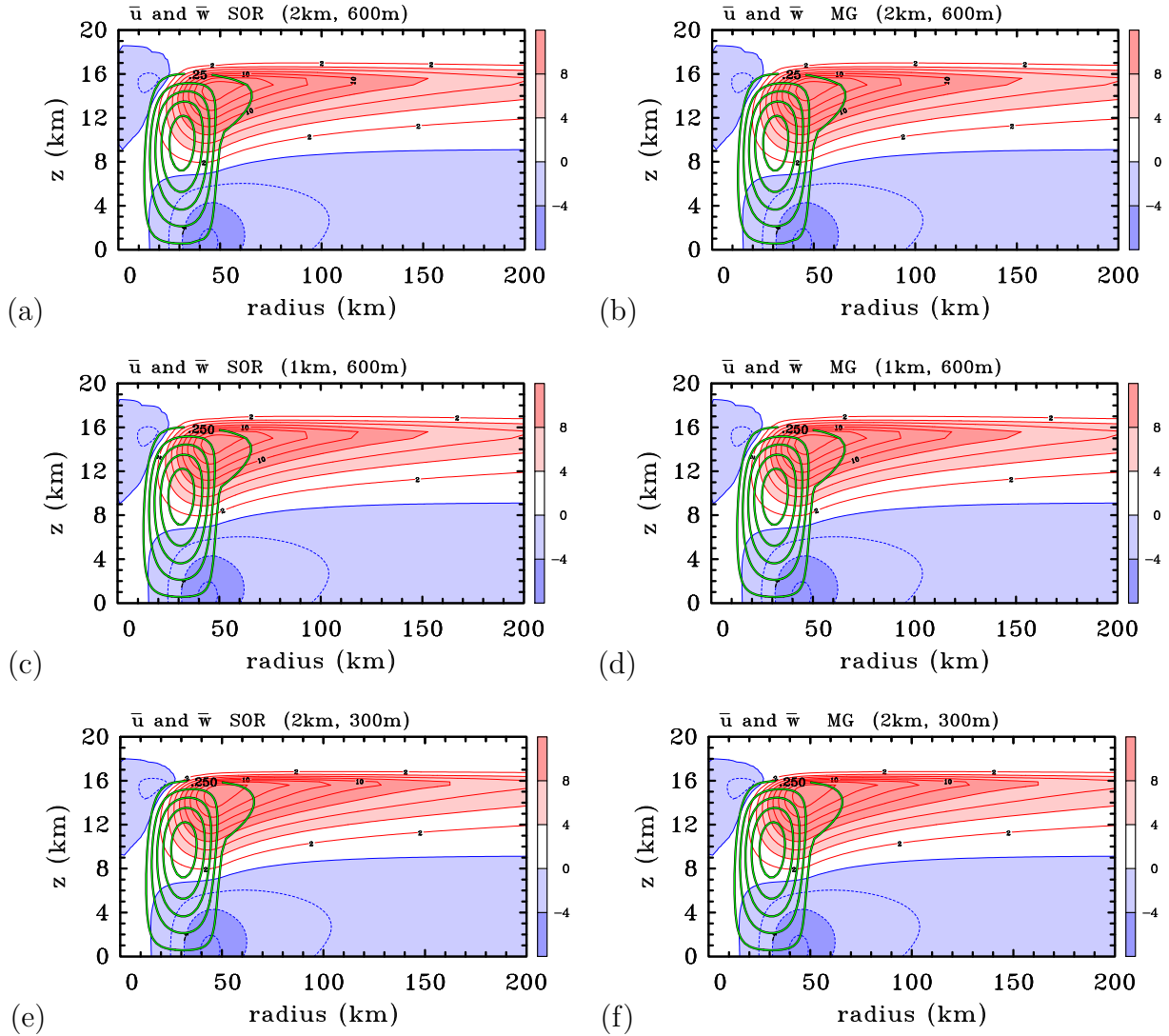


Figure 5.5: Axisymmetric balanced solutions for the radial (\bar{u}) and vertical (\bar{w}) components of the secondary circulation in a subset of Calc-A. The calculations differ in the method of solution (left columns SOR, right columns multigrid) and the radial and vertical grid spacing (dr, dz): (a) and (b) $dr = 2$ km, $dz = 600$ m; (c) and (d) $dr = 1$ km, $dz = 600$ m; (e) and (f) $dr = 2$ km, $dz = 300$ m. Contour interval for \bar{u} : 2 m s^{-1} when $\bar{u} > 0$, 1 m s^{-1} when $\bar{u} < 0$. Positive contours solid, negative contours dashed. Shading values indicated on color bar. Green thick contours are shown for \bar{w} : 0.25 m s^{-1} (Only positive values are shown).

5.3.2 Calculation set Calc-B

We turn now to examine in more depth the solutions for the balanced secondary circulation in the high-resolution tropical cyclone simulation presented by Chapter 3 forced by the azimuthally averaged diabatic heating and tangential momentum forcing (including the

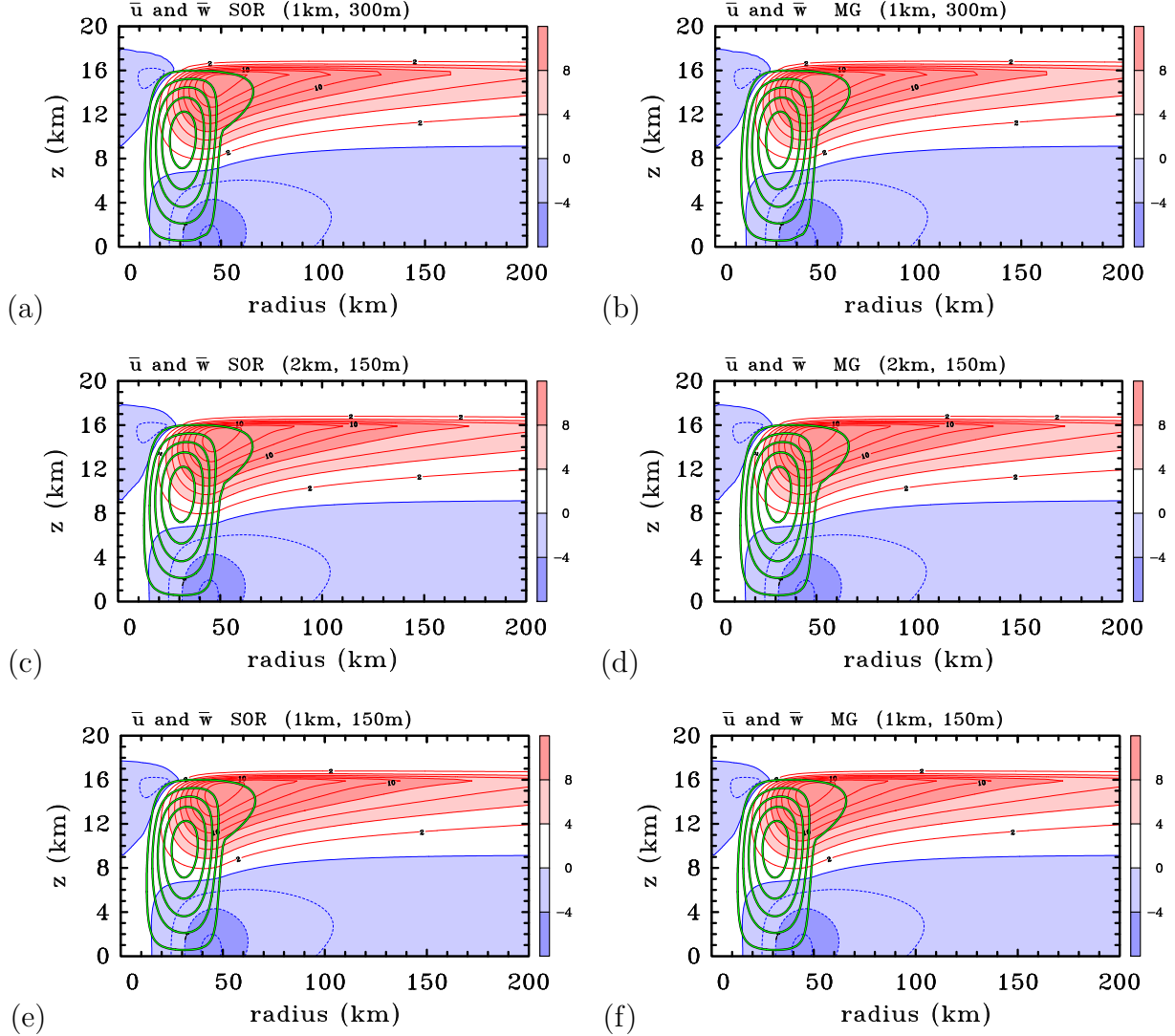


Figure 5.6: Axisymmetric balanced solutions for the radial (\bar{u}) and vertical (\bar{w}) components of the secondary circulation in a subset of Calc-A. The calculations differ in the method of solution (left columns SOR, right columns multigrid) and the radial and vertical grid spacing (dr, dz): (a) and (b) $dr = 1$ km, $dz = 300$ m; (c) and (d) $dr = 2$ km, $dz = 150$ m; (e) and (f) $dr = 1$ km, $dz = 150$ m. Contour interval for \bar{u} : 2 m s^{-1} when $\bar{u} > 0$, 1 m s^{-1} when $\bar{u} < 0$. Positive contours solid, negative contours dashed. Shading values indicated on color bar. Green thick contours are shown for \bar{w} : 0.25 m s^{-1} (Only positive values are shown).

eddy terms) diagnosed from the simulation at 60 h. These forcing distributions are shown in Figures 5.2. Table 5.4 shows that, as the resolution increases, convergence solutions become harder to obtain. Figure 5.7 compares solutions for the balanced secondary circulation with different grid resolutions with that obtained from the azimuthally averaged output from

Calc-A	method	outflow	inflow
dr = 2 km, dz = 600 m	SOR MG	17.6 17.6 m/s	-6.4 -6.4 m/s
dr = 1 km, dz = 600 m	SOR MG	17.6 17.6 m/s	-6.5 -6.4 m/s
dr = 2 km, dz = 300 m	SOR MG	17.4 17.4 m/s	-6.4 -6.4 m/s
dr = 1 km, dz = 300 m	SOR MG	17.5 17.5 m/s	-6.5 -6.4 m/s
dr = 2 km, dz = 150 m	SOR MG	17.4 17.4 m/s	-6.4 -6.4 m/s
dr = 1 km, dz = 150 m	SOR MG	17.4 17.4 m/s	-6.5 -6.4 m/s

Table 5.3: Maximum values of inflow and outflow for each case in Calc-A.

the simulation, itself, at 60 h. Figure 5.7(a) shows the azimuthally-averaged circulation in the simulation while Figure 5.7(b) shows the corresponding balanced solution obtained using the SOR method with a radial grid spacing of 2 km and vertical grid spacing of 600 m. This choice of grid configuration is coarser than that used for the simulated vortex for reasons discussed at the beginning of this Chapter.

As noted in Section 5.2, the mean height of the balanced outflow is too low (12 km compared with 14 km) and the outflow is split at larger radii in the balanced solution. There are strong discrepancies also in the strength and radial extent of the inflow layers. For example, the inflow below the outflow layer is approximately twice as strong in the balanced solution and the inflow layer above the outflow layer is barely evident. The maximum radial velocity in the upper level outflow in the balance solution is 23.3 m s^{-1} compared with 20.3 m s^{-1} in the simulation. The boundary layer inflow in the balance solution is significantly weaker than in the simulation (maximum inflow 7.5 m s^{-1} compared with 24.5 m s^{-1} , a factor of three discrepancy), but is much deeper in the inner region as found by Montgomery and Persing (2020).

Figure 5.7(c) shows the balance solution using the multi-grid method with the same grid configuration as in Figure 5.7(b). Comparing Figures 5.7(b) and 5.7(c) it is seen that the multi-grid solution is almost the same as that obtained with SOR. Indeed, the maximum upper-level outflow and inflow have comparable values (Table 5.5), but the outflow and inflow weaken slightly faster with radius with the multi-grid method. Again, the boundary layer inflow in the balance solution is much weaker than in the numerical simulation, reflecting the fact that the balance assumption in the boundary layer is poor.

When the vertical grid spacing is halved, the SOR method failed to converge, but a convergent solution is still possible using the multi-grid method (Figure 5.7(d)). However, this solution is significantly different in detail from that with the coarser vertical resolution in Figure 5.7(c). The outflow layer has a stronger maximum and has a more obvious two-layer structure at large radii. The upper inflow is stronger also and extends to a larger radius, even exceeding the strength of that in the numerical simulation. Although the maximum boundary layer inflow is larger also, its strength is still greatly underestimated relative to that of the simulation. When the vertical grid spacing is halved again to 150 m, neither solution methods converge (Table 5.4).

When the radial grid spacing is reduced to 1 km, the same as in the numerical simulation

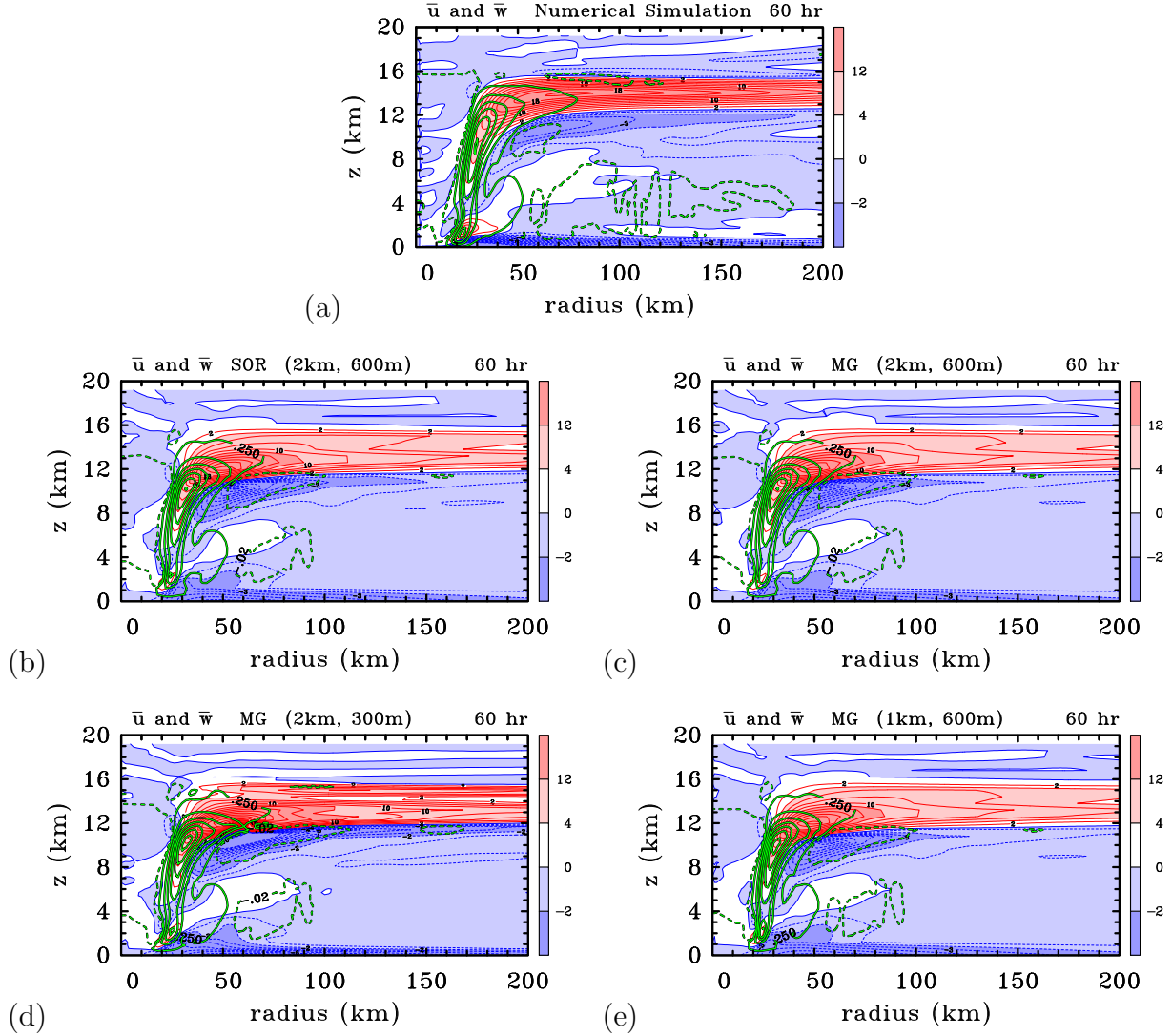


Figure 5.7: Axisymmetric balanced solutions for the radial (\bar{u}) and vertical (\bar{w}) components of the secondary circulation at 60 h in the numerical simulation (panel (a)) and in a subset of axisymmetric balanced solutions for Calc-B. The fields in panels (a) are azimuthally-averaged and time-averaged for one hour using 1 min output. (b) SOR and (c) multi-grid with $dr = 2$ km, $dz = 600$ m. (e) multi-grid with $dr = 2$ km, $dz = 300$ m; (f) multi-grid with $dr = 1$ km, $dz = 600$ m. Contour interval for 2 m s^{-1} when $\bar{u} > 0$, 1 m s^{-1} when $\bar{u} < 0$. Positive contours solid, negative contours dashed. Shading values indicated on color bar. Only two thick contours are shown for \bar{w} . For $\bar{w} > 0$, 0.25 m s^{-1} (green, solid); for $\bar{w} < 0$, -0.02 m s^{-1} (green, dashed). Shading values indicated on colour bar.

(Figure 5.7(e)), a convergent solution is possible only using the multi-grid method and only then using the coarsest vertical grid spacing of 600 m. The solution in this case is virtually indistinguishable from that in Figure 5.7(c). These findings support that of Chapter 4,

Section 5.1 and Montgomery and Persing (2020) indicating that the balance solution has intrinsic limitations in diagnosing the secondary circulation of the numerical simulation.

Calc-B	SOR	MG
dr = 2 km, dz = 600 m	solvable	solvable
dr = 2 km, dz = 300 m	unsolvable	solvable
dr = 2 km, dz = 150 m	unsolvable	unsolvable
dr = 1 km, dz = 600 m	unsolvable	solvable
dr = 1 km, dz = 300 m	unsolvable	unsolvable
dr = 1 km, dz = 150 m	unsolvable	unsolvable

Table 5.4: Summary of SOR and multi-grid performance for Calc-B.

Table 5.5 shows maximum values of inflows and outflow for each case in Calc-B. Although the extreme values of the outflow jets seem to be comparable at a coarser resolution, as the resolution increases, the difference increases rapidly, even doubled. For upper inflow jets, its intensity at higher resolution is even tripled compared to the simulation. And boundary inflows also have no comparability.

Calc-B	outflow	upper-inflow	inflow
Simulation	20.3 m/s	-4.9 m/s	-24.5 m/s
SOR, 2 km, 600 m	23.3 m/s	-10.2 m/s	-7.5 m/s
MG, 2 km, 600 m	22.8 m/s	-9.7 m/s	-7.5 m/s
MG, 2 km, 300 m	38.9 m/s	-14.8 m/s	-9.2 m/s
MG, 1 km, 600 m	22.8 m/s	-9.7 m/s	-7.5 m/s

Table 5.5: Maximum values of inflow and outflow for each case in Calc-B.

Table 5.6 shows the root mean square error between the radial velocity in the model simulation and that in two of the balance solutions in Calc-B. The root mean square error (RMSE) is defined as

$$RMSE = \sqrt{\frac{1}{n} \sum_{i=0}^n (e_i)^2}, \quad (5.16)$$

where n is the number of sample points, e_i is the difference between the model simulation and balance solution. The two balance solutions are those obtained using the SOR method and multi-grid method with a radial grid spacing of 2 km and a vertical grid spacing of 600 m shown in Figures 5.7(b) and 5.7(c). In each calculation there are 3333 grid points, 470 inside the regularization region and 2863 outside. For the SOR calculation, the RMSE is 3.1 m s^{-1} over the whole domain, 6.3 m s^{-1} inside the regularization region and 2.1 m s^{-1} outside the regularization region. Since the mean radial velocity over the domain in the simulation is only 0.7 m s^{-1} , the agreement between the balance calculation and the

simulation is rather poor. The RMSEs for the multi-grid calculation are only marginally better than those for the SOR calculation, showing again that the balance calculation is rather poor for diagnosing the secondary circulation of the numerical simulation, especially in the region of regularization.

Calc-B/600m-2km	SOR	MG
Whole domain	3.1 m/s	3.0 m/s
Inside regularization region	6.3 m/s	6.0 m/s
Outside regularization region	2.1 m/s	2.1 m/s

Table 5.6: Point-by-point Root Mean Square Error between the radial velocity in the numerical simulation at 60 hours and that in two balance calculations of the set Calc-B, those shown in Figures 5.7(b) and 5.7(c).

5.3.3 Calculation set Calc-C

In an effort to pinpoint the reasons for the failure of the SOR and multi-grid methods to converge for lower grid spacings in calculation set Calc-B, we turn first to a set of calculations with the same vortex structure in Calc-B, but with the idealized forcing used in Calc-A. The tangential wind structure and prescribed diabatic heating rate used in Calc-C are shown in Figure 5.8(a). As in Calc-B, there are regions where the discriminant of the Sawyer-Eliassen equation is negative (Figure 5.4) and the equation requires regularization. Even though the diabatic heating rate in these calculations has a regular shape, the secondary circulation has more structure than in Figures 5.5 and Figures 5.6 with an inflow layer beneath the upper-level outflow. And the maximum values of inflows and outflow for each case are shown in Table 5.7

The two solutions with the same grid spacing are similar with two local maxima in the upper-level outflow (Figure 5.8(b,c)). However, the multi-grid solution with the same radial grid spacing, but a vertical grid spacing of 300 m has three local maxima within the outflow layer and a much stronger upper level inflow (Figure 5.8(d)). As in Calc-B and as detailed in Table 5.7, the SOR method does not converge with a 300 m vertical grid spacing and neither solution method converges with a 150 m vertical grid spacing.

When the radial grid spacing is reduced to 1 km, it is only possible to obtain a solution with the multi-grid method and only then with a vertical grid spacing of 600 m. This solution, which is shown in Figure 5.8(e), is virtually the same as the solution with a 2 km radial grid spacing in Figure 5.8(b).

These results suggest that the solution is less sensitive to changes in the radial resolution than to changes in the vertical resolution, at least where a convergent solution is possible.

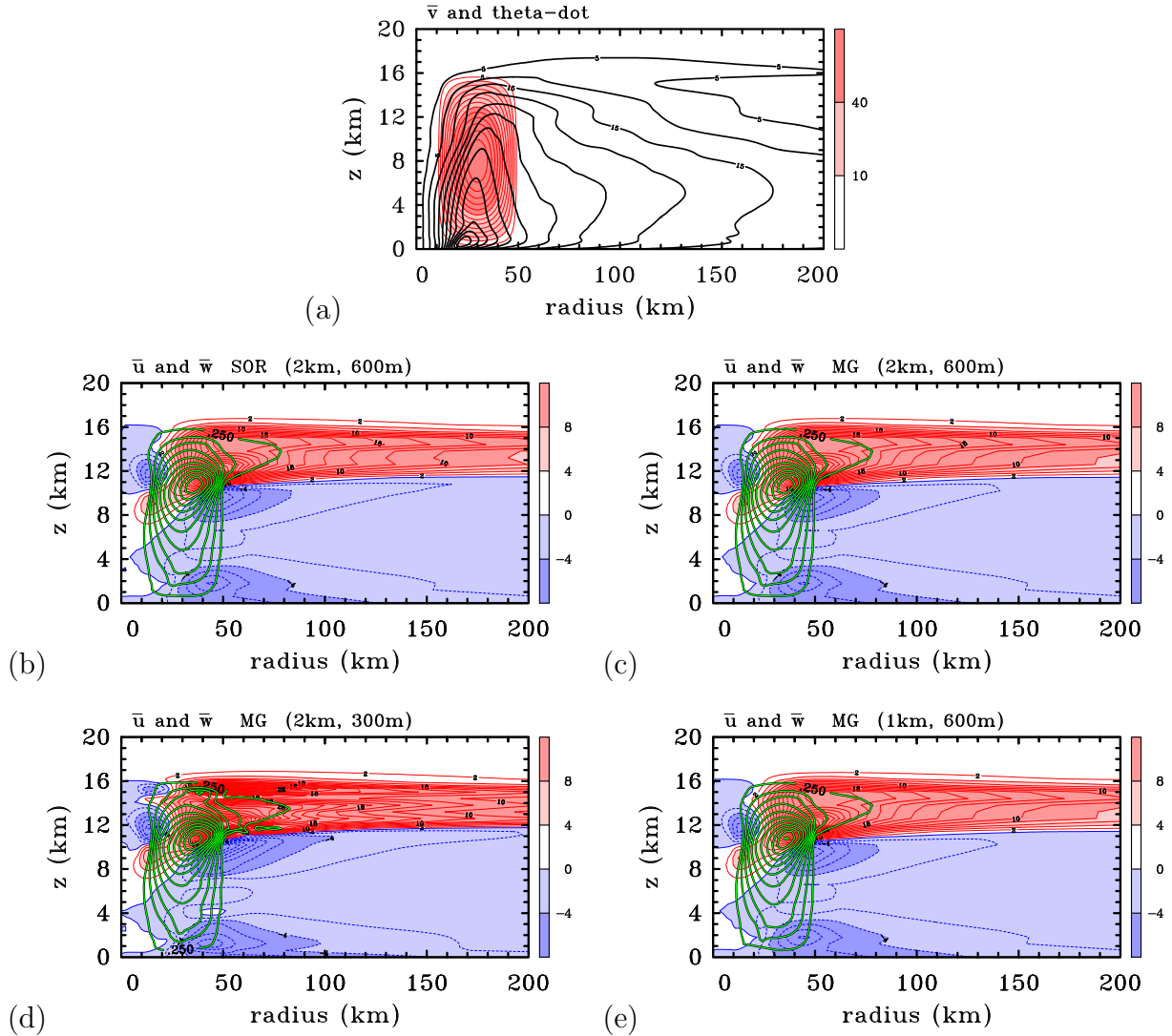


Figure 5.8: Axisymmetric balanced solutions for the radial (\bar{u}) and vertical (\bar{w}) components of the secondary circulation in a subset of Calc-C. For comparison, panel (a) shows the tangential wind from the numerical simulation at 60 h and a prescribed diabatic heating rate (K per hour). (b) SOR method, $dr = 2$ km, $dz = 600$ m. Panels (c)-(e) use the multi-grid method with (c) $dr = 2$ km, $dz = 600$ m; (d) $dr = 2$ km, $dz = 300$ m; (e) $dr = 1$ km, $dz = 600$ m. Contour interval for \bar{u} : 2 m s^{-1} when $\bar{u} > 0$, 1 m s^{-1} when $\bar{u} < 0$. Positive contours solid, negative contours dashed. Shading values indicated on color bar. Green thick contours are shown for \bar{w} : 0.25 m s^{-1} (Only positive values are shown).

5.3.4 Calculation set Calc-D

The final set of calculations, Calc-D, uses the full diabatic heating and momentum forcing (including that from the eddies) from the numerical simulation, as in Calc-B, but incorporate the idealized vortex structure in Calc-A. The unique feature is that this vortex is

Calc-C	SOR	MG
dr=2km, dz=600m	solvable	solvable
dr=2km, dz=300m	unsolvable	solvable
dr=2km, dz=150m	unsolvable	unsolvable
dr=1km, dz=600m	unsolvable	solvable
dr=1km, dz=300m	unsolvable	unsolvable
dr=1km, dz=150m	unsolvable	unsolvable

Table 5.7: Summary of SOR and multi-grid performance for Calc-C.

Calc-C	outflow	upper-inflow	inflow
SOR, 2 km, 600 m	42.8 m/s	-12.4 m/s	-10.3 m/s
MG, 2 km, 600 m	42.4 m/s	-12.2 m/s	-10.3 m/s
MG, 2 km, 300 m	53.6 m/s	-18.2 m/s	-11.5 m/s
MG, 1 km, 600 m	42.5 m/s	-12.1 m/s	-10.3 m/s

Table 5.8: Maximum values of inflows and outflow for each case in Calc-C.

everywhere symmetrically stable and the Sawyer-Eliassen equation does not require regularization. The balanced secondary circulation for this set of calculations is shown in Figures 5.9, 5.10 and 5.11.

The four calculations with 600 m vertical grid spacing and either 1 or 2 km radial grid spacing in Figure 5.9 show similar structures with a hint of a second outflow maximum above the main outflow layer. The second outflow maximum is presumably related to the fine structure of the diabatic heating rate.

With a vertical grid spacing of 300 m, the second outflow feature becomes more marked using both solution methods (Figure 5.10), while in the finest resolution solutions (Figure 5.11(c) and (d)), the second outflow structure is even more pronounced. Again, the radial resolution change shows less sensitive as mentioned in the last subsection.

Notably, there is no concentrated inflow layer below the main outflow layer as in Calc-B and Calc-C. This result indicates that the upper-level inflow layer in Calc-B and Calc-C is mainly a consequence of the need to regularize the coefficients of the Sawyer-Eliassen equation in regions of symmetric instability. The implications of this finding are discussed in the next section.

As shown in Table 5.9, when the resolutions increase, flow extrema increase marginally. For the case of the same resolution, both two solution methods give essentially the same results. Most importantly, without the need to regularize the Sawyer-Eliassen equation, a convergent solution can be obtained using both solution methods.

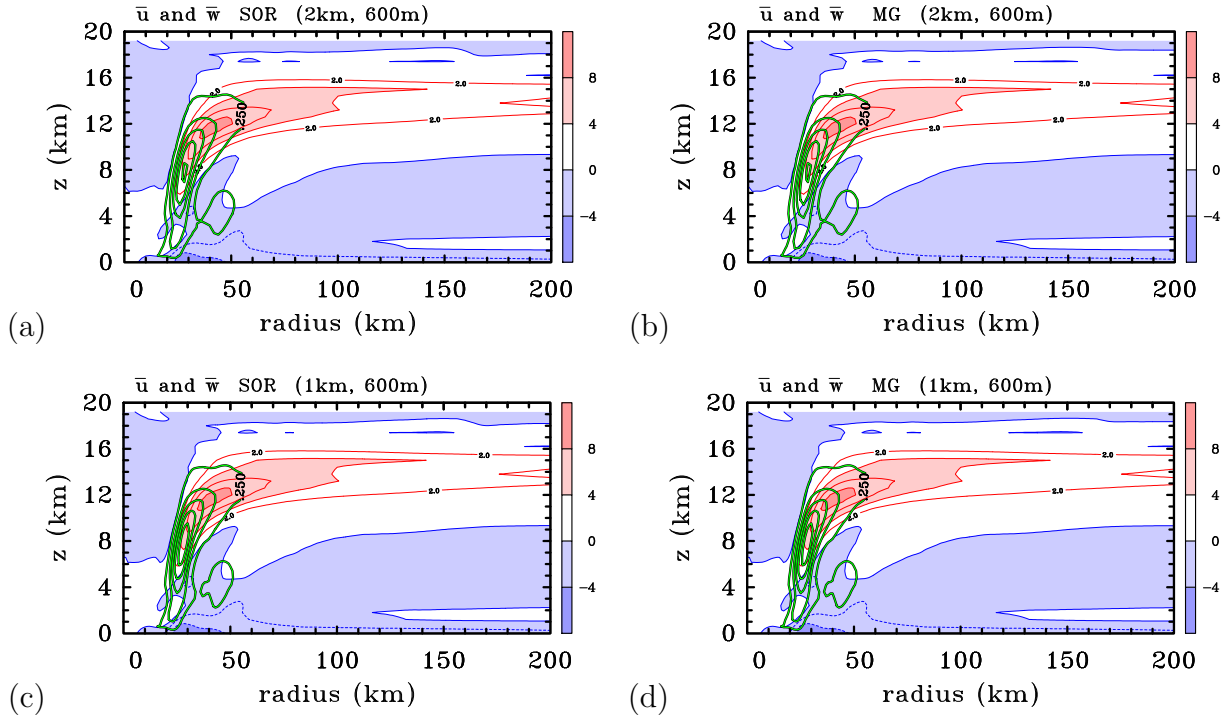


Figure 5.9: Axisymmetric balanced solutions for the radial (\bar{u}) and vertical (\bar{w}) components of the secondary circulation in a subset of Calc-D (idealized vortex, generalized diabatic heating (K per hour) and generalized tangential momentum forcing (m s^{-1} per hour)). The calculations differ in the method of solution (left columns SOR, right columns multigrid) and the radial and vertical grid spacing (dr, dz): (a) and (b) $dr = 2$ km, $dz = 600$ m; (c) and (d) $dr = 1$ km, $dz = 600$ m. Contour interval for \bar{u} : 2 m s^{-1} when $\bar{u} > 0$, 1 m s^{-1} when $\bar{u} < 0$. Positive contours solid, negative contours dashed. Shading values indicated on color bar. Green thick contours are shown for \bar{w} : 0.25 m s^{-1} (Only positive values are shown).

Calc-D	method	outflow		inflow	
$dr = 2$ km, $dz = 600$ m	SOR MG	8.8	8.8 m/s	-5.1	-5.1 m/s
$dr = 1$ km, $dz = 600$ m	SOR MG	8.9	8.9 m/s	-5.2	-5.2 m/s
$dr = 2$ km, $dz = 300$ m	SOR MG	9.3	9.3 m/s	-5.5	-5.5 m/s
$dr = 1$ km, $dz = 300$ m	SOR MG	9.4	9.3 m/s	-5.6	-5.5 m/s
$dr = 2$ km, $dz = 150$ m	SOR MG	9.4	9.4 m/s	-5.8	-5.8 m/s
$dr = 1$ km, $dz = 150$ m	SOR MG	9.5	9.5 m/s	-5.9	-5.9 m/s

Table 5.9: Maximum values of upper-level inflow and outflow for each case in Calc-D.

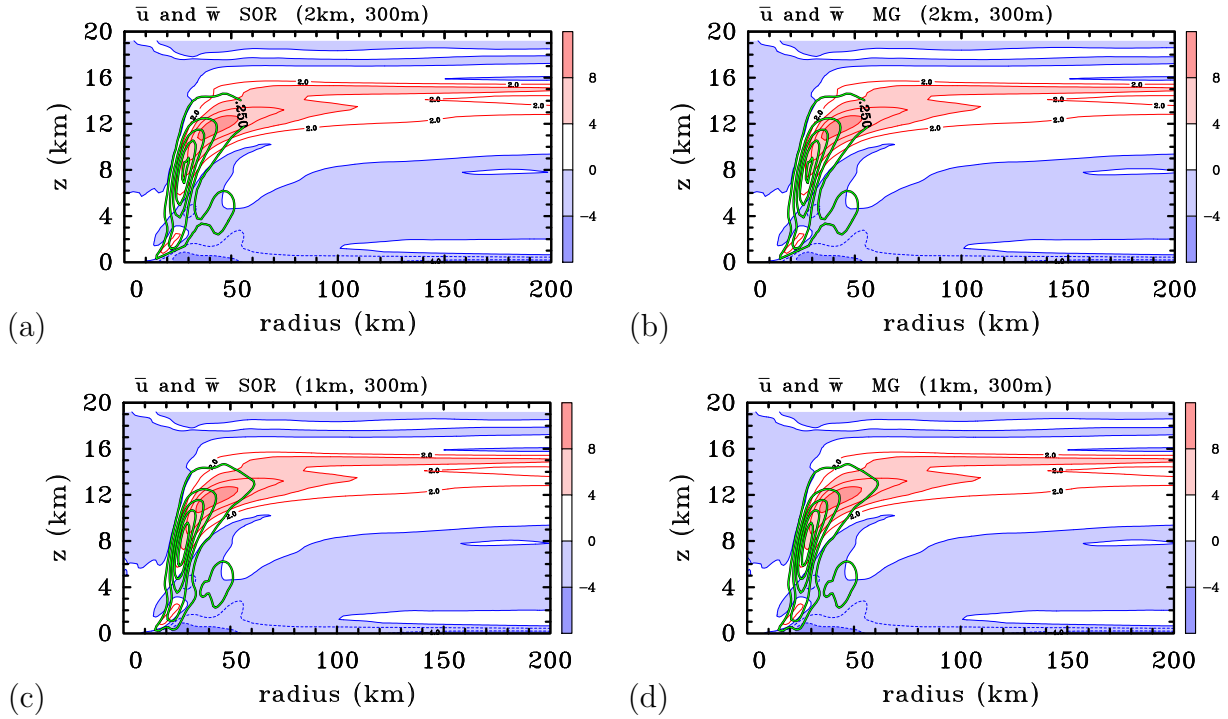


Figure 5.10: Axisymmetric balanced solutions for the radial (\bar{u}) and vertical (\bar{w}) components of the secondary circulation in a subset of Calc-D (idealized vortex, generalized diabatic heating (K per hour) and generalized tangential momentum forcing (m s^{-1} per hour)). The calculations differ in the method of solution (left columns SOR, right columns multigrid) and the radial and vertical grid spacing (dr, dz): (a) and (b) $dr = 2 \text{ km}$, $dz = 300 \text{ m}$; (c) and (d) $dr = 1 \text{ km}$, $dz = 300 \text{ m}$. Contour interval for \bar{u} : 2 m s^{-1} when $\bar{u} > 0$, 1 m s^{-1} when $\bar{u} < 0$. Positive contours solid, negative contours dashed. Shading values indicated on color bar. Green thick contours are shown for \bar{w} : 0.25 m s^{-1} (Only positive values are shown).

5.3.5 Summary of the calculations

Taken together, the four sets of calculations described above indicate that the ability to obtain a convergent solution of the Sawyer-Eliassen equation for the balanced secondary circulation of a high-resolution simulated tropical cyclone is severely compromised by the presence of regions where the azimuthal flow is inertially and/or symmetrically unstable. Such regions are predominantly found in the upper troposphere (see Figure 5.4). By severely compromised, we mean that it is no longer possible to obtain a convergent solution at a resolution commensurate with that of the simulation. In these situations, it is possible to obtain a convergent solution only by coarsening the grid, which serves to shrink the region of instability. With this coarsening, the solutions obtained by the SOR and multigrid methods are essentially the same, but in the calculations carried out here, the multigrid method is capable of obtaining a convergent solution with a smaller radial and/or

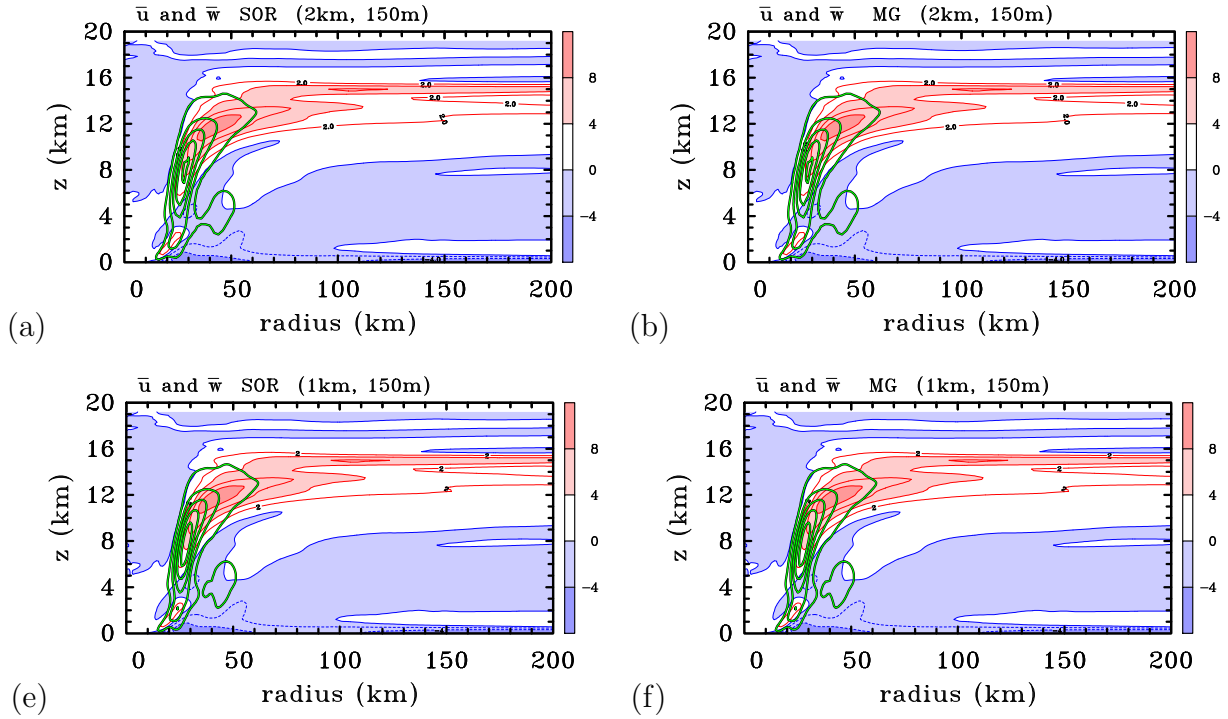


Figure 5.11: Axisymmetric balanced solutions for the radial (\bar{u}) and vertical (\bar{w}) components of the secondary circulation in a subset of Calc-D (idealized vortex, generalized diabatic heating (K per hour) and generalized tangential momentum forcing (m s^{-1} per hour)). The calculations differ in the method of solution (left columns SOR, right columns multigrid) and the radial and vertical grid spacing (dr, dz): (a) and (b) $dr = 2 \text{ km}$, $dz = 150 \text{ m}$; (c) and (d) $dr = 1 \text{ km}$, $dz = 150 \text{ m}$. Contour interval for \bar{u} : 2 m s^{-1} when $\bar{u} > 0$, 1 m s^{-1} when $\bar{u} < 0$. Positive contours solid, negative contours dashed. Shading values indicated on color bar. Green thick contours are shown for \bar{w} : 0.25 m s^{-1} (Only positive values are shown).

vertical grid spacing than the SOR method, before it too fails to converge.

Comparison between the two sets of calculations Calc-C and Calc-D suggest that the inflow layer just beneath the upper-level outflow layer in any balance solution is a consequence of the regularization that is required in Calc-C, but not in Calc-D. Because regularization is an *ad hoc* procedure, this result calls for caution in attributing such inflow layers to a balanced flow response driven by the distribution of diabatic heating and tangential momentum forcing.

The subset of calculations Calc-B that converge affirm prior work of Bui et al. (2009), Abarca and Montgomery (2014) and Montgomery and Persing (2020) in that the boundary layer inflow in the strict axisymmetric Sawyer-Eliassen balance model is far too weak (by a factor of about 3) compared to the simulated inflow in the inner-core region of the vortex. It follows that the Sawyer-Eliassen balance model is unable to represent the nonlinear boundary layer spin up mechanism that is essential for properly capturing the

intensification of the maximum tangential wind of an intensifying tropical cyclone when realistic sub grid scale diffusivities are employed consistent with current observational knowledge. These results are further evidence to refute the claim by Heng et al. 2017, Heng et al. 2018 that the balance dynamics is sufficient to capture the secondary circulation of an intensifying tropical cyclone, including the boundary layer.

5.4 Discussion

In this chapter, I investigated a potential balance explanation of upper tropospheric inflow jets. The result shows the explanation for the inflow layers in terms of axisymmetric balance dynamics is problematic. I have compared two solution methods, the SOR-method and a multi-grid method, to solve the Sawyer-Eliassen equation for the balanced secondary circulation of a tropical cyclone vortex to a particular forcing distribution of diabatic heating and tangential momentum forcing. These solutions affirm prior findings concerning the need to coarsen the data from high-resolution numerical simulations in the presence of inertial or symmetric instability when applied to determine the corresponding balanced secondary circulation. They show also that the multi-grid method is able to obtain a convergent solution with a finer grid spacing than the SOR method, although it too fails when the grid spacing is too small. When both methods converge *and the vortex is symmetrically stable*, the solutions are broadly similar.

All results suggest that the inflow layer just beneath the upper-level outflow layer in a balance flow solution of the Sawyer-Eliassen equation corresponding to a typical tropical cyclone simulation is a consequence of the need to regularize this equation in regions of inertial and/or symmetric instability. Because regularization is an *ad hoc* procedure, this inference calls for caution in attributing such inflow layers to a balanced flow response driven by the distribution of diabatic heating and tangential momentum forcing. Thus, an explanation of the upper-level inflow layers that are found in numerical simulations of tropical cyclones needs to be based on more fundamental considerations than assuming global thermal wind balance.

Chapter 6

Explanations for upper inflows

At an early stage of my study, a possible explanation for the inflow layers seemed to be an extension of the result of Shapiro and Willoughby (1982) that, if the tangential flow is in thermal wind balance, the response of the secondary circulation to a point source of positive tangential momentum is an outward flow through the source and a compensating inward flow above and below it. Such an explanation is explored in Chapter 4, where it is shown to be problematic.

As far as I am aware, a satisfactory explanation for these layers and their possible significance for the storm, itself, has not been provided. Zhang and Chen (2012) and Chen and Zhang (2013) drew attention to the inflow layer above the upper-tropospheric outflow layer, attributing this layer to the detrainment of deep “convective bursts” in the developing eyewall region. However, these studies fell short of investigating the forces responsible for the inflow layer (an appraisal of these papers was provided by Smith and Montgomery 2015).

Referring to the results of Bu et al. (2014) and Fovell et al. (2016), Duran and Molinari (2019) inferred that cloud-top cooling modifies the circulation near the cloud top, driving a weak inflow above the cooling maximum and outflow below, along with subsidence within the region of cooling. However, this is at best a partial explanation because a change in radial flow requires a net force field in the radial direction, the origin and nature of which were not discussed.

A recent analysis of the mean and eddy contributions to tropical cyclone spin up in an idealized, high-resolution, numerical simulation of tropical cyclone intensification by Montgomery et al. (2020) pointed to an alternative explanation for the upper tropospheric inflow layers. They suggested that these layers are primarily a result of a negative agradient force field that develops in the upper troposphere, apparently as a response to the outflow itself. As their study was focussed largely on the vortex spin up at low levels and in the eyewall, the vertical resolution of the model was largest in the boundary layer. The present Chapter focusses on the evolution and three-dimensional structure of the upper tropospheric inflow layers using a modified version of the model used by Montgomery et al. (described in Chapter 2) with increased vertical resolution in the upper troposphere and reduced vertical resolution at low levels. In addition, because it concentrates on the

upper troposphere, the new simulation includes a representation of cloud microphysics, unlike that of Montgomery et al..

The radial velocity tendency equation is presented in section 6.1. Section 6.2 shows the radial velocity tendency analysis and offers an explanation of upper inflow layers, while Section 6.3 shows diagnostics of normalized agradient force, a measure of the degree of imbalance in the numerical simulation. Section 6.4 shows the azimuth-height structure. The conclusions are presented in section 6.5.

6.1 The radial velocity tendency equation

As a starting point to understanding the origin of the layers of inflow sandwiching the upper-level outflow, I carry out an analysis of the azimuthally-averaged radial momentum equation in the cylindrical coordinate system (r, λ, z) , which can be written as the following form:

$$\begin{aligned}
 \frac{\partial \bar{u}}{\partial t} + \underbrace{\bar{u} \frac{\partial \bar{u}}{\partial r}}_{U_{mr}} + \underbrace{\left(\overline{u' \frac{\partial u'}{\partial r}} + \frac{v'}{r} \overline{\frac{\partial u'}{\partial \lambda}} \right)}_{U_{eh}} &= \underbrace{-\bar{w} \frac{\partial \bar{u}}{\partial z}}_{U_{mv}} - \underbrace{\overline{w' \frac{\partial u'}{\partial z}}}_{U_{ev}} \\
 &+ \underbrace{\frac{\bar{v}^2}{r} + f \bar{v} - \frac{1}{\bar{\rho}} \frac{\partial \bar{p}}{\partial r}}_{U_{magf}} + \underbrace{\frac{\overline{v'^2}}{r} - \frac{1}{\bar{\rho}} \frac{\partial \bar{p}'}{\partial r}}_{U_{eagf}} \\
 &+ \underbrace{\frac{1}{r \bar{\rho}} \frac{\partial r \bar{\rho} \overline{\tau_{rr}}}{\partial r} - \frac{\overline{\tau_{\lambda\lambda}}}{r}}_{U_{dh}} + \underbrace{\frac{1}{\bar{\rho}} \frac{\partial \bar{\rho} \overline{\tau_{rz}}}{\partial z}}_{U_{dv}}, \tag{6.1}
 \end{aligned}$$

where, for any quantity α , $\alpha' = \alpha - \bar{\alpha}$ denotes a departure from the azimuthal mean, or eddy component, t is the time, u, v, w are the radial, tangential and vertical components of velocity. ρ is the density, p is the pressure, f is the Coriolis parameter, ζ is the vertical component of relative vorticity, and the stress tensors τ_{rr} , $\tau_{\lambda\lambda}$ and τ_{rz} , generalized to account for anisotropic eddy momentum diffusivities for the subgrid scale motions can be calculated from:

$$\overline{\tau_{rr}} = \overline{2K_{m,h} \left(\frac{\partial u}{\partial r} \right)}, \tag{6.2}$$

$$\overline{\tau_{\lambda\lambda}} = \overline{2K_{m,h} \left(\frac{1}{r} \frac{\partial v}{\partial \lambda} + \frac{u}{r} \right)}, \tag{6.3}$$

$$\overline{\tau_{rz}} = \overline{K_{m,v} \left(\frac{\partial w}{\partial r} + \frac{\partial u}{\partial z} \right)}. \tag{6.4}$$

See e.g., Landau and Lifshitz (1966, p51). Here $K_{m,h}$ and $K_{m,v}$ are the horizontal and vertical diffusivities of horizontal momentum.

To facilitate interpretation, here choosing this pseudo-Lagrangian form in which the left-hand-side represents the material acceleration in the radial direction following the horizontal wind. The reason for this choice is to provide a layer-wise perspective of the inflow and outflow layers. The individual terms on this side represent: the local tendency of the mean radial velocity, the mean radial advection of radial momentum per unit mass, U_{mr} , and the mean horizontal advection of eddy radial momentum per unit mass, U_{eh} . The terms on the right-hand-side of the equation are in order: U_{mv} is minus the mean vertical advection of mean radial momentum per unit mass and U_{ev} is minus the eddy vertical advection of eddy radial momentum per unit mass; U_{magf} and U_{eagf} are the mean and eddy agradiant force per unit mass, respectively; U_{dh} is the mean horizontal diffusive tendency of radial momentum while U_{dv} is the vertical diffusive tendency.

6.2 Radial velocity tendency analysis

Figure 6.1 shows radius-height cross sections of the mean radial advection of radial momentum per unit mass, U_{mr} (left column), and the mean horizontal advection of eddy radial momentum per unit mass, U_{eh} (right column), in the azimuthally-averaged and one-hour time-averaged radial momentum equation centred at 42 h, 60 h and 74 h. In all U_{mr} fields, there is a shallow layer of negative values beyond a radius of about 25–35 km and a layer of positive values within such radius at the surface. For all left panels, the boundary layer inflow accelerates inwards and then decelerates to the centre. Shallow sloping layers of alternating positive and negative values of U_{mr} are above the boundary layer inflow. These layers are generally confined within a radius of about 40 km and a height of about 4 km. The lowermost layer of positive values coincides with the radii where the inflow is decelerated sharply before ascending into the eyewall. This structure becomes more obvious as the tropical cyclone strength increases by time.

In the upper troposphere, the radial flow accelerates outwards as the air exits the eyewall. At 42 h (Figure 6.1(a)), the outward acceleration region occurs in a small area at about 12 km to 15 km in height and 20 km to 60 km in radii. Beyond approximately 60 km radius, the mean acceleration in the upper troposphere is inwards so that outward flowing air is being decelerated. At 60 h (Figure 6.1(c)), the outward acceleration area extends to about 80 km while also down to the middle troposphere. The inward acceleration region is much stronger than at 42 h, and appears next to the bottom right direction of the outward acceleration region. A similar, but stronger structure is found at 74 h (Figure 6.1(e)), because of the complex structure in the root of the upper inflow layer, more detailed alternating positive and negative values distribution is shown.

The right column of Figure 6.1 shows the mean horizontal advection of eddy radial momentum per unit mass, U_{eh} . In general, U_{eh} is positive inside the eyewall and negative outside. Particularly at 74 h (Figure 6.1(f)), an extra negative range is sandwiched between the positive ranges from 1 km to 10 km in height.

Figure 6.2 shows radius-height cross sections of minus the mean vertical advection of mean radial momentum per unit mass, U_{mv} (left column) and minus the eddy vertical

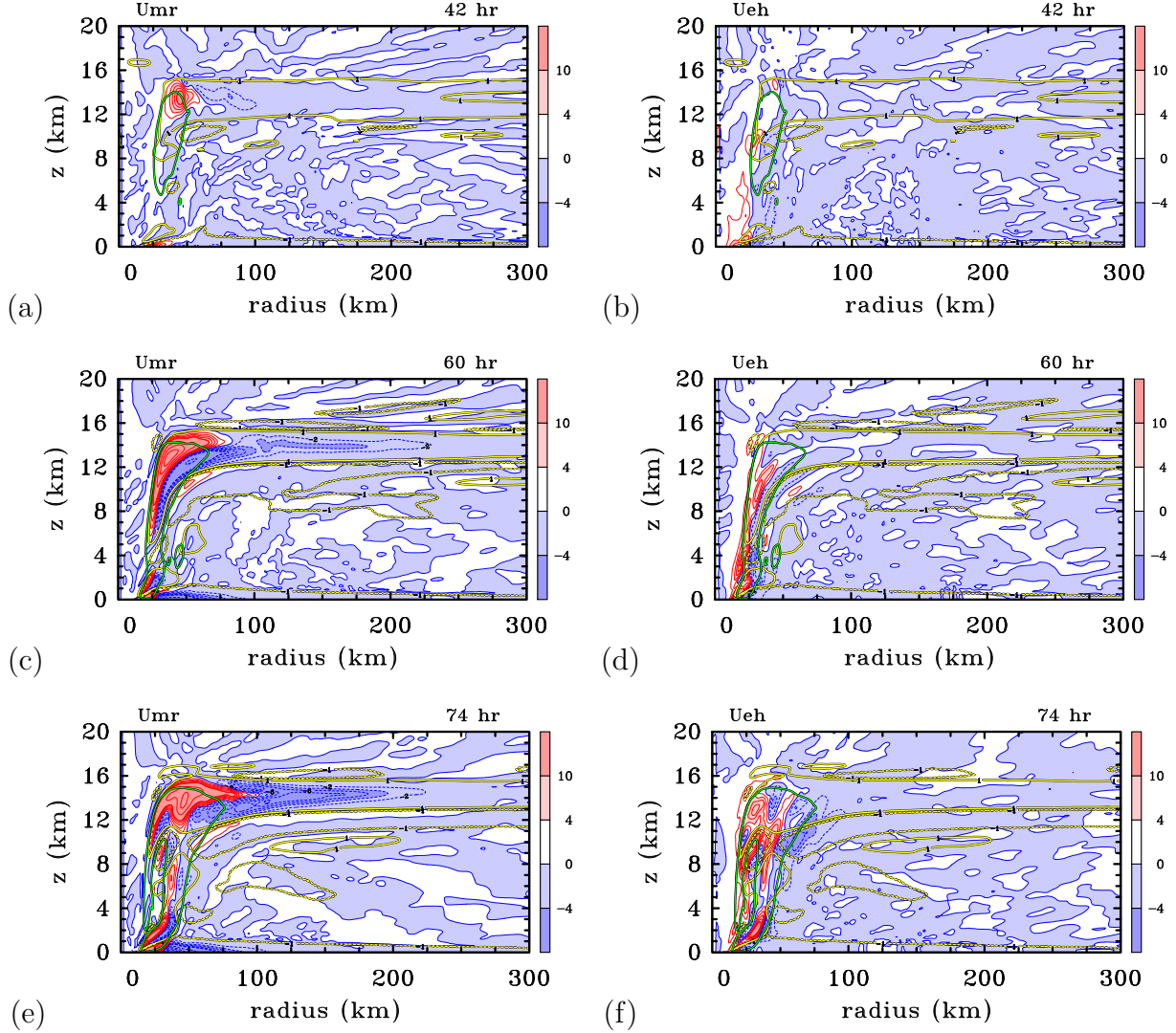


Figure 6.1: Radius-height cross sections of the main terms in the azimuthally-averaged radial momentum equation (Equation 6.1) with two contours of the azimuthally-averaged radial velocity component, \bar{u} , superimposed: (a), (c), (e) the mean radial advection of radial momentum per unit mass, U_{mr} ; (b), (d), (f) the mean horizontal advection of eddy radial momentum per unit mass, U_{eh} ; at 42 h (top row), 60 h (middle row) and 74 h (bottom row). All fields are time-averaged for one hour. Contour interval for terms in the momentum equation, $2 \text{ m s}^{-1} \text{ h}^{-1}$ for values from 0 to $\pm 10 \text{ m s}^{-1} \text{ h}^{-1}$ and $10 \text{ m s}^{-1} \text{ h}^{-1}$ for values higher in magnitude (red solid contours for positive values, blue dashed contours for negative value, shading as on colour bar in $\text{m s}^{-1} \text{ h}^{-1}$). Contours of \bar{u} : solid yellow contour with black border for 1 m s^{-1} , dashed yellow contour with black border for -1 m s^{-1} .

advection of eddy radial momentum per unit mass, U_{ev} (right column) in the azimuthally-averaged and one-hour time-averaged radial momentum equation centred at 42 h, 60 h

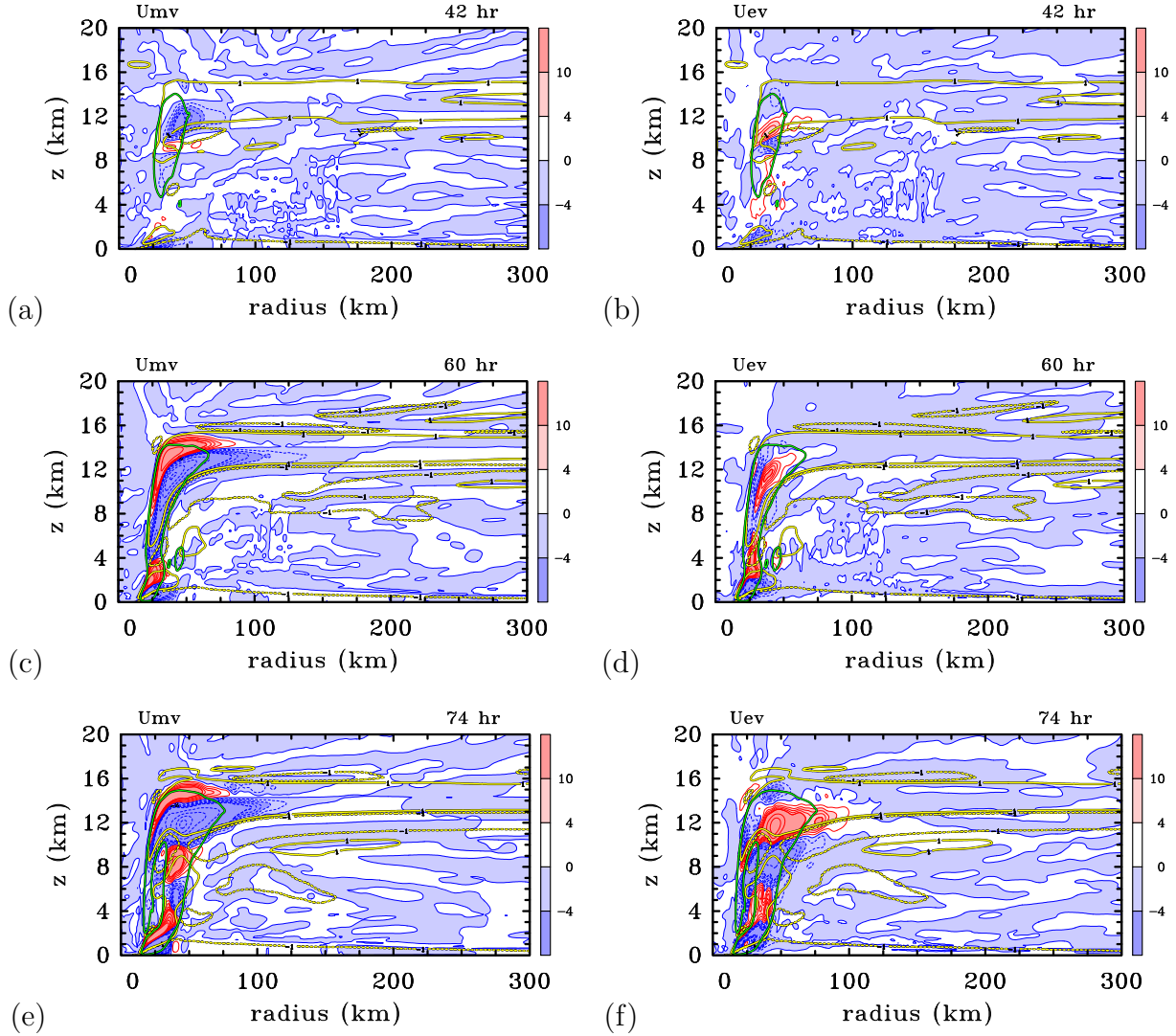


Figure 6.2: Radius-height cross sections of the main terms in the azimuthally-averaged radial momentum equation (Equation 6.1) with two contours of the azimuthally-averaged radial velocity component, \bar{u} , superimposed: (a), (c), (e) minus the mean vertical advection of mean radial momentum per unit mass, U_{mv} ; (b), (d), (f) minus the eddy vertical advection of eddy radial momentum per unit mass, U_{ev} ; at 42 h (top row), 60 h (middle row) and 74 h (bottom row). All fields are time-averaged for one hour. Contour interval for terms in the momentum equation, $2 \text{ m s}^{-1} \text{ h}^{-1}$ for values from 0 to $\pm 10 \text{ m s}^{-1} \text{ h}^{-1}$ and $10 \text{ m s}^{-1} \text{ h}^{-1}$ for values higher in magnitude (red solid contours for positive values, blue dashed contours for negative value, shading as on colour bar in $\text{m s}^{-1} \text{ h}^{-1}$). Contours of \bar{u} : solid yellow contour with black border for 1 m s^{-1} , dashed yellow contour with black border for -1 m s^{-1} .

and 74 h. The radius-height structure of U_{mv} in the left column of Figure 6.2 shows a series of layers in which U_{mv} has an alternating sign. At 42 h (Figure 6.2 (a)), there are

two relatively strong negative value regions at the base of the boundary layer inflow and the base of the upper-tropospheric outflow. In the lowest layer, $U_{mv} < 0$, indicating a contribution to an increase of the radial inflow by the vertical advection of inward radial momentum from near the surface. The negative U_{mv} which above 8 km represents the upward transport of mean inward radial momentum from the inflow layer just below the mean outflow layer.

At 60 h and 74 h (Figure 6.2 (c) and (e)), due to the development of eyewall updraft, the upward advection of both inward and outward radial momentum become more significantly. The enhancement of the original negative U_{mv} regions, which already existed at 42 h, shows a stronger upward transport of inward radial momentum. In the sloping layer above the boundary layer, $U_{mv} > 0$, reflecting the mean vertical transport of positive radial momentum associated with the strong outflow of air just above the boundary layer. The layer of negative U_{mv} between about 4 and 8 km height is associated with the upward transport of mean radial inflow in the eyewall updraught from the lower troposphere. The layered pattern of U_{mv} above about 8 km is consistent also with the layered pattern of inflow and outflow in the upper troposphere together with that of vertical velocity. The downward transport of inward radial momentum from the inflow layer just above the mean outflow layer contributes to the layer of negative tendency at about 15 km. The additional positive and negative U_{mv} regions at about 7 km to 10 km at 74 h (Figure 6.2 (e)) are associated with a relative strong local outflow.

Figure 6.2 (b) (d) and (e) show minus the eddy vertical advection of eddy vertical momentum per unit mass, U_{ev} . The structure of U_{ev} exhibits a series of layers just like U_{mv} in which U_{ev} has an alternating sign. In the lower troposphere, the U_{ev} field broadly reinforces that of U_{mv} . In the upper troposphere, there is a degree of cancellation between U_{mv} and U_{ev} , which implies that the eddies are acting to transport radial momentum against the mean gradient in this layer, i.e. they are counter-gradient. These features are consistent with the upper-level pattern of the vertical eddy momentum flux shown in Persing et al. (2013; Figure 15(e)) and contribute to a strengthening of the primary outflow layer, itself, as well as the inflow layer below the outflow layer.

Figure 6.3 shows radius-height cross sections of the mean and eddy gradient force per unit mass, U_{magf} and U_{eagf} respectively, in the azimuthally-averaged and one-hour time-averaged radial momentum equation centred at 42 h (top), 60 h (middle) and 74 h (bottom). The fields are overlain with the azimuthally- and time-averaged radial velocity. Panel (a), (c) and (e) show the mean gradient force field, U_{magf} , which characterizes the degree of gradient wind imbalance, at 42 h 60 h and 74 h, respectively. Prominent features of this field at these times include:

- a shallow layer of strong subgradient force ($U_{magf} < 0$) beyond a radius of 20 km near the surface. This layer corresponds with the frictional boundary layer in which the negative force imbalance drives a strong, surface-based inflow (Figure 3.1);
- a deeper region of supergradient force ($U_{magf} > 0$) immediately inside this radius and extending above the shallow subgradient force region. This force serves to de-

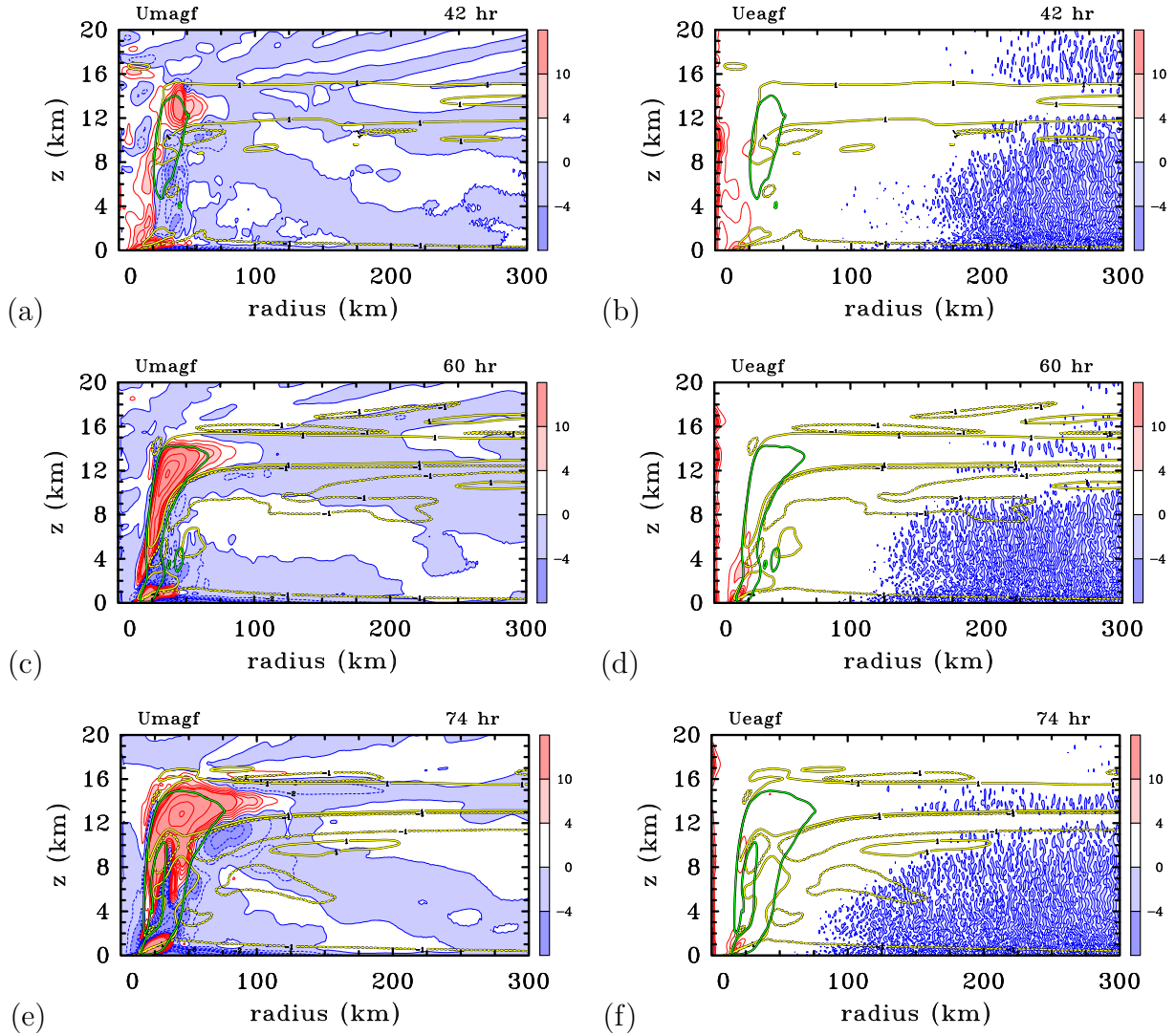


Figure 6.3: Radius-height cross sections of the main terms in the azimuthally-averaged radial momentum equation (Equation 6.1) with two contours of the azimuthally-averaged radial velocity component, \bar{u} , superimposed: (a), (c), (e) the mean gradient force per unit mass, U_{magf} ; (b), (d), (f) the eddy gradient force per unit mass, U_{eagf} ; at 42 h (top row), 60 h (middle row) and 74 h (bottom row). All fields are time-averaged for one hour. Contour interval for terms in the momentum equation, $2 \text{ m s}^{-1} \text{ h}^{-1}$ for values from 0 to $\pm 10 \text{ m s}^{-1} \text{ h}^{-1}$ and $10 \text{ m s}^{-1} \text{ h}^{-1}$ for values higher in magnitude (red solid contours for positive values, blue dashed contours for negative value, shading as on colour bar in $\text{m s}^{-1} \text{ h}^{-1}$). Contours of \bar{u} : solid yellow contour with black border for 1 m s^{-1} , dashed yellow contour with black border for -1 m s^{-1} .

celerate the boundary layer inflow and accelerate outflow just above the inflow layer as the air ascends into the eyewall;

- a region of subgradient force through the lower troposphere extending to the outer radius. This force accelerates air inwards towards the eyewall and accounts for the spin up of the tangential winds above the boundary layer outside the developing eyewall (radii > 50 km).
- at 60 h (Figure 6.3 (c)) and 74 h (Figure 6.3 (e)), there is a tower of supergradient force within the outward-sloping eyewall updraught from about 2 km to 15 km in height. In this region, air with high tangential momentum generated in the boundary-layer inflow is lofted into the eyewall updraught. This lofting is sufficiently strong that the sum of the centrifugal and Coriolis forces exceed the inward radial pressure gradient force per unit mass as air parcels ascend. In turn, the outward force drive these air parcels outwards as they ascend. At 42 h (Figure 6.3 (a)), this structure has not yet become established.

From about 13 km to 15 km, the region of strong positive $Umagf$ extends to a radius of about 75 km at 42 h, 100 km at 60 h and 125 km at 74 h. This force is the main outward force accelerating the upper-level outflow. As air parcels move outwards in this region while approximately conserving their absolute angular momentum, their tangential velocity diminishes. Eventually, the inward-directed pressure gradient force present at this level finally gains the upper hand and the sign of $Umagf$ reverses. This sign change of $Umagf$ is to be expected since mass continuity requires the outflowing air parcels to decelerate as the flow spreads out. Invoking Newton’s second law of motion, the only way that air parcels can decelerate radially is if they experience a negative radial force. Recall that in fluid flows, the pressure force *is determined as part of the solution* and is constrained *globally* by the boundary conditions on the flow as well as the need to satisfy mass continuity and Newton’s second law of motion.

An equivalent way to think about the outflow layer is to consider it as an expanding jet of air emanating from a radial momentum source where the eyewall convection terminates (Ooyama 1987). The outward expansion is resisted by an induced radially-inward pressure gradient force (recall that the centrifugal force is always positive and the Coriolis force in the radial direction is positive as long as the tangential flow remains cyclonic). Because the induced pressure field extends beyond just the outflow layer itself, one can expect a flow response laterally beyond the outflow layer as well. In confirmation of this idea, Figure 6.3 (c) shows that $Umagf$ is mostly inward beyond a radius of 100 km (beyond 75 km in panel (a) and beyond 125 km in panel (e)), not only in the outflow layer, itself, but over a significant depth above and below it, especially below. Where this inward force persists, it will act to accelerate air parcels inwards.

The foregoing interpretation appears to be different from that proposed by Komaromi and Doyle (2017) to explain this inflow above the outflow layer, which they believe “to be associated with a “reverse” secondary circulation pattern, associated with dry-adiabatic descent above the eye in the lower stratosphere”. It is unclear whether the “belief” rests on balance ideas, whether it invokes an unbalanced argument in which descent in the eye “sucks air inwards” above the tropopause, or whether it is pure speculation.

From a balance dynamics perspective, the proffered explanation seems unlikely because the subsiding air on the inside of the eyewall updraught would be explained as a result of the diabatic heating in the eyewall itself (Schubert et al. 2007). The balance response to this heating would be limited by the local Rossby scale, which for a fully developed tropical cyclone vortex in the eyewall is on the order of 60 km (Shapiro and Montgomery 1993). Therefore, the idea of the upper-level inflow, which extends beyond 300 km at the later times shown, being a balanced consequence of the diabatic heating in the upper eyewall cloud seems implausible to me.

From a more general perspective not limited to balance, since the pressure field is connected globally by the requirement that the mass continuity equation is globally satisfied and since the vortex is a tightly coupled system through the pressure field, it is clear that if air is being funneled towards the eye just above the tropopause it must either ascend or descend in the central region. The high static stability in the stratosphere would overwhelmingly favour descent into the eye and, from an unapproximated, unbalanced perspective, according to Newton's second law, the pressure field would have to adjust to drive this descent, even though the flow adjustment may take place as a nearly balanced response. In this view, whether one argues that the eye "sucks air inwards" or that the flow in the upper inflow layer is driven by the inward agradient force may be a matter of semantics.

In developing the foregoing interpretation for the emergence and persistence of the upper-level inflow layers that straddle the main outflow layer, we have noted that the solution for the upper troposphere region is highly variable in both time and azimuth. This behaviour is a result of inertia gravity waves that are generated by transient deep convection. Consequently, the persistence of this underlying forcing structure tends to be obscured in individual snapshots of the flow and only becomes evident after time averaging on the scale of an hour or two. The effects of inertia-gravity wave fluctuations in the outflow upper level outflow and inflow layers as well as the outflow just above where the inflowing boundary layer inflow terminates are evident as fluctuations in the radial wind component in Figure 3.1.

The right colmun of Figure 6.3 shows the eddy agradient force field, U_{eagf} , which indicates that the asymmetric part of the tangential flow is not in gradient wind balance. This eddy term contributes to a positive radial acceleration throughout the troposphere within 100 km radius (about 75 km at 74 h), where it represents an additional centrifuge effect to that of the mean term U_{magf} . In particular, U_{eagf} shows strong positive values near the surface at radii between approximately 10 and 20 km near where the surface inflow terminates, reinforcing the deceleration of the boundary layer inflow. The relatively large values of U_{eagf} near the axis should not be taken too seriously and are presumably due to numerical inaccuracy arising from the appreciable numerical discretization error and centre location error.

Figures 6.4 shows the sub-grid-scale diffusive tendencies of radial momentum, U_{dh} and U_{dz} , in the azimuthally-averaged and one-hour time-averaged radial momentum equation centred at 42 h (top), 60 h (middle) and 74 h (bottom). At 42 h, values of both terms are small. At 60 h and 74 h, the horizontal diffusion of radial momentum (U_{dh}) is relatively

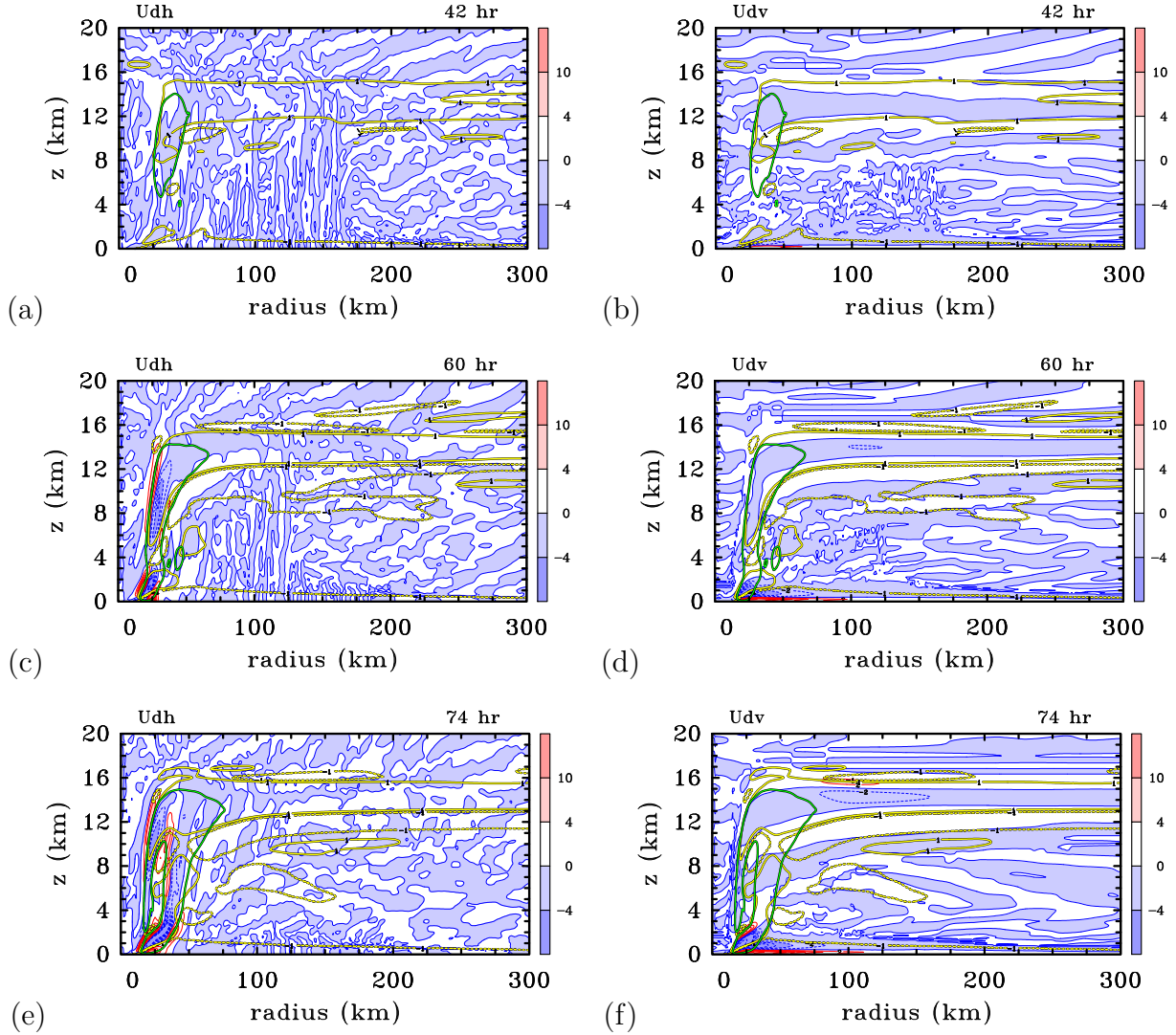


Figure 6.4: Radius-height cross sections of the main terms in the azimuthally-averaged radial momentum equation (Equation 6.1) with two contours of the azimuthally-averaged radial velocity component, \bar{u} , superimposed: (a), (c), (e) the mean radial diffusive tendency of radial momentum, U_{dh} ; (b), (d), (f) the mean vertical diffusive tendency of radial momentum, U_{dv} ; at 42 h (top row), 60 h (middle row) and 74 h (bottom row). All fields are time-averaged for one hour. Contour interval for terms in the momentum equation, $2 \text{ m s}^{-1} \text{ h}^{-1}$ for values from 0 to $\pm 10 \text{ m s}^{-1} \text{ h}^{-1}$ and $10 \text{ m s}^{-1} \text{ h}^{-1}$ for values higher in magnitude (red solid contours for positive values, blue dashed contours for negative value, shading as on colour bar in $\text{m s}^{-1} \text{ h}^{-1}$). Contours of \bar{u} : solid yellow contour with black border for 1 m s^{-1} , dashed yellow contour with black border for -1 m s^{-1} .

small except in the region where the radial flow terminates and turns up into the eyewall and the inner part of the eye wall from about 6 km to 12 km height. The vertical diffusion of radial momentum (U_{dh}) shows a very shallow layer of strong positive tendency beyond a

radius of about 20 km, which is a manifestation of surface friction slowing down the inflow. Above this layer lies a somewhat thicker layer of negative tendency, which is associated with the vertical diffusion of inward radial momentum through the inflow layer. This diffusion becomes particularly strong near where the boundary layer inflow terminates.

The essence of the radial momentum budget is encapsulated in Figure 6.5. These show the sum of the time-averaged and azimuthally-averaged tendencies on each side of Equation 6.1 at 42 h, 60 h and 74 h. Panels (a) (c) and (e) shows the time-averaged pseudo-Lagrangian radial acceleration, while panels (b) (d) and (f) show the corresponding time-averaged net radial force leading to this acceleration. At all three times, there is generally good agreement between the pseudo-radial acceleration and the net forcing terms, especially in the upper troposphere. These comparisons provide confidence in the integrity of the calculations. In the lower troposphere, there are a few local discrepancies in detail between the acceleration and forcing terms. These are presumably associated with interpolation errors and the like (see Montgomery et al. 2020, section 4.2.1).

6.3 Diagnosis of imbalance

Since the magnitude of $Umagf$ is a measure of the degree of force imbalance in the radial direction, the fields shown in Figure 6.6 provide a context to assess the accuracy of the balance theory of tropical cyclones, in general, and thereby its applicability to explaining the upper-tropospheric inflow jets in particular.

In his review paper on the tropical cyclone inner core, Willoughby (1988) wrote “Although the wind may be supergradient where the boundary-layer inflow decelerates under the eyewall, the role of the imbalance in the secondary circulation has been exaggerated. (p186)” More recently, Heng et al. (2017) claimed that: “balanced dynamics can well capture the secondary circulation in the full-physics model simulation *even in the inner-core region in the boundary layer*”. These claims were called into question long ago by the analysis of a three-dimensional numerical simulation of Hurricane Andrew (1992) by Zhang et al. (2001), which showed significant imbalances in the boundary layer, just above it, and through much of the eyewall¹.

The simulation by Zhang et al. (2001) had a relatively coarse 6 km horizontal grid spacing by modern standards, compared with the 1 km used in the present simulations, and it was performed for a particular storm. In comparison, the idealized calculation presented here is carried out in a quiescent environment. For these reasons it is of interest to examine the extent to which Zhang et al.’s findings are generic. As a contribution to the debate on the accuracy of the balance approximation, as is shown in Figure 6.6 radius-height cross sections of $Umagf$ normalized by the local radial pressure gradient and expressed as a percentage: $Umagf/[(1/\bar{\rho})(\partial\bar{p}/\partial r)]$.

At all times shown (42 h, 60 h and 74 h), much of the upper troposphere shows significant force imbalance (magnitude of normalized $Umagf$ approaching 100% supergradient at the top of the eyewall and exceeding 50% subgradient in much of outer region of outflow).

¹These claims have been refuted more recently also by Montgomery and Persing (2020).

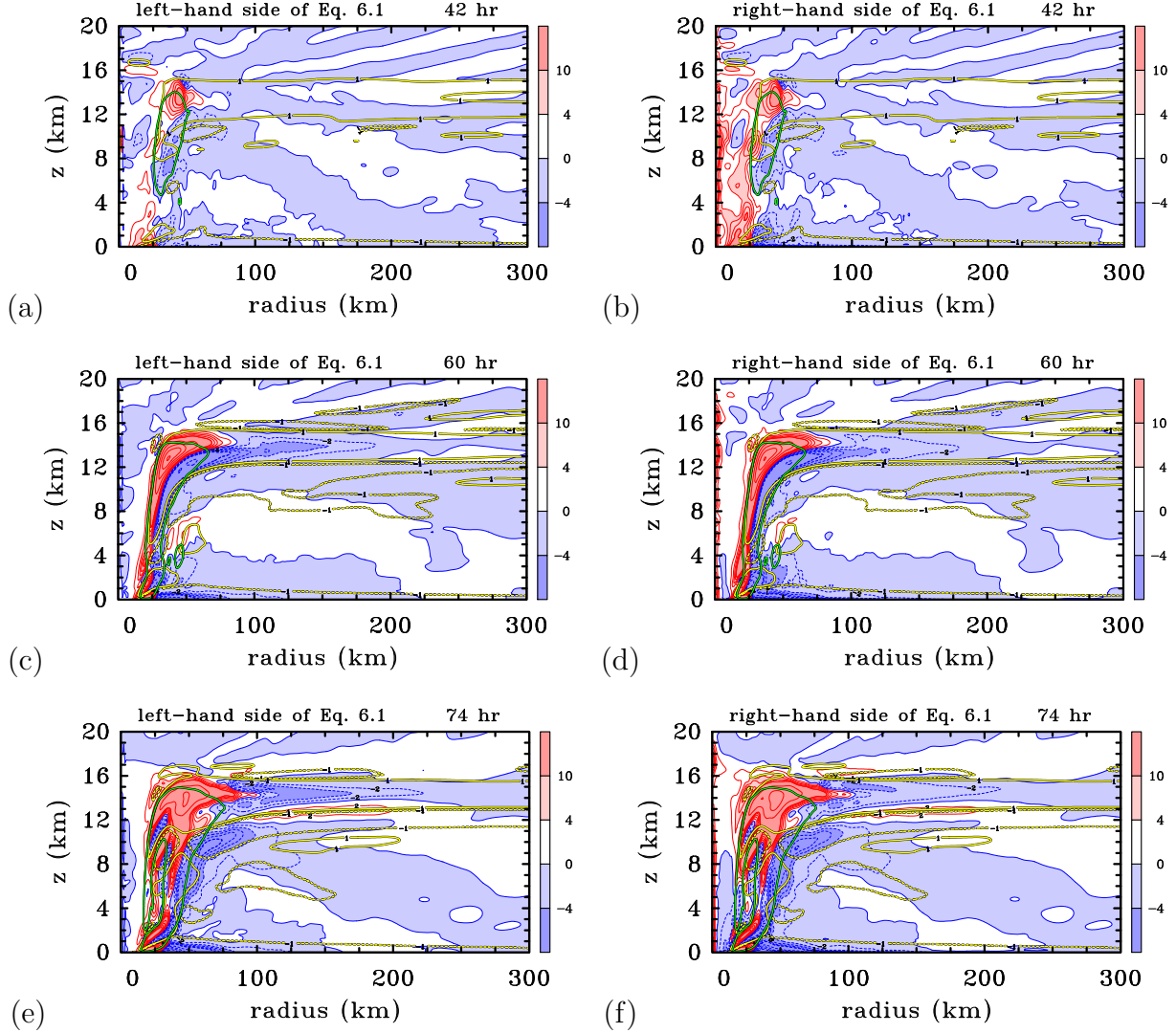


Figure 6.5: Radius-height cross sections of the main terms in the azimuthally-averaged radial momentum equation (Equation 6.1) with two contours of the azimuthally-averaged radial velocity component, \bar{u} , superimposed: (a), (c), (e) left-hand-side of Equation 6.1; (b), (d), (f) right-hand-side of Equation 6.1 at 42 h (top row), 60 h (middle row) and 74 h (bottom row). All fields are time-averaged for one hour. Contour interval for terms in the momentum equation, $2 \text{ m s}^{-1} \text{ h}^{-1}$ for values from 0 to $\pm 10 \text{ m s}^{-1} \text{ h}^{-1}$ and $10 \text{ m s}^{-1} \text{ h}^{-1}$ for values higher in magnitude (red solid contours for positive values, blue dashed contours for negative value, shading as on colour bar in $\text{m s}^{-1} \text{ h}^{-1}$). Contours of \bar{u} : solid yellow contour with black border for 1 m s^{-1} , dashed yellow contour with black border for -1 m s^{-1} .

At 60 h and 74 h, in the outer part of the frictional boundary layer (beyond about 25 km radius), the force imbalance is as much as 30% subgradient. At smaller radii and low levels near the base of the eyewall, the normalized imbalance exceeds 40% supergradient.

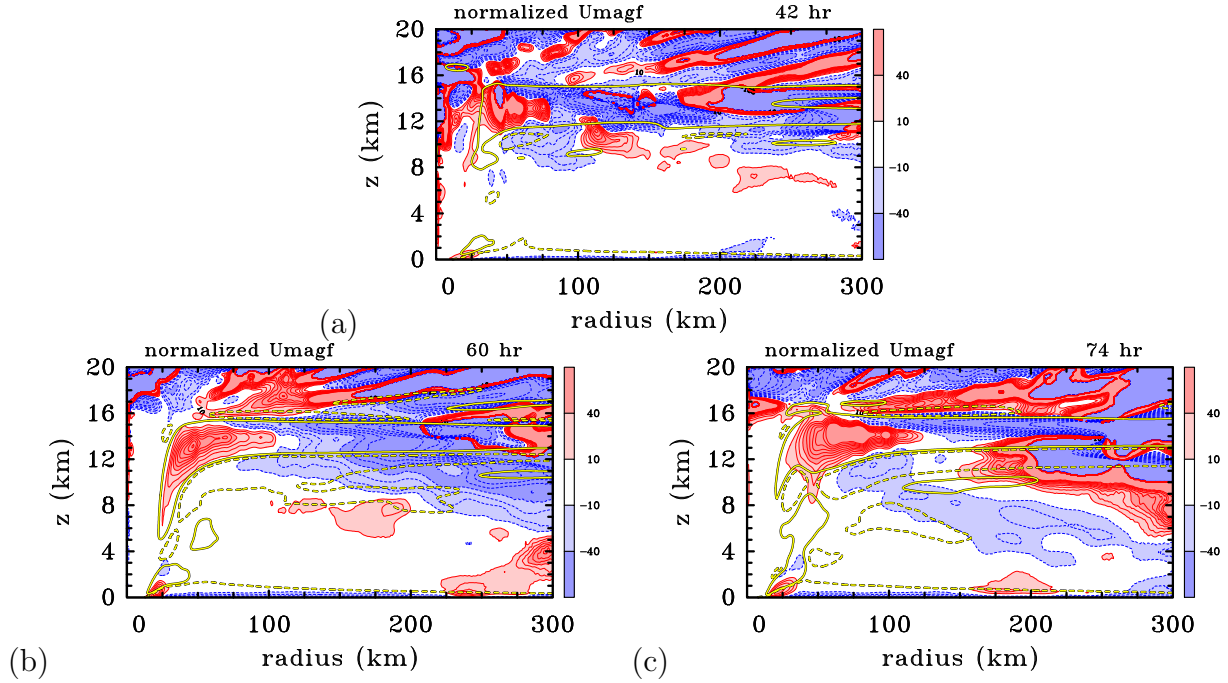


Figure 6.6: Radius-height cross sections of U_{magf} normalized by the by radial pressure gradient force with two contours of the azimuthal mean radial velocity component, \bar{u} , superimposed. Normalized U_{magf} shaded, solid red contours for positive values, blue dashed contours for negative values, contour interval 10 % from -100 % to 100 %, shading as colour bar in %. All fields are azimuthally-averaged and time-averaged for one hour. Contours of u : solid yellow contour with black border for 1 m s^{-1} , dashed yellow contour with black border for -1 m s^{-1} . Shading values on colour bar.

In contrast, much of the low to mid troposphere is balanced to within 10%, especially at 42 h and 60 h. These findings are broadly in line with those of Zhang et al., see Fig. 6d and related discussion, but they do highlight also a significant degree of relative imbalance characterized by significant values of normalized U_{magf} in the upper tropospheric outflow layer². One difference is that Zhang et al. did not find inflow layers, perhaps because the vertical resolution of their simulation was insufficient, or because of the presence of significant vertical wind shear.

6.4 Azimuth-height structure

Nevertheless, because the explanation given in section 6.2 is presented from an axisymmetric viewpoint, it is appropriate to consider its applicability in light of the low azimuthal wavenumber asymmetric structure of the inflow layers shown in Figures 3.7 and 3.8. Since

²These results are consistent also with the degree of relative axisymmetric imbalance shown in Schecter (2019, Fig. 1b).

the principal asymmetry of the upper tropospheric flow is azimuthal wavenumber one, and since the argument presented for the existence of the inflow jets invokes a vertical extension of the pressure field above and below the outflow layer, one might argue that the forcing of the inflow layers would apply equally to a sector of the upper-tropospheric flow region. To examine this possibility, as is shown in the left column of Figure 6.7 azimuth-height cross sections of the mean radial motion in an annular region between radii 50 km to 100 km at 42 h, 60 h and 74 h. At both these times, the mean upper-tropospheric outflow is more axisymmetric than the mean inflow just below it.

At 42 h, the inflow layer below the outflow layer is concentrated mostly in the sector going counterclockwise from approximately 30 deg. to the north of east (Figure 6.7 (a)) to the west (180 deg.) with a maximum value 70 deg. to the north of east. At 60 h, the inflow layer below the outflow layer is concentrated mostly in the sector going counterclockwise from approximately south (270 deg. in Figure 6.7 (c)) to the northwest (135 deg.) with a maximum value 25 deg. to the north of east and a minimum in the southwest (225 deg.). At 74 h (Figure 6.7 (e)), the outflow layer has thickened and developed two local maxima while the inflow has become more azimuthally confined and the maximum inflow has rotated counterclockwise to about 15 deg. east of north. At both times, the outflow is seen to be still ascending, while at 74 h, much of the lower inflow layer overlaps with a region of subsidence. These features may be seen from the two contours of vertical velocity in Figure 6.7 (e) with a magnitude of 0.25 m s^{-1} , the contour with the negative value being dashed.

If the argument is correct that the forcing of the upper inflow layers applies equally to a sector, then, subject to the caveat at the end of this paragraph, the sector with maximum inflow should correspond approximately with the sector with maximum outflow. At all three times in Figure 6.7, the azimuth of maximum inflow below the outflow is close to that of maximum outflow, the separation distance being about 20 deg. at 42 h and 60 h, being less than 10 deg. at 74 h. At 74 h, the same is true of the maximum inflow above the outflow, but at 60 h, the situation is less clear. At this time there are three sectors of enhanced inflow above the outflow and the strongest inflow maximum (near 180 deg.) lies far from that of the outflow maximum. Even so, there is a local inflow maximum at about 340 deg., within 20 deg. of the outflow maximum. At 42 h, there is no obvious inflows above the outflow yet.

Further support for the role of the agradient force in producing the inflow layers is obtained by examination of the azimuthal variation of the agradient force field as a function of height. As is shown in the right column of Figure 6.7, the regions of maximum upper-level inflow coincide on average with regions of maximum inward agradient forcing at these levels.

Overall, the foregoing findings point to the robustness of the argument that the inward agradient force is producing the upper-level inflow layers. Even though the occurrence of inflow above and below the outflow layer does not occur at all values of azimuth, the interpretation for the presence of inflow is based on the existence of an inward agradient force that either decelerates outflow or accelerates inflow. Thus, one does not necessarily expect a one-to-one correspondence everywhere between inward acceleration and inflow. Another

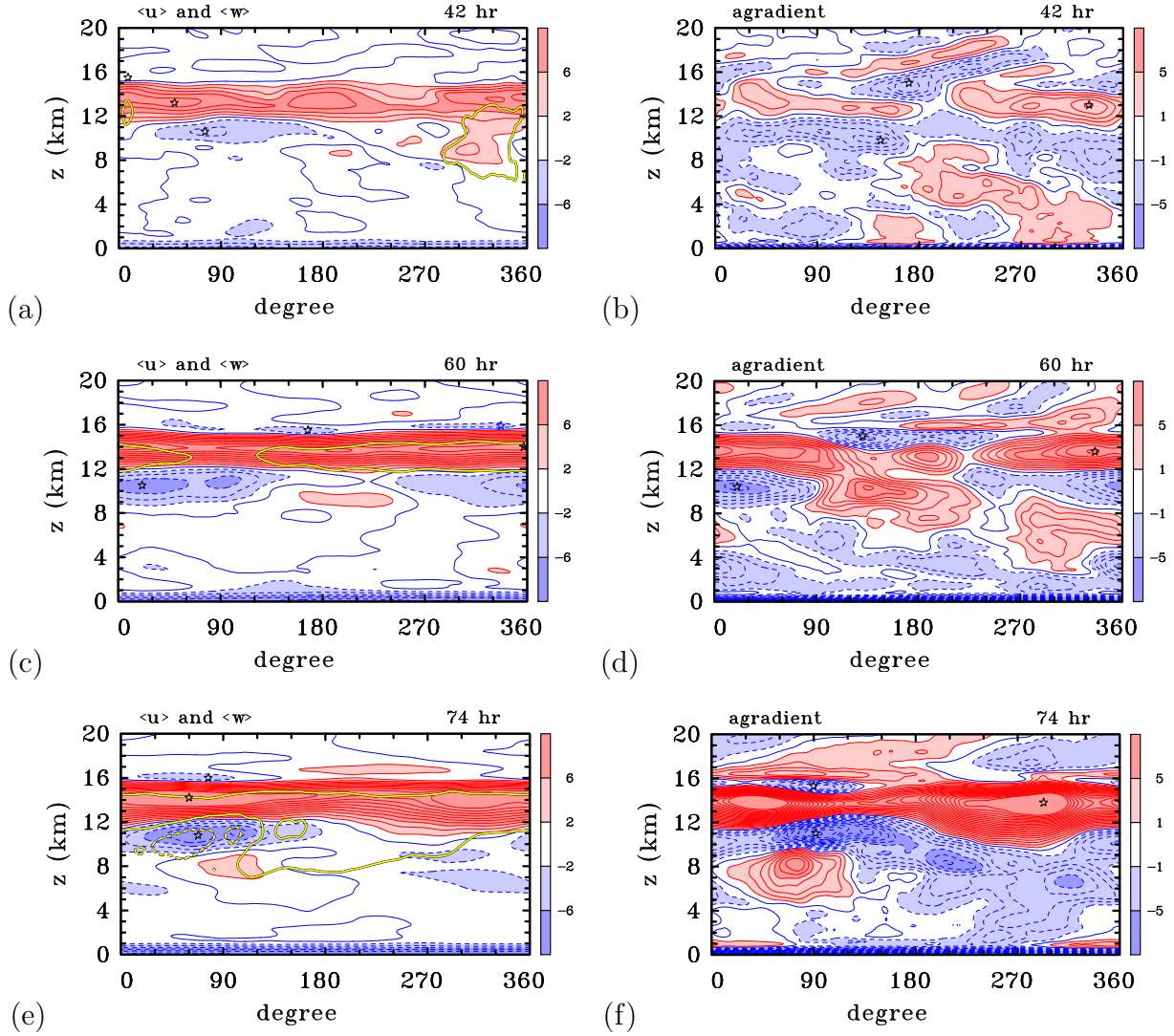


Figure 6.7: Azimuth-height cross sections of (a, c, e) the one hour time-averaged radial velocity component, $\langle u \rangle$, and vertical velocity, $\langle w \rangle$, (b, d, f) the one hour time-averaged gradient force, both averaged over an annulus from $r = 50$ km to 100 km, at 42 h (top), 60 h (middle) and 74 h (bottom). Contour interval for $\langle u \rangle$: 2 m s^{-1} , red solid contours for positive values, blue dashed contours for negative values, shading values on colour bar. Contours for $\langle w \rangle$: black and yellow solid contour 0.25 m s^{-1} , black and yellow dashed contour -0.25 m s^{-1} . Black star symbols denote locations of maximum inflow and outflow in the upper troposphere, the blue star in panel (a) is a local maximum inflow. The “east” direction corresponds with 0 deg. and azimuth is measured counterclockwise.

complication is the possibility that during vortex evolution, there may be occasional bouts of moderately deep convection that detrain in particular sectors at a lower level than the outflow layer, itself.

Clearly, the asymmetric structure of the upper-tropospheric outflow and inflow layers is complex, in part, because of the significant internal variability forced by deep convection as well as the inertia-buoyancy waves, vortex Rossby waves and possibly other instabilities excited by this convection (e.g., Anthes 1972; Flatau and Stevens 1993; Chen et al. 2003; Reasor and Montgomery 2015) and it would be simplistic to expect that an argument based on symmetric reasoning would be correct in all details. However, the interpretations given above are plausible.

6.5 Discussion

The analyses presented endorse a previous idea of Ooyama (1987) to view the outflow layer as an expanding jet of air emanating from a radial mass and momentum source where the eyewall convection terminates. They suggest also a new way to think about the inflow layers above and below the outflow layer. From an azimuthally-averaged perspective, I showed that the outflow, itself, is driven near its source primarily by a positive agradient force in which the centrifugal and Coriolis force in the radial direction is partly opposed by the radially-inward pressure gradient force. As air parcels move outwards, approximately conserving their absolute angular momentum, the tangential velocity diminishes as does the sum of the centrifugal and Coriolis forces. Well beyond the source, the inward-directed radial pressure gradient force begins to dominate and leads to a deceleration of the outflow. The inward pressure gradient force extends vertically above and below the outflow layer, itself, and leads to a flow response on either side of the outflow layer, where it accelerates air parcels inwards. There is a significant degree of imbalance in the upper troposphere.

The inflow layers adjacent to the upper-level outflow were shown to be more asymmetric than the outflow layer, itself, having a low azimuthal wavenumber flow asymmetry. Nevertheless, the region of maximum inflow above and below the outflow layer tends to align with that of maximum outflow, which, in a first approximation, supports the foregoing interpretation of the inflow layers based on axisymmetric reasoning.

In summary, this work outlines a new framework for examining the outflow and inflow layer dynamics in tropical cyclone vortices. Further work on the asymmetric aspects of these layers, as well as an understanding of their modification in more complex environments would be of meteorological and fluid dynamical interest.

Chapter 7

Trajectories

Two unanswered questions about the inflow layer beneath the outflow layer are: where does this air go and what is the impact on the thermodynamics of the upper tropospheric? In this chapter I will address these questions by carrying out a series of trajectory calculations and calculating the variation of pseudo-equivalent potential temperature, θ_e along these trajectories.

The chapter is organized as follows. Section 7.1 describes the method for calculating the trajectories and model output used. Section 7.2 presents the main results the trajectory calculations, showing a series of sample trajectories (Section 7.2.1) and the statistics of many trajectories (Section 7.2.2). Section 7.2.1 examines also the variation of pseudo-equivalent potential temperature along trajectories. Section 7.3 presents a brief discussion of the relationship of the results to those of a recent study. The discussion is presented in Section 7.4.

7.1 Method for calculating trajectories

The trajectories are calculated using output data from the model simulation in Chapter 2. For the present calculations, the output data are interpolated to a new fine grid in a region 800 km square in the horizontal and 20 km in the vertical using bicubic splines. This new grid has a horizontal grid spacing of 1 km and a vertical grid spacing of 100 m.

The main set of trajectory calculations start at 60 h of model integration. These calculations are for air parcels located every 2 km, from 60 km radius to 130 km radius and every 5 degrees in azimuth at the maximum inflow height of 11 km, which is within the upper inflow layer beneath the outflow layer (see Figure 3.2(d)). In total, there are 2592 trajectories. Here, 60 km is chosen as it is the radius where the azimuthally-averaged vertical velocity is zero and therefore beyond the eyewall updraught. The 130 km radius is chosen to encompass the extent of relatively strong inflow, being where the azimuthally-averaged radial inflow velocity falls below 2 m s^{-1} in magnitude. The details of other sets of trajectories will be described where they are discussed.

The computation of trajectories uses the formula:

$$\vec{r}_{t_{n+1}} = \vec{r}_{t_n} + \frac{1}{2}(\vec{V}_{t_{n+1}} + \vec{V}_{t_n})\Delta t, \quad (7.1)$$

where, \vec{r}_{t_n} is the three dimensional position vector of an air parcel at time t_n , \vec{V}_{t_n} is the three dimensional velocity vector at the location of the parcel at this time and Δt is time step, here 15 min. A tri-linear interpolation is used to determine \vec{V}_{t_n} when the air parcel does not lie on a model grid point. If an air parcel moves beyond a radius of 400 km from the vortex centre or above 20 km in height, the calculation for that air parcel is terminated.

7.2 Results

7.2.1 Sample trajectories

Figure 7.1 shows two sets of eight trajectories, each starting along a radial line from 60 km radius to 130 km radius with a spacing of 10 km and having a duration of 24 h. The left column of Figure 7.1 shows trajectories of air parcels with initial positions along a radial line located in the quadrant with a relatively strong inflow component (see Figure 3.6). The three panels (a), (c) and (e) of Figure 7.1 provide different perspectives of the trajectories. There are two main groups of trajectory in this set.

- (1) the air parcels starting at 70, 80 and 110 km radius spiral cyclonically inwards before entering the eyewall updraught. They ascend in the updraught and move rapidly outwards in the outflow layer, taking less than 12 h to move more than 250 km in radius from the vortex centre.
- (2) the air parcels starting at 90, 100, 120 and 130 km radius spiral cyclonically inwards before subsiding beyond the eyewall updraught to a layer between about 8 km and 9 km, where the radial flow is relatively weak. Subsequently, they move slowly outwards. Even after 24 h, these air parcels remain within a radius of 250 km from the vortex centre.

Unlike these two types above, the air parcel initialized at 60 km first descends like those in group (2), but it doesn't descend as far, remaining above 10 km height. Its subsequent motion is erratic in both the horizontal and vertical, at one point rising to 12 km altitude. After about 18 h, this air parcel enters the eyewall updraught, ascending rapidly before entering the outflow and moving outwards like the air parcels in group (1).

The right column of Figure 7.1 shows trajectories with initial positions along a radial line located in the quadrant with a relative weak inflow component (see Figure 3.6). Again, the three panels (b), (d) and (f) of Figure 7.1 provide different perspectives of the trajectories. As in the previous set of trajectories, the behaviour in this case is not systematic in radius. The air parcels starting at 70, 90 km and further move outwards at first, but turn inwards later. Of these, the parcels starting at 70, 90 and 100 km spiral cyclonically downwards

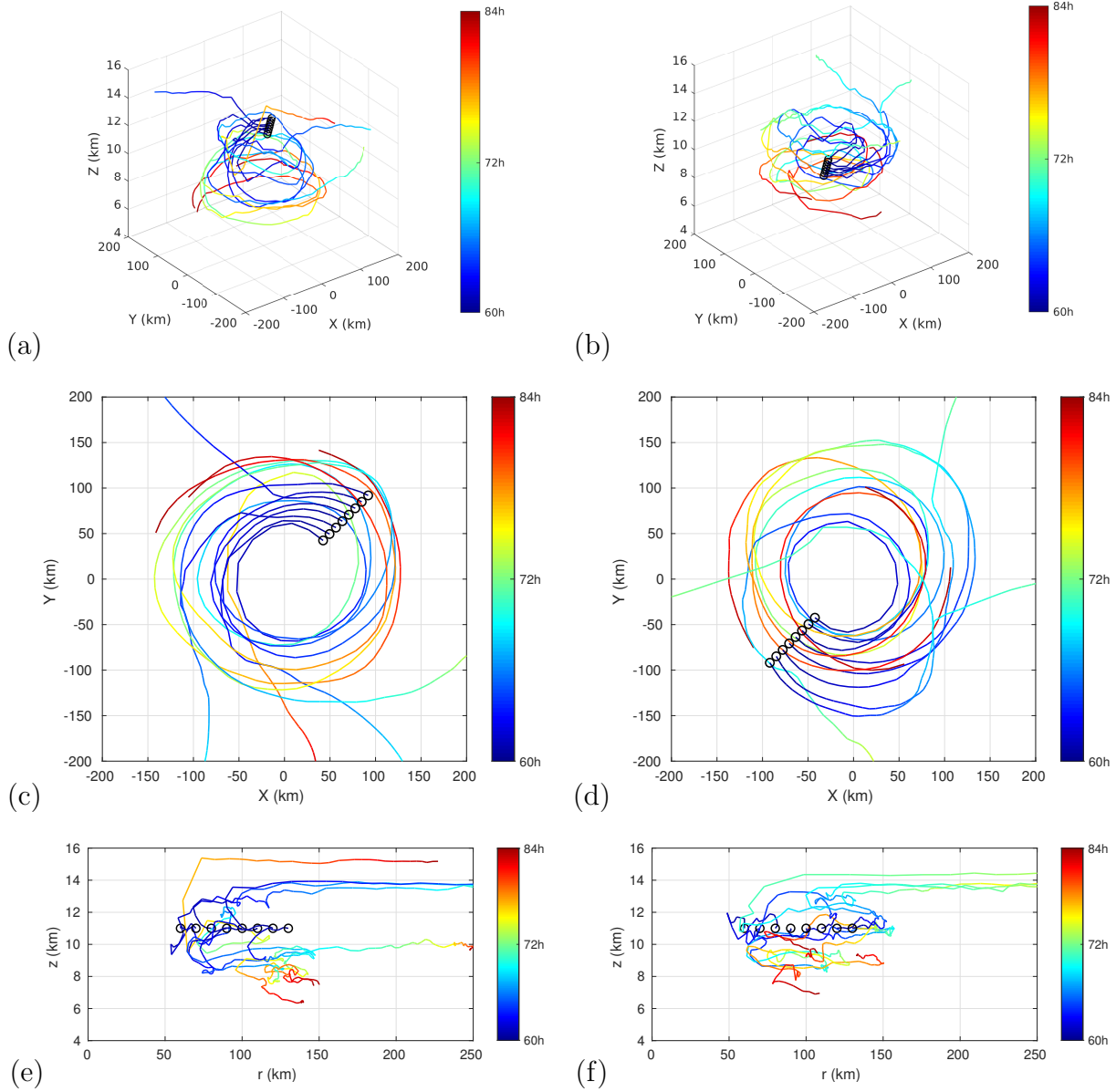


Figure 7.1: Two sets of eight 24 h trajectories, each starting along a radial line in the inflow layer below the upper-tropospheric outflow layer at an altitude of 11 km. Trajectories in the left column lie in the quadrant with a relatively strong inflow, while those in the right column lie in a quadrant where the inflow is relatively weak. (a), (b) show a three-dimensional view; (c), (d) show a horizontal plan view; (e), (f) shows a vertical plan view in the radius-height plane. Initial locations are marked by black circles. Time evolution indicated in the colour bar.

and outwards, ending up after 24 h in the middle layer. In contrast, the parcels starting at

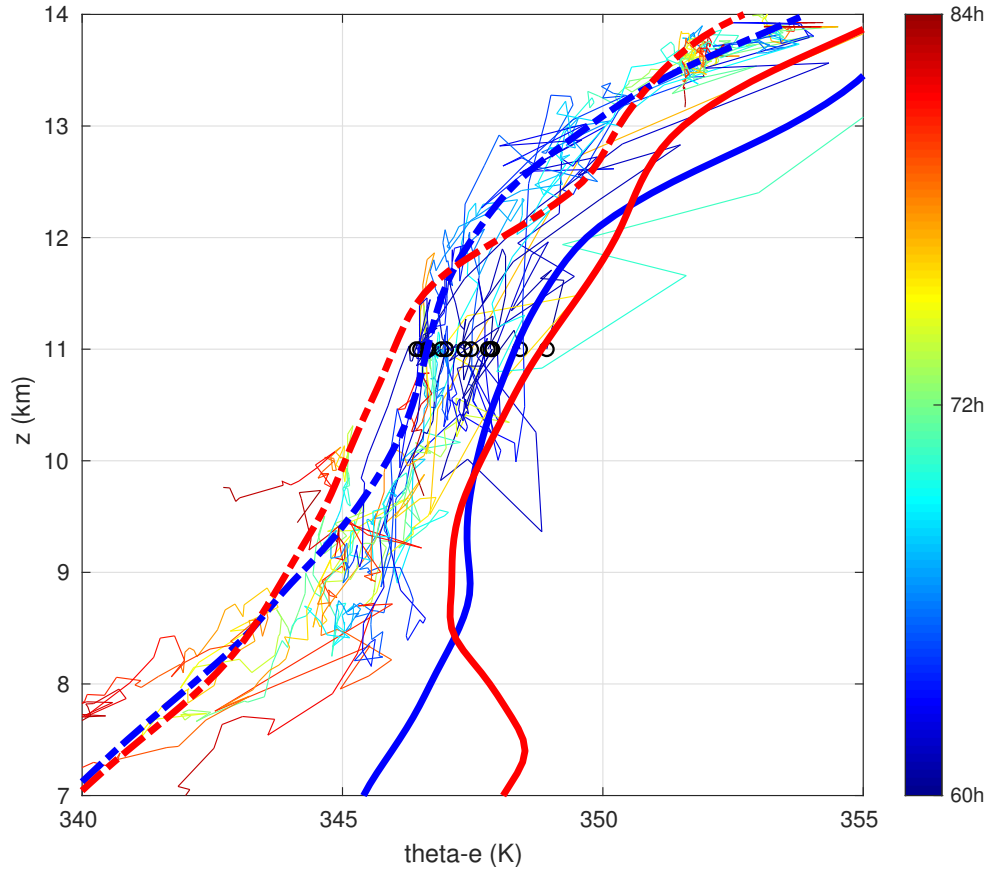


Figure 7.2: Variation of pseudo-equivalent potential temperature, θ_e , along the 16 trajectories in Figure 7.1 (thin curves) as a function of height, z , and colour coded as a function of time (indicated on the colour bar). Thick curves show for reference the azimuthally-averaged profiles of θ_e at 60 km radius at 60 h (blue) and 84 h (red). Dashed curves show similar reference profiles at 130 km radius.

110 km and beyond spiral upwards in the eyewall updraught and are carried outwards in the outflow layer. The remaining air parcels starting at 60 and 80 km both spiral inwards and downwards at first, but their subsequent tracks differ. The parcel starting at 60 km slowly spirals outwards to the middle layer, while that starting at 80 km enters a strong updraught and ends up in the outflow layer. As in the previous set of trajectories, the air parcels which end up in the outflow layer take less than 12 h to move more than 250 km in radius from the vortex centre, while those that descend to the middle layer remain within a radius of 150 km after 24 h.

At this point it is worth noting that, although the data used for the foregoing trajectory calculations has a relatively high spatial resolution, it was not possible to store the three dimensional model data more frequently than every 15 minutes. The limitation appears to be most serious in short segments of trajectories where air parcels ascend rapidly in the eyewall updraught. In general, it is not likely to have a significant impact on my findings.

It is clear from the foregoing analysis that, as a result of even low azimuthal wavenumber variations in vortex structure, there is a complex “stirring” taking place within the middle and upper levels of the vortex as a result of the inflow layers. In the absence of turbulent diffusion, this stirring would contribute to a rich structure in the pattern of approximately materially-conserved quantities such as the pseudo-equivalent potential temperature, θ_e . In reality, of course, such a structure might be considerably modified by diffusion. The effects of stirring and diffusion in a simple barotropic vortex flow are discussed by Meunier and Villerraux (2003).

To investigate the effects of the turbulent diffusion of heat and moisture on the θ_e distribution, I show in Figure. 7.2 the values of θ_e along the tracks of the 16 air parcels investigated in Figure 7.1. Shown also are the vertical profiles of azimuthally-averaged values of θ_e at 60 km and 130 km radius, the extremes of the initial air parcel locations, at the initial time (60 h) and final time (84 h) of the trajectory calculations. The profiles at 84 h are shown merely to judge the temporal variation of the profiles, but, of course, air parcels do not, in general, remain in the annulus between 60 km and 130 km radius. If θ_e were approximately materially-conserved, the values of θ_e along parcel trajectories would appear as approximately vertical lines in the figure. The fact that this is not the case and that the values lie mostly within the range of values of the azimuthally-averaged profiles between 60 km and 130 km radius at 60 h (the thick solid lines in the figure) is strong evidence that turbulent diffusion of heat and moisture along trajectories is appreciable in the middle and upper troposphere. Despite the fact that this result is dependent on the fidelity of the representation of turbulent diffusion in the CM1 model, it would be reasonable to surmise that the same would be true in the real atmosphere.

The implications of the existence of upper-level inflow layers and the inferred strong upper-tropospheric mixing for the thermodynamic Carnot model of tropical cyclones (see Section 1.3) have yet to be determined.

7.2.2 Statistics of trajectories

The results of the previous section highlight the complexity of trajectories, even when the starting positions are uniformly spaced along a horizontal radial line within the inflow layer. There must be a stochastic element responsible for this complexity because, for example, the rapid ascent of air parcels to the outflow layer takes place in strong and localized deep convective cores, which, themselves, have a stochastic element. Because of this stochastic element, it is appropriate to analyse the statistics of a large number of air parcels starting in the inflow layer. To this end, I examine the distribution of end locations after 24 h of all 2592 trajectories calculated in Section 7.1.

Figure 7.3(a) shows a histogram of the heights of the foregoing end locations. Height ranges are divided into 100 bins with the same width and the number of end trajectories in each bin is divided by the number of trajectories (2592) to give a fractional number density distribution. The solid red curve in this figure represents the cumulative distribution function. The end trajectories are confined mainly to two layers, one coinciding with the upper outflow layer and the other in the mid to upper troposphere somewhat below the

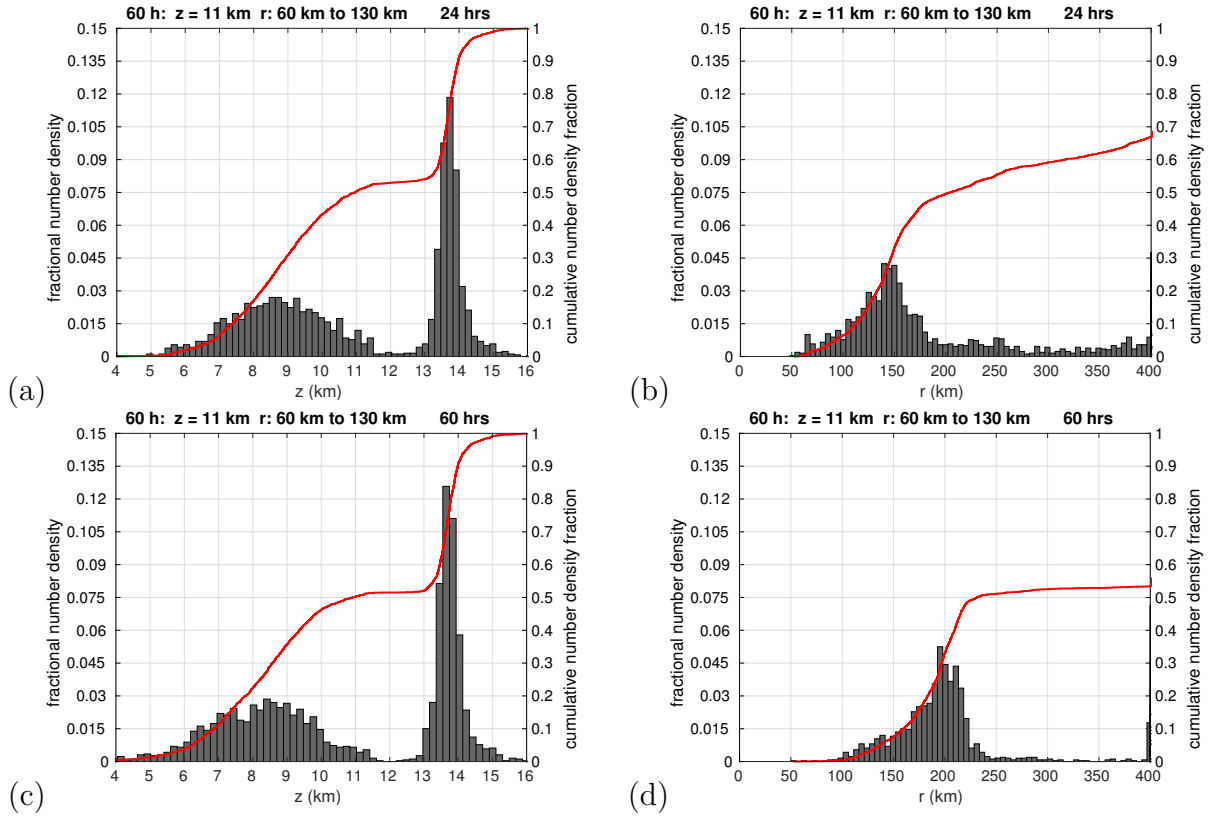


Figure 7.3: Histograms of end locations of all 2592 trajectories initialized in the inflow layer at 11 km height at 60 h as described in the text. (a, c) show the height distribution of end locations, (b, d) show the radial distribution of end locations inside a radius of 400 km. Upper panels for 24 h trajectories, lower panels for 60 h trajectories. Bin number is 100 for each panel. Number density is expressed as a proportion of the total number of trajectories. The red curves show the cumulative number density fraction.

outflow layer. The distribution in the outflow layer is relatively sharp with the peak number density at an altitude of about 13.5 km. The distribution in the mid to upper troposphere is rather broader and a maximum number density at about 8.5 km. The cumulative number density fraction curve shows that air parcels subsiding from the upper inflow layer do not descend below about 5 km. Thus, they do not reach the frictional boundary layer.

Figure 7.3(b) shows a similar histogram to that in panel (a), but for the end radii of trajectories after 24 h. There is a peak of number density at about 150 km where most trajectories end up at this radius. All trajectories end up beyond a radius of 50 km and the distribution has a considerable radial spread with a peak near 150 km radius and a long tail with low number density beyond about 180 km radius. About 33 % of trajectories move out beyond a radius of 400 km, which accounts for the reduction of the maximum cumulative number density fraction in the histogram. It turns out that trajectories which descend to the middle layer end within 270 km of the axis and all those that end beyond this radius ascend to the outflow layer. I have verified this finding by plotting the histogram

for only air parcels that descend and only air parcels that ascend (not shown).

Figures 7.3(c) and 7.3(d) show similar histograms to those in panels (a) and (b), but for trajectories of 60 h duration. The major features of the histogram in panel (c) are essentially the same as those in panel (a). The trajectory end locations shows two separate bell-shaped distributions, a broader one with smaller peak value centred near an altitude of 8.5 km and a more peaked one with much larger amplitude near an altitude of 13.8 km. Even the magnitude and spread of these distributions are similar. The intersection of the cumulative number density curve with the reference line at 11 km altitude is 0.5 in both panels, indicating that, at both end times, about half of the trajectories ascend into the outflow and the other half subside. The small differences between the distributions in panels (a) and (c) provide confidence in the robustness of the distributions.

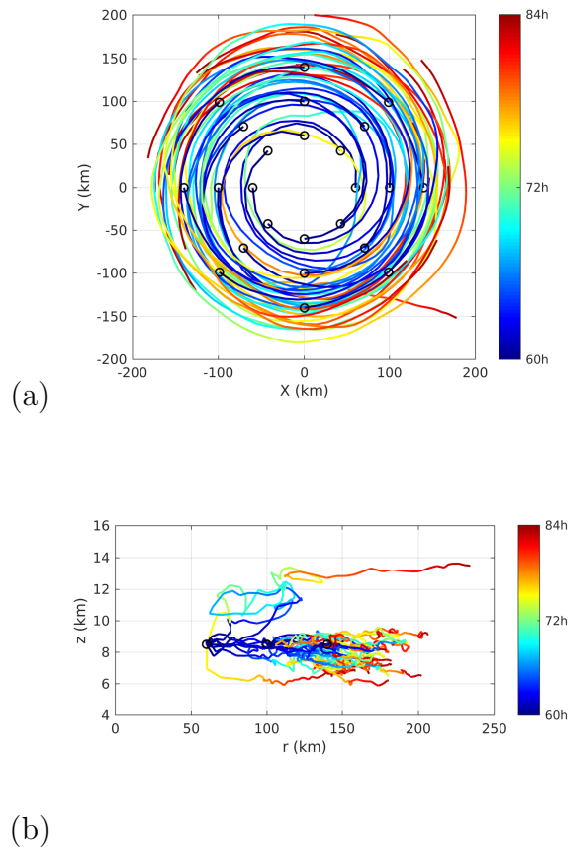


Figure 7.4: A set of 24, 24 h trajectories starting at a height of 8.5 km at a height of 8.5 km. (a) a horizontal plan view; (b) a vertical plan view in the radius-height plane. Initial locations are marked by black circles. Time evolution indicated in the colour bar.

The histogram in Figure 7.3(d) shows the radius of the end of trajectories at 60 h, which should be compared with the situation at 24 h in Figures 7.3(b). Three features stand out: (1) the peak in the distribution has moved outwards in radius from about 140 km to near 200 km; (2) there are fewer end trajectories beyond about 240 km; and (3) the

maximum cumulative number density has reduced further to about 53 %. The reason for both (2) and (3) is that the end trajectories at larger radii at 24 h are mostly in the upper level outflow and by 60 h, these have moved out of the 400 km domain and are no longer counted. The outward shift in the distribution of end radii is because these trajectories lie in a region of the mid- to upper troposphere where there is a slow outward drift.

If a significant fraction of air parcels in the inflow layer beneath the outflow descend and move slowly outwards at levels mostly between 6 and 10 km, the question is raised where air parcels originally (at 60 h) move to. To answer this question I calculate an additional set of 24 air parcel trajectories to those described in Section 7.1. The air parcels are located initially along radial lines at a height of 8.5 km at 60 h. The lines are every 45 degrees and the air parcels are located at 60, 100 and 140 km radius along these lines. The trajectories, which have a duration of 24 h, are shown in Figure 7.4. Figure 7.4(a) shows a horizontal perspective of the trajectories and Figure 7.4(b) shows a radius-height perspective.

The majority of these air parcels spiral slowly cyclonically outwards while slowly subsiding. They remain within a radius of 200 km from the vortex centre and above 6 km, even after 24 h. Evidently the overturning circulation in the mid- to upper troposphere below the inflow layer and outside the eyewall is relatively weak. Only two air parcels, both initially at 60 km radius, show a different behaviour. They enter a strong updraught area beyond the eyewall in the first 3 h and are carried into the upper inflow layer at a radius of about 110 km. Then, they spiral cyclonically inwards. One of these air parcels subsequently ascends in the eyewall updraught and moves rapidly outwards in the outflow layer while the other subsides to about 8 km height.

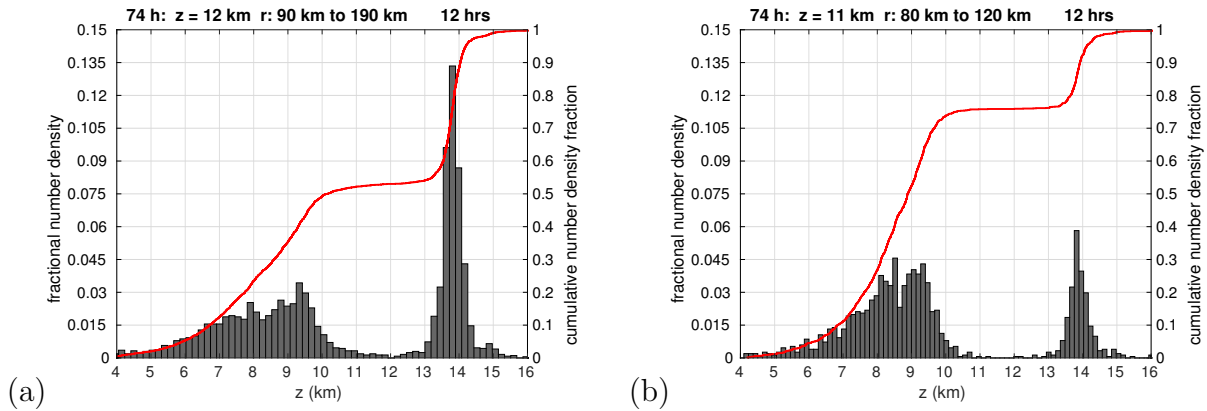


Figure 7.5: Histograms of the height of end locations of (a) all 4032 trajectories initialized in the inflow layer at 12 km height at 74 h described in the text; (b) all 4032 trajectories initialized in the inflow layer at 11 km height at 74 h described in the text. 12 h trajectories are shown. Bin number is 100 for each panel. Number density is expressed as a proportion of the total number of trajectories. The red curves show the cumulative number density fraction.

In order to judge the representativeness of the above results, histograms of the statistics

of two sets of trajectories calculations at 74 h are shown in Figure 7.5. Figure 7.5(a) shows a histogram of the height of end locations of all 4032 trajectories initialized in the inflow layer at 74 h after 12 h. Those trajectories are calculated for air parcels located every 2 km from 90 km radius to 190 km radius and every 5 degrees in azimuth at a height of 12 km in the upper inflow layer. Here, 90 km is chosen as it is the radius where, again, the azimuthally-averaged vertical velocity is zero and therefore beyond the eyewall updraught (see Figure 3.2(f)). As in Figures 7.3(a) and 7.3(c), the distribution of trajectory end heights has two peaks, one in the upper outflow layer and the other in the mid to upper troposphere. The cumulative number density curve at 12 km shows that about 53 % trajectories subside while 47 % trajectories ascend into the outflow, comparable with the proportions in Figure 7.3.

Figure 7.5(b) shows a histogram of the end heights of a second set of 1512 trajectories initialized again in the inflow layer, but at a height of 11 km at 74 h (cf. Figure 3.2(f)). These trajectories are calculated for air parcels located every 2 km from 80 km radius to 120 km radius and every 5 degrees in azimuth in the bottom of the upper inflow layer of a height and again end after 12 h. Once more, 80 km is chosen as it is the radius where the azimuthally-averaged vertical velocity is zero. The 120 km radius is chosen to encompass the extent of relatively strong inflow, being where the azimuthally-averaged radial inflow velocity falls below 2 m s^{-1} in magnitude (see Figure 3.2(f)). It is seen that about 76 % of these trajectories subside into the mid to upper troposphere and only 24 % ascend in the eyewall to the outflow layer, presumably because of increased upper level subsidence at later times as seen in see Figure 3.2(f).

7.3 Relationship to other studies

A much earlier study of trajectories in hurricanes is that of Cram et al. (2007), who investigated transport and mixing characteristics of a large sample of air parcels within a high-resolution (2-km horizontal grid spacing) numerical simulation of *Hurricane Bonnie* (1998). The main focus of their paper was on the eye, eyewall, and near environment during the mature stage of this vertically sheared hurricane, but a few back trajectories were calculated also. These backwards trajectories show that one-fifth of the mass in the eyewall at a height of 5 km has an origin in the mid- to upper-level environment. In their Figure 16c, Cram et al. show some trajectories at upper levels outside the eyewall updraught that descend along a slanted path to middle levels, similar to the air parcels in Group (2) described in Section 7.2.1.

A more recent paper is that by Cohen and Paldor (2020) entitled “Lagrangian trajectories at (*sic*) the outflow layer of tropical cyclones”. Whereas my trajectory calculations are based on a three-dimensional numerical simulation and focus on trajectories that start within the inflow layer below the outflow layer, Cohen and Paldor consider only trajectories in the outflow layer within an axi-symmetric configuration. Moreover, they prescribe the pressure gradient in this layer. In general, one cannot do this, of course, because the pressure gradient has to produce accelerations and hence velocities that satisfy mass con-

tinuity. For example, in an incompressible (or anelastic) fluid flow, the pressure field is determined diagnostically at any instant of time by a Poisson-type equation by the velocity field in such a way that suitable boundary conditions are satisfied on the flow domain and mass continuity is ensured. For a field of air parcels moving in a prescribed pressure field, the mass continuity constraint must, in general, be forfeited. On these grounds, I have reservations about the results of the Cohen and Paldor study.

7.4 Discussion

Data from an idealized and relatively high resolution three-dimensional numerical simulation have been used to investigate the trajectories of air parcels starting in the upper tropospheric inflow layer just beneath the outflow layer. I showed that about half of the inflowing air parcels enter the eyewall updraught where they ascend and are rapidly carried outwards in the outflow layer, itself. The remaining air parcels subside and drift slowly outwards in the mid- to upper troposphere where there is a weak overturning circulation.

A histogram of the distribution of 24 h and 60 h end locations of trajectories shows two peaks in the height, a sharp peak centred at 13.5 km within the upper level outflow and a broader peak centred at 8.5 km below the inflow layer. The air parcels subsiding from the inflow layer do not descend below about 5 km. The small differences between the distributions for 24 h trajectories and 60 h trajectories are an indication of the robustness of these features.

Calculations of pseudo-equivalent potential temperature along the air parcel trajectories indicate that this quantity is not materially-conserved, even approximately, indicating that the turbulent diffusion of heat and moisture along the trajectories is appreciable in the middle and upper troposphere. Of course, an extension of this result to the real atmosphere relies on the fidelity of the representation of turbulent diffusion in the CM1 model used for the simulation. Nevertheless, the strong diffusion of heat and moisture would mitigate the impact of the inflow layers on the thermodynamics of the upper troposphere compared with the situation if pseudo-equivalent potential temperature were approximately materially conserved. The implications of this strong diffusion and of the existence of the inflow layers, themselves, for the thermodynamical Carnot heat engine model for a mature tropical cyclone have yet to be determined.

While the data available for the foregoing trajectory calculations has a relatively high spatial resolution, storage issues restricted the temporal availability of data to 15-minute intervals. The limitation appeared most serious in short segments of those trajectories where air parcels ascend rapidly in the eyewall updraught and is unlikely to have a major impact on my findings.

Chapter 8

Conclusions

Three-dimensional numerical simulations of tropical cyclone intensification with moderately high vertical resolution have been used to analyze the development of a layer of strong inflow beneath the upper tropospheric outflow layer as well as, in some cases, a shallower layer of weaker inflow above the outflow layer. The calculations pertain to the prototype problem for tropical-cyclone intensification, which considers the evolution of a vortex on an f -plane in a quiescent environment starting from an initially-symmetric, moist, cloud-free vortex over a warm ocean.

In Chapter 3, the inflow layers adjacent to the upper-level outflow were shown to have a role in modifying the vortex structure in the upper troposphere. The inflow layer above the outflow layer leads to a spin up of the tangential winds there, thereby extending the cyclonic circulation of the hurricane vertically. In addition, the inflow acts to resist the radial spread of air with high equivalent potential temperature at this level. The inflow layer below the outflow layer leads also to a spin up of the cyclonic tangential winds in the inflow layer and would appear to contribute to an increase of the radial gradient of equivalent potential temperature at the outer edge of the eyewall. The inflow layers adjacent to the upper-level outflow were shown to be more asymmetric than the outflow layer, itself, having a low azimuthal wavenumber flow asymmetry.

Chapter 4 developed a framework for exploring the consequences of regularizing the Sawyer-Eliassen equation to diagnose the streamfunction for the axisymmetric secondary circulation of a tropical cyclone subject to a given distribution of diabatic forcing and tangential frictional stress. Regularization amounts to adjusting the coefficients of the equation in regions where the discriminant is negative to ensure that the equation is globally elliptic. The possible consequences of regularization have been explored using the analog behaviour of a stretched membrane subject to a particular force distribution.

Regularization is required in three regions: (1) regions where the flow is inertially unstable; (2) regions where it is statically unstable; and (3) regions where the baroclinicity is large. Regions of large baroclinicity are typically ones of large vertical shear. In numerical models of tropical cyclones, regions of azimuthally-averaged inertial instability are generally the most extensive, while regions of static instability are typically small in areal extent. Regions where the azimuthally-averaged baroclinicity is large are typically con-

fined to the lower part of the frictional boundary layer, where the vertical shear is large. However, setting the inertial stability to be small and positive in regions of inertial instability generally requires the baroclinicity to be reduced in magnitude as well to keep the discriminant of the Sawyer-Eliassen equation positive. Possible improvements in the procedure for regularizing in cases (1) and (3) were suggested.

A comparison of the azimuthally-averaged radial flow from a three-dimensional numerical simulation of a tropical cyclone with those from an axisymmetric balance calculation of the Sawyer-Eliassen equation forced by diabatic and frictional terms from the numerical simulation was presented. Important findings from this comparison are:

- (1) The largest uncertainty in the integrity of the balance solutions results from the regularization in regions of inertial instability, especially when the diagnosed forcing overlaps with such regions. In the example shown, where there is some overlap of this type, the diagnosed balanced flow is sensitive to the particular procedure for regularization and none of the schemes produced a flow that was structurally and quantitatively close to that obtained from the numerical solution.
- (2) Regularization in regions of large vertical shear that typically occur in the lower part of the boundary layer is less problematic, even though such regions are ones in which there is forcing. The reason is that a modification of the coefficient B in the Sawyer-Eliassen equation leads to a rotation of the streamfunction response, but the degree of rotation is constrained by the proximity of the lower boundary.
- (3) On account of (2), the large difference found between the low-level inflow in the azimuthally-averaged numerical solution and that in the axisymmetric balance solution is further indication that *balance dynamics is unable to adequately capture the flow in the boundary layer*, contrary to recent claims.

While balance ideas have played a central role in the development of a theoretical framework for understanding tropical cyclone dynamics, the application of such ideas to diagnose the results of numerical simulations almost always requires that the Sawyer-Eliassen equation be regularized. Regularization is intrinsically an *ad hoc* procedure and some methods may be better than others. Exploitation of the membrane analogy as outlined herein would seem to offer a useful framework for assessing the integrity of such procedures and their possible limitations. The analysis suggests, however, that regularization introduces uncertainties in the integrity of balance solutions to a degree that much caution is called for in the use of such solutions for “explaining” tropical cyclone structure, especially within and near the regions which have been regularized.

In Chapter 5, I investigated a potential balance explanation for upper tropospheric inflow jets. The explanation for the inflow layers in terms of axisymmetric balance dynamics is shown to be problematic. I have compared two solution methods, the SOR-method and a multi-grid method, to solve the Sawyer-Eliassen equation for the balanced secondary circulation of a tropical cyclone vortex to a particular forcing distribution of diabatic heating and tangential momentum forcing. These solutions affirm prior findings concerning

the need to coarsen the data from high-resolution numerical simulations in the presence of inertial or symmetric instability when applied to determine the corresponding balanced secondary circulation. They show also that the multi-grid method is able to obtain a convergent solution with a finer grid spacing than the SOR method, although it too fails when the grid spacing is too small. When both methods converge *and the vortex is symmetrically stable*, the solutions are broadly similar.

The inflow layer just beneath the upper-level outflow layer in a balance flow solution of the Sawyer-Eliassen equation corresponding to a typical tropical cyclone simulation is a consequence of the need to regularize this equation in regions of inertial and/or symmetric instability. Because regularization is an *ad hoc* procedure, this inference calls for caution in attributing such inflow layers to a balanced flow response driven by the distribution of diabatic heating and tangential momentum forcing. Thus, an explanation of the upper-level inflow layers that are found in numerical simulations of tropical cyclones needs to be based on more fundamental considerations than assuming global thermal wind balance.

The analyses in Chapter 6 endorse a previous idea of Ooyama (1987) to view the outflow layer as an expanding jet of air emanating from a radial mass and momentum source where the eyewall convection terminates. They suggest also a new way to think about the inflow layers above and below the outflow layer. From an azimuthally-averaged perspective, I showed that the outflow, itself, is driven near its source primarily by a positive agradient force in which the sum of the centrifugal and Coriolis force in the radial direction is partly opposed by the radially-inward pressure gradient force. As air parcels move outwards, approximately conserving their absolute angular momentum, the tangential velocity diminishes as does the sum of the centrifugal and Coriolis forces. Well beyond the source, the inward-directed radial pressure gradient force begins to dominate and leads to a deceleration of the outflow. The inward pressure gradient force extends vertically above and below the outflow layer, itself, and leads to a flow response on either side of the outflow layer, where it accelerates air parcels inwards. There is a significant degree of imbalance in the upper troposphere.

The inflow layers adjacent to the upper-level outflow were shown to be more asymmetric than the outflow layer, itself, having a low azimuthal wavenumber flow asymmetry. Nevertheless, the region of maximum inflow above and below the outflow layer tends to align with that of maximum outflow, which, to a first approximation, supports the foregoing interpretation of the inflow layers based on axisymmetric reasoning.

In summary, this part of the work outlines a new framework for examining the outflow and inflow layer dynamics in tropical cyclone vortices. Further work on the asymmetric aspects of these layers, as well as an understanding of their modification in more complex environments would be of meteorological and fluid dynamical interest.

Chapter 7 investigated the trajectories of air parcels starting in the upper tropospheric inflow layer just beneath the outflow layer. I showed that about half of the inflowing air parcels enter the eyewall updraught where they ascend and are rapidly carried outwards in the outflow layer, itself. The remaining air parcels subside and drift slowly outwards in the mid- to upper troposphere where there is a weak overturning circulation.

A histogram of the distribution of 24 h and 60 h end locations of trajectories shows

two peaks in the height, a sharp peak centred at 13.5 km within the upper level outflow and a broader peak centred at 8.5 km below the inflow layer. The air parcels subsiding from the inflow layer do not descend below about 5 km. The small differences between the distributions for 24 h trajectories and 60 h trajectories are an indication of the robustness of these features.

Calculations of pseudo-equivalent potential temperature along the air parcel trajectories indicate that this quantity is not materially-conserved, even approximately, indicating that the turbulent diffusion of heat and moisture along the trajectories is appreciable in the middle and upper troposphere. Of course, an extension of this result to the real atmosphere relies on the fidelity of the representation of turbulent diffusion in the CM1 model used for the simulation. Nevertheless, the strong diffusion of heat and moisture would mitigate the impact of the inflow layers on the thermodynamics of the upper troposphere compared with the situation if pseudo-equivalent potential temperature were approximately materially conserved. The implications of this strong diffusion and of the existence of the inflow layers, themselves, for the thermodynamical Carnot heat engine model for a mature tropical cyclone have yet to be determined.

While the data available for the foregoing trajectory calculations has a relatively high spatial resolution, storage issues restricted the temporal availability of data to 15-minute intervals. The limitation appeared most serious in short segments of those trajectories where air parcels ascend rapidly in the eyewall updraught and is unlikely to have a major impact on my findings.

Appendix A

List of acronyms

ARPS	Advanced Regional Prediction System
CM1	Cloud Model 1 (of George Bryan)
JMA	Japan Meteorological Agency
JTWC	Joint Typhoon Warning Center
MG	Multi-Grid
MM5	Pennsylvania State University/ National Center for Atmospheric Research mesoscale model
NASA	National Aeronautics and Space Administration
NCAR	National Center for Atmospheric Research
NHC	National Hurricane Center
RAMS	Regional Atmospheric Modeling System
RMSE	Root Mean Square Error
SOR	Successive Over-Relaxation
WMO	World Meteorological Organization
WRF	Weather Research and Forecasting model

Appendix B

List of symbols

The principal symbols are listed in this chapter. Extended symbols formed by adding bars, brackets, primes or upper and lower indices are not generally listed here, but explained in the text where they appear.

b	Buoyancy
B	Baroclinicity
C	Sum of centrifugal and Coriolis forces per unit mass
C_p	Specific gas constant for dry air at constant pressure
D_u, D_v, T_w	Optional diffusive tendencies for velocity components (u, v, w)
D_s	Optional diffusive tendency, while s represents model scalars (θ, q_v, q_l, q_i)
e_i	Difference between the model simulation and balance solution
f	Coriolis parameter
g	Acceleration due to gravity
I_g	Generalized inertial stability
I^2	Inertial stability squared
$K_{m,h}$	Horizontal diffusivities of horizontal momentum
$K_{m,v}$	Vertical diffusivities of horizontal momentum
L_v	Latent heat of freezing
L_s	Latent heat of sublimation
L_f	Latent heat of freezing
M	Absolute angular momentum

n	Number of points
N	Static stability
N_u, N_v, N_w	Newtonian relaxation for velocity components (u, v, w)
N_s	Newtonian relaxation, while s represents model scalars (θ, q_v, q_l, q_i)
p	Pressure
p_{00}	Standard reference pressure
PV	Potential vorticity
q_v	Water vapor mixing ratio
q_l	Mixing ratio of liquid water
q_i	Mixing ratio of solid water (ice)
$\dot{q}_{cond}, \dot{q}_{dep}, \dot{q}_{frz}$	Phase changes between liquid water, solid water (ice) and water vapor
\dot{Q}_θ	External tendencies to internal energy, primarily radiative heating/cooling
r	Radius
\vec{r}	Three dimensional position vector
R_d	Specific gas constant for dry air
R_v	Specific gas constant for water vapor
t	Time
T	Temperature
T_l	Condensation temperature
T_u, T_v, T_w	Turbulence tendencies for velocity components (u, v, w)
T_s	Turbulence tendency, while s represents model scalars (θ, q_v, q_l, q_i)
u	Velocity in the x direction or radial velocity component
v	Velocity in the y direction or tangential velocity component
V_l	Terminal fall velocity of liquid water
V_i	Terminal fall velocity of solid water (ice)
\dot{V}	Tangential momentum source
\vec{V}	Three dimensional velocity vector
w	Velocity in the z direction
W_T	Cooling/warming effect from hydrometeors
x	Horizontal coordinate, eastward distance
y	Horizontal coordinate, northward distance
z	Vertical coordinate, upward distance
z_s	Terrain elevation
z_t	Constant height of the model top
ϵ	Ratio of R_d to R_v
ζ	Vertical component of relative vorticity
ζ_a	Vertical component of absolute vorticity
θ	Potential temperature
θ_e	Pseudo-equivalent potential temperature

θ_ρ	Density potential temperature
$\dot{\theta}$	Material derivative of the diabatic heating rate
Θ_i	Coefficients of θ' equation, for $i = 1, 2, 3$
κ	Ratio of R_d to C_p
λ	Azimuthal angle
ξ	Twice the local absolute angular velocity
π	Non-dimensional pressure
Π_i	Coefficients of π' equation, for $i = 1, 2, 3, 4, 5$
ρ	Density
σ	Terrain-following vertical coordinate
$\tau_{i,j}$	Stress tensors, for $i, j = r, z$
χ	Inverse of θ
ψ	Meridional streamfunction

Bibliography

- Abarca, S. F., and M. T. Montgomery, 2014: Departures from axisymmetric balance dynamics during secondary eyewall formation. *J. Atmos. Sci.*, **71**, 3723–3738.
- Adams, J. C., 1991: *MUltigrid Software for Elliptic Partial Differential Equations: MUDPACK (No. 357)*. National Center for Atmospheric Research.
- Anthes, R. A., 1972: Development of asymmetries in a three-dimensional numerical model of the tropical cyclone. *Mon. Wea. Rev.*, **100**, 461–476.
- Anthes, R. A., 1974: The dynamics and energetics of mature tropical cyclones. *Rev. Geophys. Space Phys.*, **12**, 495–522.
- Arakawa, A., and V. R. Lamb, 1977: Computational design of the basic dynamical process of the ucla general circulation model. *Methods in Computational Physics: Advances in Research and Applications*, **17**, 173–265.
- Bolton, D., 1980: The computation of equivalent potential temperature. *Mon. Wea. Rev.*, **108**, 1046 – 1053.
- Braun, S. A., P. A. Newman, and G. M. Heymsfield, 2016: NASA’s Hurricane and Severe Storm Sentinel (HS3) investigation. *Bull. Amer. Met. Soc.*, **97**, 2085–2102.
- Briggs, W. L., V. E. Hensen, and S. F. McCormick, 2000: *A Multigrid Tutorial, Second Edition*. Society for Industrial and Applied Mathematics, 193 pp., doi:10.1137/1.9780898719505.
- Bryan, G. H., 2012: Effects of surface-exchange coefficients and turbulence length scales on the intensity and structure of numerically simulated hurricanes. *Mon. Wea. Rev.*, **140**, 1125–1143.
- Bryan, G. H., and J. M. Fritsch, 2002: A benchmark simulation for moist nonhydrostatic numerical models. *Mon. Weather Rev.*, **130**, 2917–2928.
- Bryan, G. H., and H. Morrison, 2012: Sensitivity of a simulated squall line to horizontal resolution and parameterization of microphysics. *Mon. Wea. Rev.*, **140**, 202–225.

- Bryan, G. H., and R. Rotunno, 2009a: Evaluation of an analytical model for the maximum intensity of tropical cyclones. *J. Atmos. Sci.*, **66**, 3042–3060.
- Bryan, G. H., and R. Rotunno, 2009b: The maximum intensity of tropical cyclones in axisymmetric numerical model simulations. *Mon. Wea. Rev.*, **137**, 1770–1789.
- Bu, Y. P., R. G. Fovell, and K. L. Corbosiero, 2014: Influence of cloud-radiative forcing on tropical cyclone structure. *J. Atmos. Sci.*, **71**, 1644–1622.
- Bui, H. H., R. K. Smith, M. T. Montgomery, and J. Peng, 2009: Balanced and unbalanced aspects of tropical-cyclone intensification. *Quart. Journ. Roy. Meteor. Soc.*, **135**, 1715–1731.
- Challa, M., and R. Pfeffer, 1980: Effects of eddy fluxes of angular momentum on model hurricane development. *J. Atmos. Sci.*, **37**, 1603–1618.
- Chen, H., and D.-L. Zhang, 2013: On the rapid intensification of Hurricane Wilma (2005). Part II: Convective bursts and the upper-level warm core. *J. Atmos. Sci.*, **70**, 146–162.
- Chen, X., M. Xue, and J. Fang, 2018: Rapid intensification of Typhoon Mujigae (2015) under different sea surface temperatures: Structural changes leading to rapid intensification. *J. Atmos. Sci.*, **75**, 4313–4335.
- Chen, Y., G. Brunet, and M. K. Yau, 2003: Spiral bands in a simulated hurricane. Part II: wave activity diagnosis. *J. Atmos. Sci.*, **60**, 1239–1256.
- Cohen, Y., and N. Paldor, 2020: Lagrangian trajectories at the outflow of tropical cyclones. *Quart. Journ. Roy. Meteor. Soc.*, **147**, 58 – 73.
- Cram, T. A., J. Persing, M. T. Montgomery, and S. A. Braun, 2007: A lagrangian trajectory view on transport and mixing processes between the eye, eyewall, and environment using a high-resolution simulation of Hurricane Bonnie (1998). *J. Atmos. Sci.*, **64**, 1835–1856.
- Doyle, J. D., and Coauthors, 2017: A view of tropical cyclones from above: The tropical cyclone intensity experiment. *Bull. Amer. Met. Soc.*, **98**, 2113–2134.
- Dunion, J. P., 2011: Rewriting the climatology of the tropical north atlantic and caribbean sea atmosphere. *J. Clim.*, **24**, 893–908.
- Duran, P., and J. Molinari, 2018: Dramatic inner-core tropopause variability during the rapid intensification of hurricane patricia (2015). *Mon Wea. Rev.*, **146**, 119–134.
- Duran, P., and J. Molinari, 2019: Tropopause evolution in a rapidly intensifying tropical cyclone: A static stability budget analysis in an idealized axisymmetric framework. *J. Atmos. Sci.*, **76**, 209–229.

- Eliassen, A., 1951: Slow thermally or frictionally controlled meridional circulation in a circular vortex. *Astrophys. Norv.*, **5**, 19–60.
- Emanuel, K. A., 1986: An air-sea interaction theory for tropical cyclones. Part I: Steady state maintenance. *J. Atmos. Sci.*, **43**, 585–604.
- Emanuel, K. A., 1988: The maximum intensity of hurricanes. *J. Atmos. Sci.*, **45**, 1143–1155.
- Emanuel, K. A., 1989: The finite-amplitude nature of tropical cyclogenesis. *J. Atmos. Sci.*, **46**, 3431–3456.
- Emanuel, K. A., 1991: The theory of hurricanes. *Annu. Rev. Fluid Mech.*, **23**, 179–196.
- Emanuel, K. A., 2012: Self-stratification of tropical cyclone outflow. Part II: Implications for storm intensification. *J. Atmos. Sci.*, **69**, 988–996.
- Emanuel, K. A., 2018: 100 years of progress in tropical cyclone research. *Meteorological Monographs*, **59**, 15.1–15.68.
- Flatau, M., and D. E. Stevens, 1993: The role of outflow-layer instabilities in tropical cyclone motion. *J. Atmos. Sci.*, **50**, 1721–1733.
- Fovell, R. G., Y. P. Bu, K. L. Corbosiero, W.-W. Tung, Y. Cao, H.-C. Kuo, L.-H. Hsu, and H. Su, 2016: Influence of cloud microphysics and radiation on tropical cyclone structure and motion. *Meteorological Monographs*, **56**, 11.1–11.27.
- Gal-Chen, G., and R. Somerville, 1975: On the use of a coordinate transformation for the solution of the navier-stokes equations. *J. Comput. Phys.*, **17**, 209–228.
- Hack, J. J., and W. H. Schubert, 1986: Nonlinear response of atmospheric vortices to heating by organized cumulus convection. *J. Atmos. Sci.*, **43**, 1559–1573.
- Hausman, S. A., K. V. Ooyama, and W. H. Schubert, 2006: Potential vorticity structure of simulated hurricanes. *J. Atmos. Sci.*, **63**, 87–108.
- Heng, J., and Y. Wang, 2016: Nonlinear response of a tropical cyclone vortex to prescribed eyewall heating with and without surface friction in tcm4: Implications for tropical cyclone intensification. *J. Atmos. Sci.*, **73**, 1315–1333.
- Heng, J., Y. Wang, and W. Zhou, 2017: Revisiting the balanced and unbalanced aspects of tropical cyclone intensification. *J. Atmos. Sci.*, **74**, 2575–2591.
- Heng, J., Y. Wang, and W. Zhou, 2018: Reply to “comments on ‘revisiting the balanced and unbalanced aspects of tropical cyclone intensification’”. *J. Atmos. Sci.*, **75**, 2497–2505.

- Kieu, C., V. Tallapragada, D.-L. Zhang, and Z. Moon, 2016: On the development of double warm-core structures in intense tropical cyclones. *J. Atmos. Sci.*, **73**, 4487–4506.
- Kilroy, G., R. K. Smith, and M. T. Montgomery, 2016: Why do model tropical cyclones grow progressively in size and decay in intensity after reaching maturity? *J. Atmos. Sci.*, **73**, 487–503.
- Komaromi, W. A., and J. D. Doyle, 2017: Tropical cyclone outflow and warm core structure as revealed by HS3 dropsonde data. *Mon. Wea. Rev.*, **145**, 1339–1359.
- Landau, L. D., and E. M. Lifshitz, 1966: *Fluid Mechanics. Third Revised English Edition*. Pergamon Press, 536pp.
- Meunier, P., and E. Villiermaux, 2003: How vortices mix. *J. Fluid Mech.*, **476**, 213–222.
- Molinari, J., and Vollaro, 1990: External influences on hurricane intensity. Part II: Vertical structure and the response of the hurricane vortex. *J. Atmos. Sci.*, **47**, 1902–1918.
- Möller, J. D., and L. J. Shapiro, 2002: Balanced contributions to the intensification of hurricane opal as diagnosed from a GFDL model forecast. *Mon. Wea. Rev.*, **130**, 1866–1881.
- Möller, J. D., and R. K. Smith, 1994: The development of potential vorticity in a hurricane-like vortex. *Quart. Journ. Roy. Meteor. Soc.*, **120**, 1255–1265.
- Montgomery, M. T., and B. F. Farrell, 1993: Tropical cyclone formation. *J. Atmos. Sci.*, **50**, 285–310.
- Montgomery, M. T., G. Kilroy, R. K. Smith, and N. Črnivec, 2020: Contribution of eddy momentum processes to tropical cyclone intensification. *Quart. Journ. Roy. Meteor. Soc.*, **146**, 3101–3117.
- Montgomery, M. T., and J. Persing, 2020: Does balance dynamics well capture the secondary circulation and spin-up of a simulated tropical cyclone? *J. Atmos. Sci.*, **78**, 75–95.
- Montgomery, M. T., J. Persing, and R. K. Smith, 2019: On the hypothesized outflow control of tropical cyclone intensification. *Quart. Journ. Roy. Meteor. Soc.*, **145**, 1309–1322.
- Montgomery, M. T., and R. K. Smith, 2014: Paradigms for tropical cyclone intensification. *Aust. Met. Ocean. Soc. Jounl.*, **64**, 37–66.
- Montgomery, M. T., and R. K. Smith, 2017: Recent developments in the fluid dynamics of tropical cyclones. *Annu. Rev. Fluid Mech.*, **49**, 541–574.
- Montgomery, M. T., and R. K. Smith, 2018: Comments on: “Revisiting the balanced and unbalanced aspects of tropical cyclone intensification”. *J. Atmos. Sci.*, **75**, 2491–2496.

- Montgomery, M. T., and R. K. Smith, 2019: Toward understanding the dynamics of spin up in Emanuel's tropical cyclone model. *J. Atmos. Sci.*, **76**, 3089–3093.
- Nguyen, V. S., R. K. Smith, and M. T. Montgomery, 2008: Tropical-cyclone intensification and predictability in three dimensions. *Quart. Journ. Roy. Meteor. Soc.*, **134**, 563–582.
- Ohno, T., and M. Satoh, 2015: On the warm core of a tropical cyclone formed near the tropopause. *J. Atmos. Sci.*, **72**, 551–571.
- Ooyama, K. V., 1969: Numerical simulation of the life cycle of tropical cyclones. *J. Atmos. Sci.*, **26**, 3–40.
- Ooyama, K. V., 1982: Conceptual evolution of the theory and modeling of the tropical cyclone. *J. Meteor. Soc. Japan*, **60**, 369–380.
- Ooyama, K. V., 1987: Numerical experiments of steady and transient jets with simple model of the hurricane outflow layer. *Preprint, 17th Conf. on Hurricanes and Tropical Meteorology, Miami, Florida, Amer. Meteor. Soc.*, **17**, 318–320.
- Pendergrass, A. G., and H. E. Willoughby, 2009: Diabatically induced secondary flows in tropical cyclones. Part I. Quasi-steady forcing. *Mon. Wea. Rev.*, **137**, 3–40.
- Persing, J., M. T. Montgomery, J. McWilliams, and R. K. Smith, 2013: Asymmetric and axisymmetric dynamics of tropical cyclones. *Atmos. Chem. Phys.*, **13**, 12 299–12 341.
- Press, W. H., S. A. Teukolsky, W. T. Vetterling, and B. P. Flannery, 1992: *Numerical Recipes in C: The art of scientific computing*. Cambridge University Press, Cambridge, England, ISBN-13:978-1107404083, 994pp.
- Rappin, E. D., M. C. Morgan, and G. J. Tripoli, 2011: The impact of outflow environment on tropical cyclone intensification and structure. *J. Atmos. Sci.*, **68**, 177–194.
- Reasor, P. D., and M. T. Montgomery, 2015: Evaluation of a heuristic model for tropical cyclone resilience. *J. Atmos. Sci.*, **72**, 1765–1782.
- Rotunno, R., and K. A. Emanuel, 1987: An air-sea interaction theory for tropical cyclones. Part II :Evolutionary study using a nonhydrostatic axisymmetric numerical model. *J. Atmos. Sci.*, **44**, 542–561.
- Rozoff, C. M., W. H. Schubert, and J. P. Kossin, 2008: Some dynamical aspects of tropical cyclone concentric eyewalls. *Quart. Journ. Roy. Meteor. Soc.*, **135**, 583–593.
- Schecter, D. A., 2019: On the instabilities of tropical cyclones generated by cloud resolving models. *Tellus A*, **70**, 1–30.
- Schubert, W. H., and B. T. Alworth, 1982: Evolution of potential vorticity in tropical cyclones. *Quart. Journ. Roy. Meteor. Soc.*, **39**, 1687–1697.

- Schubert, W. H., and J. J. Hack, 1982: Inertial stability and tropical cyclone development. *J. Atmos. Sci.*, **39**, 1687–1697.
- Schubert, W. H., C. J. Slocum, J. L. Vigh, B. D. McNoldy, and J. P. Kossin, 2007: On the distribution of subsidence in the hurricane eye. *Quart. Journ. Roy. Meteor. Soc.*, **133**, 1–20.
- Shapiro, L. J., and M. T. Montgomery, 1993: A three-dimensional balance theory for rapidly-rotating vortices. *J. Atmos. Sci.*, **50**, 3322–3335.
- Shapiro, L. J., and H. Willoughby, 1982: The response of balanced hurricanes to local sources of heat and momentum. *J. Atmos. Sci.*, **39**, 378–394.
- Smith, R. K., 1981: The cyclostrophic adjustment of vortices with application to tropical cyclone modification. *J. Atmos. Sci.*, **38**, 2020–2030.
- Smith, R. K., 2006: Accurate determination of a balanced axisymmetric vortex. *Tellus A*, **58**, 98–103.
- Smith, R. K., G. Kilroy, and M. T. Montgomery, 2014a: Why do model tropical cyclones intensify more rapidly at low latitudes? *J. Atmos. Sci.*, **140**, 1783–1804.
- Smith, R. K., and M. T. Montgomery, 2015: Towards clarity on understanding tropical cyclone intensification. *J. Atmos. Sci.*, **72**, 3020–3031.
- Smith, R. K., M. T. Montgomery, and S. A. Braun, 2019: Azimuthally averaged structure of Hurricane Edouard (2014) just after peak intensity. *Quart. Journ. Roy. Meteor. Soc.*, **145**, 211–216.
- Smith, R. K., M. T. Montgomery, and H. Bui, 2018a: Axisymmetric balance dynamics of tropical cyclone intensification and its breakdown revisited. *J. Atmos. Sci.*, **75**, 3169–3189.
- Smith, R. K., M. T. Montgomery, and G. Kilroy, 2018b: The generation of kinetic energy in tropical cyclones revisited. *Quart. Journ. Roy. Meteor. Soc.*, **144**, 2481–2490.
- Smith, R. K., M. T. Montgomery, and J. Persing, 2014b: On steady-state tropical cyclones. *Quart. Journ. Roy. Meteor. Soc.*, **140**, 2638–2649.
- Smith, R. K., and S. Wang, 2018: Axisymmetric balance dynamics of tropical cyclone intensification: Diabatic heating versus surface friction. *Quart. Journ. Roy. Meteor. Soc.*, **144**, 2350–2357.
- Stern, D. P., J. D. Kepert, G. Bryan, and J. Doyle, 2020: Understanding atypical mid-level wind speed maxima in hurricane eyewalls. *J. Atmos. Sci.*, **77**, early view online.
- Sundqvist, H., 1970a: Numerical simulation of the development of tropical cyclones with a ten-level model. Part I. *Tellus*, **4**, 359–390.

- Sundqvist, H., 1970b: Numerical simulation of the development of tropical cyclones with a ten-level model. Part II. *Tellus*, **5**, 505–510.
- Tao, D., K. A. Emanuel, F. Zhang, R. Rotunno, M. M. Bell, and R. G. Nystrom, 2019: Evaluation of the assumptions in the steady-state tropical cyclone self-stratified outflow using three-dimensional convection-allowing simulations. *J. Atmos. Sci.*, **76**, 2995–3009.
- Vogl, S., and R. K. Smith, 2009: Limitations of a linear model for the hurricane boundary layer. *Quart. Journ. Roy. Meteor. Soc.*, **135**, 839–850.
- Wang, Y., and H. Wang, 2013: The inner-core size increase of Typhoon Megi (2010) during its rapid intensification phase. *Trop. Cyclone Res. Rev.*, **2**, 65–80.
- Willoughby, H. E., 1979: Forced secondary circulations in hurricanes. *J. Geophys. Res.*, **84**, 3173–3183.
- Willoughby, H. E., 1988: The dynamics of the tropical cyclone core. *Aust. Meteor. Mag.*, **36**, 183–191.
- Willoughby, H. E., 1990: Temporal changes of the primary circulation in tropical cyclones. *J. Atmos. Sci.*, **47**, 242–264.
- Wirth, V., 1995: Diabatic heating in an axisymmetric cut-off cyclone and related stratosphere-troposphere exchange. *Quart. Journ. Roy. Meteor. Soc.*, **121**, 127–147.
- Wirth, V., and T. J. Dunkerton, 2006: A unified perspective on the dynamics of axisymmetric hurricanes and monsoons. *J. Atmos. Sci.*, **63**, 2529–2547.
- Zhang, D.-L., and H. Chen, 2012: Importance of the upper-level warm core in the rapid intensification of a tropical cyclone. *Geophys. Res. Lett.*, **39**, L02 806, doi:10.1029/2011GL050 578.
- Zhang, D.-L., Y. Liu, and M. K. Yau, 2001: A multi-scale numerical study of Hurricane Andrew (1992). Part IV: Unbalanced flows. *Mon. Wea. Rev.*, **61**, 92–107.

Acknowledgments

I want to express the depth of my gratitude to Prof. Roger Smith, I am so lucky to have had you as my supervisor. Your support with a wealth of knowledge is the base of the thesis. Thanks for teaching me how to think, it will affect my research career forever.

Thanks to Prof. Michael Montgomery for exciting discussions and insightful comments. I would like to use “adventure” to describe this experience.

Thank you to my colleague and friend Dr. Gerard Kilroy, you help me a lot not only in work, but also in daily life.

Thanks to Dr. Christian Keil for his help with some translations to German.

I love you, Xinlu Dai, your understanding and encouragement are the bones of my life and study.

This work has been generously supported by the China Scholarship Council (CSC201708510100).

Curriculum Vitae

Shanghong Wang

Faculty of Physics, Ludwig-Maximilians-University
Theresienstr. 37, 80333 Munich

Nationality: Chinese

Date of Birth: Jan.03. 1992

Contact: shanghong.wang@physik.uni-muenchen.de

Education

10/2017 – Now	Ph. D. student at the University of Munich (LMU), Faculty of Physics, Prof. Dr. Roger K. Smith. Thesis title: Upper-tropospheric Inflow Layers in Tropical Cyclones
09/2014 – 06/2017	M. S. Atmospheric Science, Chengdu University of Information Technology, China,
09/2010 – 06/2014	B. S. Atmospheric Science, Chengdu University of Information Technology, China

Publications

- Upper-tropospheric inflow layers in tropical cyclones. Quart. J. Roy. Meteor. Soc., 146: 3466–3487., 2020, S. Wang, R. K. SMITH and M. T. Montgomery.
<https://doi.org/10.1002/qj.3856>
- Consequences of regularizing the Sawyer-Eliassen equation in balance models for

tropical cyclone behaviour., Quart. J. Roy. Meteor. Soc., 145, 3766–3779., 2019, S. Wang and R. K. SMITH. <https://doi.org/10.1002/qj.3656>

- Axisymmetric balance dynamics of tropical cyclone intensification: Diabatic heating versus surface friction., Quart. J. Roy. Meteor. Soc., 144, 2350-2357., 2018, R. K. SMITH, and S. Wang. <https://doi.org/10.1002/qj.3389>
- Solutions of the Eliassen balance equation for inertially and/or symmetrically stable and unstable vortices. Quart. J. Roy. Meteor. Soc., S. Wang, M. T. MONTGOMERY, and R. K. Smith, **Revised**
- Upper level trajectories in the prototype problem for tropical cyclone intensification. Quart. J. Roy. Meteor. Soc., S. Wang, and R. K. SMITH, **Revised**